OAK RIDGE NATIONAL LABORATORY

MANAGED BY UT-BATTELLE FOR THE DEPARTMENT OF ENERGY

Gary L. Bell, Ph.D.
Fusion Energy Division
P.O. Box 2008, Bldg. 4508, Rm. 239
Oak Ridge, TN 37831-6093
(865) 241-4400
E-Mail: bellgl@ornl.gov

August 11, 2004

AGR-1008

Dr. Madeline A. Feltus
Manager, Advanced Gas Reactor
NE-20, Building GTN
Department of Energy
1000 Independence Avenue, SW
Washington, DC 20585-1290

Dear Dr. Feltus:

DE-AC05-00OR22725, Transmittal of Data Summary Report – ORNL Central File 04/08 "Results from ORNL Characterization of HRB-21 Reference Fuel"

The purpose of this letter is to provide you with a copy of the data summary report ORNL/CF-04/08, "Results from ORNL Characterization of HRB-21 Reference Fuel" (attached). This document is not a program deliverable but does provide a record of the work performed and is given to you and program participants for information purposes.

If you have any questions, please contact me at 865-241-4400 or John Hunn at 865-574-2480.

Sincerely,

Gary L. Bell, Ph.D.
Manager, Advanced Gas Reactor Program

GLB:jzp

cc/att: E. E. Bloom
J. D. Hunn
R.E. Korenke (INEEL)
S. R. Martin, Jr. (DOE-ORO)
G. E. Michaels
S. L. Milora
D. A. Petti (INEEL)
J. J. Saurwein (GA)
S. J. Zinkle
File-RC

OAK RIDGE
NATIONAL LABORATORY
MANAGED BY UT-BATTELLE
FOR THE DEPARTMENT OF ENERGY

ORNL/CF-04/08

Results From ORNL Characterization HRB-21 Reference Fuel

J. D. Hunn

August 2004

UT-BATTELLE
ORNL-27 (4-00)

Results from ORNL Characterization of HRB-21 Reference Fuel

John D. Hunn

Oak Ridge National Laboratory

This document is a compilation of the characterization data produced by ORNL for coated UCO fuel particles (350 μm kernel diameter) fabricated by GA for the HRB-21 irradiation test capsule. The archived fuel particles from the batch used in HRB-21 were obtained by the Advanced Gas Reactor Fuel Development and Qualification (AGR) program for use as a reference material. The GA characterization data for this batch of fuel particles is presented in document GT-HTGR-88357, Rev. C, "Capsule HRB-21 Preirradiation Report." The archived fuel particles obtained by the AGR Program are from batch 8876-70, which was the parent batch for batch 8876-70-O, which was actually irradiated in HRB-21. The difference between batches 8876-70 and 8876-70-O is that the particles in batch 8876-70 do not have the seal coat and protective pyrocarbon coating (PPyC) that were deposited over the OPyC layer in batch 8876-70-O. The ORNL designation for the material characterized is AGR-10.

This document summarizes characterization of the HRB-21 fuel for size, shape, coating thickness, and density. Fracture behavior and microstructural analysis of the layers and interfaces is compared to previous analyses of the German proof test particles (EUO 2358-2365) published in ORNL/CF-04/06. Further detailed comparative study of the microstructure of these two reference materials would be valuable to continue to define the property differences between particles which exhibited good irradiation performance (the German particles) and poor irradiation performance (the HRB-21 particles).

Table of Contents

1 Breaking Off Coating Fragments

J.D. Hunn, D.L. Barker, and N. Hashimoto

Several measurements required that the particle coatings be broken away from the kernel. This was done by placing several particles at a time into a stainless steel cylindrical dye and applying light pressure with a stainless steel cylindrical ram. The particles were fractured between the two flat surfaces of the cylinders. The coatings did not separate cleanly from the kernels as was observed for the German reference fuel. Fracture occurred either in the buffer layer or near the buffer/IPyC interface instead. Most of the coatings separated at the SiC/OPyC interface as well (much more so than with the German reference fuel where the four coatings tended to stay together). Figure 1-1 shows the coating fragments broken from the HRB-21 particles. Most of the pieces were either free OPyC or IPyC/SiC with some buffer attached. The free OPyC shells were relatively smooth on the inner surface where they were deposited on the SiC. In Figure 1-1, a white ring could be seen on the inner surface of the OPyC shells, this was a reflection from the ring light on the stereo microscope. Figure 1-2 shows the HRB-21 kernels after removing the coatings shown in Figure 1-1. Most of the kernels still had some amount of buffer attached. Figure 1-3 shows coatings broken from the German fuel. Most of the pieces still had all four coatings. The inside surface of the buffer was smooth and reflected the stereoscope ring light as a white circle. Figure 1-4 shows the German kernels after removing the coatings. The surfaces were smooth and shiny with no buffer attached. In both sets of fuel materials, the IPyC/SiC interface appeared relatively strong.

Images were obtained of a few of the fractured HRB-21 coatings using a scanning electron microscope (SEM). Images were obtained in scanning electron mode (SE) or backscattered electron mode (BSE), as noted on each figure. Figure 1-5 through Figure 1-10 show a typical coating fragment where the OPyC has broken off from the SiC and the inner separation has occurred both within the buffer and at the buffer/IPyC interface. A portion of buffer can be seen in the middle of the inner surface in Figure 1-5 and Figure 1-6 where the fracture occurred in the buffer rather than at the buffer/IPyC interface. Figure 1-7 shows a different fragment where the seal coat that was deposited between the buffer and IPyC can be seen. Figure 1-8 through Figure 1-10 show the fracture surfaces of the IPyC and SiC. Figure 1-11 through Figure 1-15 show a fragment of OPyC that broke off of the SiC.

For comparison, Figure 1-16 through Figure 1-20 are of coating fragments from the German reference fuel. Figure 1-16 shows the typical fragment, where separation occurred at the kernel/buffer interface and the four coatings remained together. Less common was the case shown in Figure 1-17 where the fracture occurred at the buffer/IPyC interface. In some cases, the OPyC layer broke off the SiC, but this was much more rarely observed than in the case of the HRB-21 fuel. Figure 1-18 shows the IPyC, SiC, and OPyC coatings at the same magnification as Figure 1-8 and Figure 1-14. Figure 1-19 shows the IPyC and SiC coatings at the same magnification as Figure 1-9. Figure 1-20 shows the SiC interface at the same magnification as Figure 1-10. Both reference materials showed a combination of intergranular and intragranular fracture in the SiC. The HRB-21 SiC fracture surface showed more large smooth facets, indicating a greater tendency for failure at the grain boundaries. The German SiC showed mostly stepped fracture surfaces, indicating fracture within the grains.

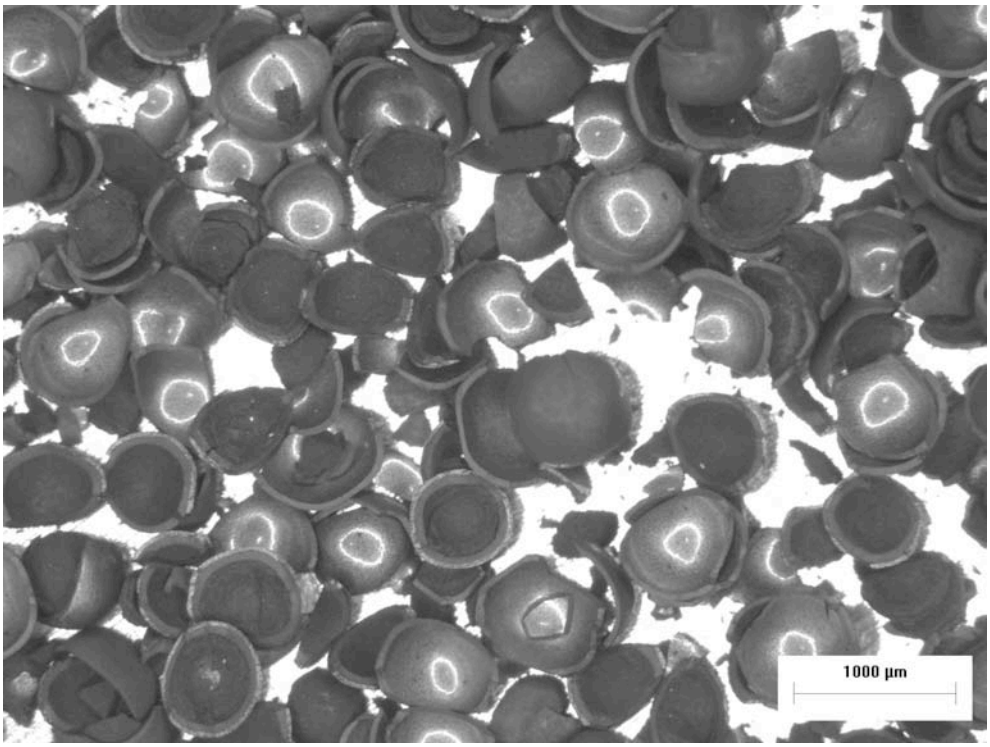

Figure 1-1: Coating fragments from HRB-21.

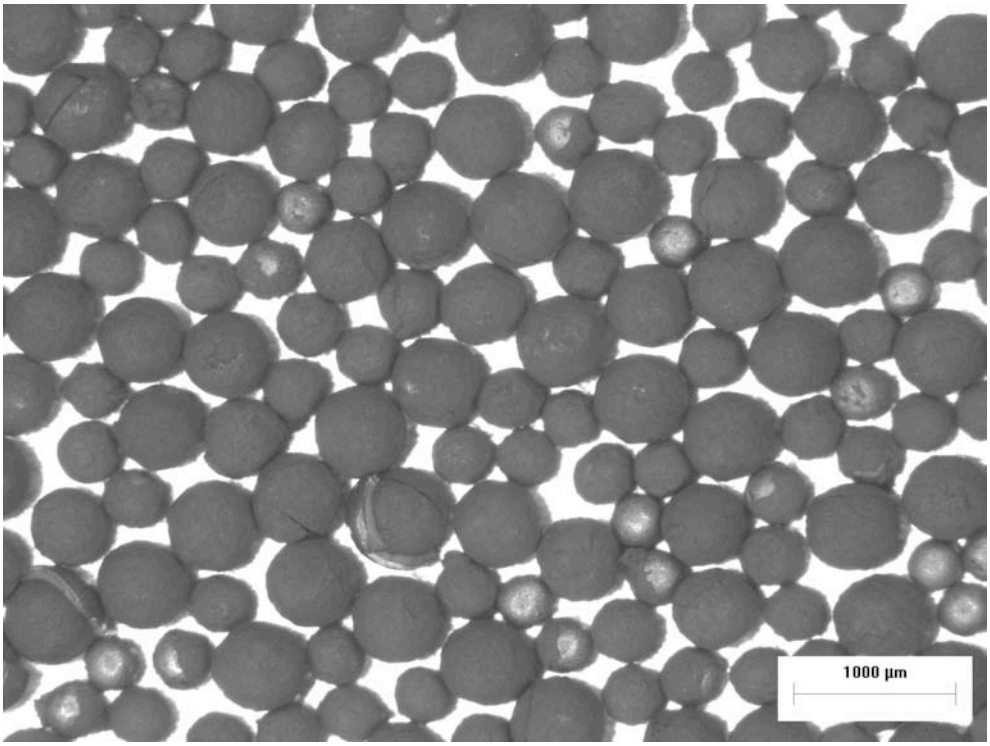

Figure 1-2: Buffer coated kernels after breaking coating fragments from HRB-21.

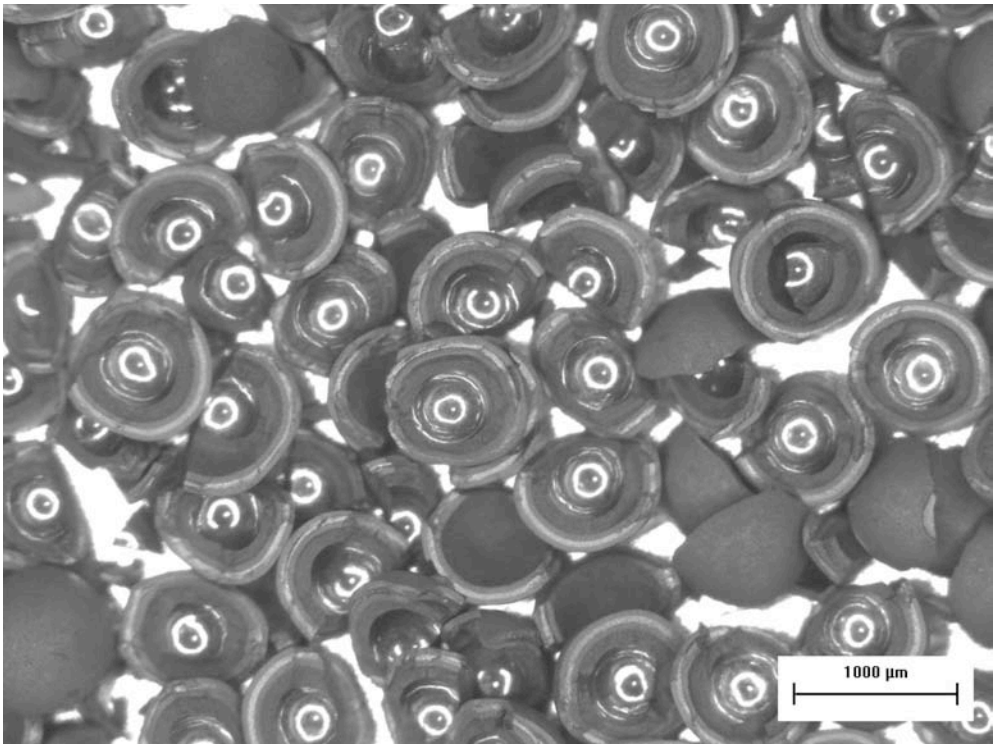

Figure 1-3: Coating fragments from German fuel.

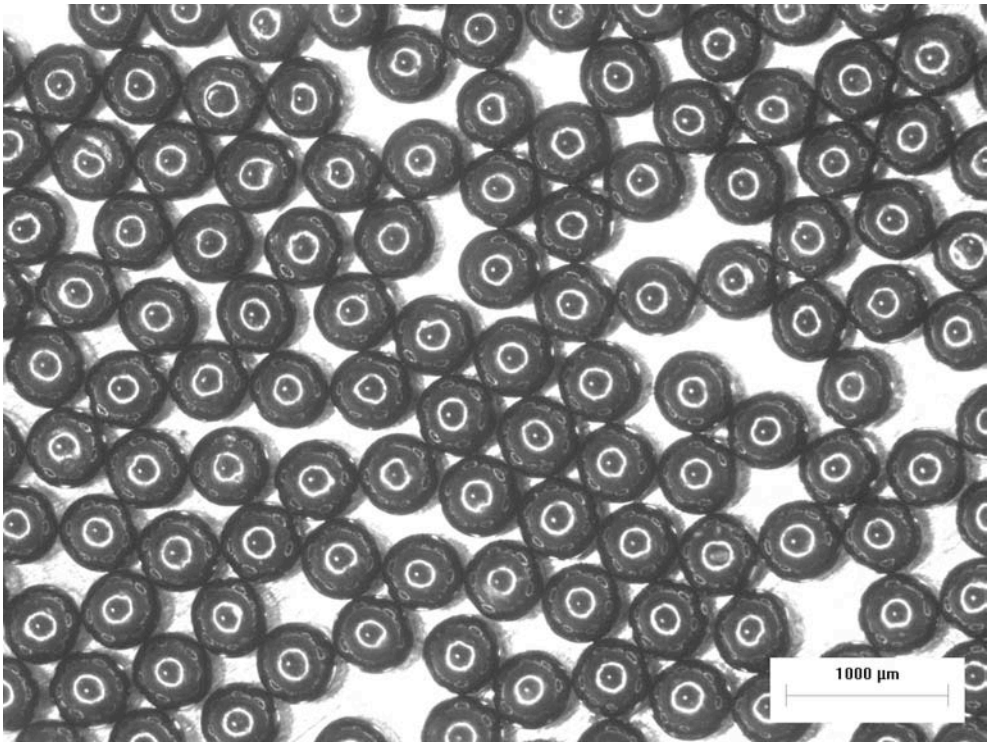

Figure 1-4: Free kernels after breaking coating fragments from German fuel.

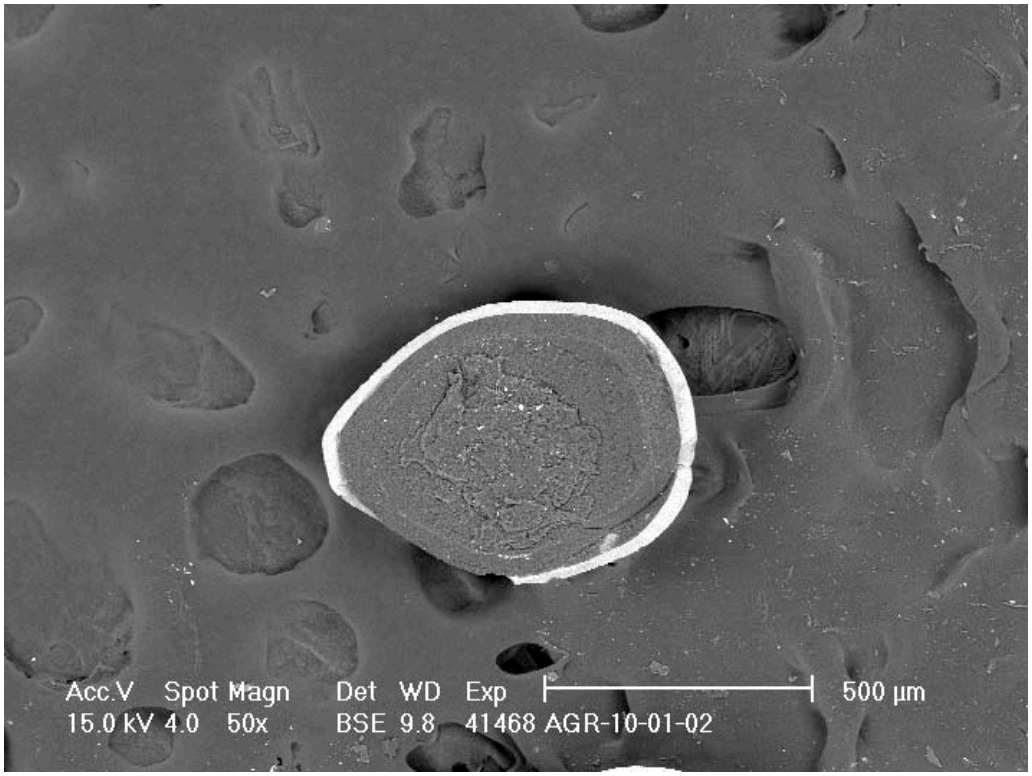

Figure 1-5: HRB-21 IPyC/SiC fragment with some buffer still attached.

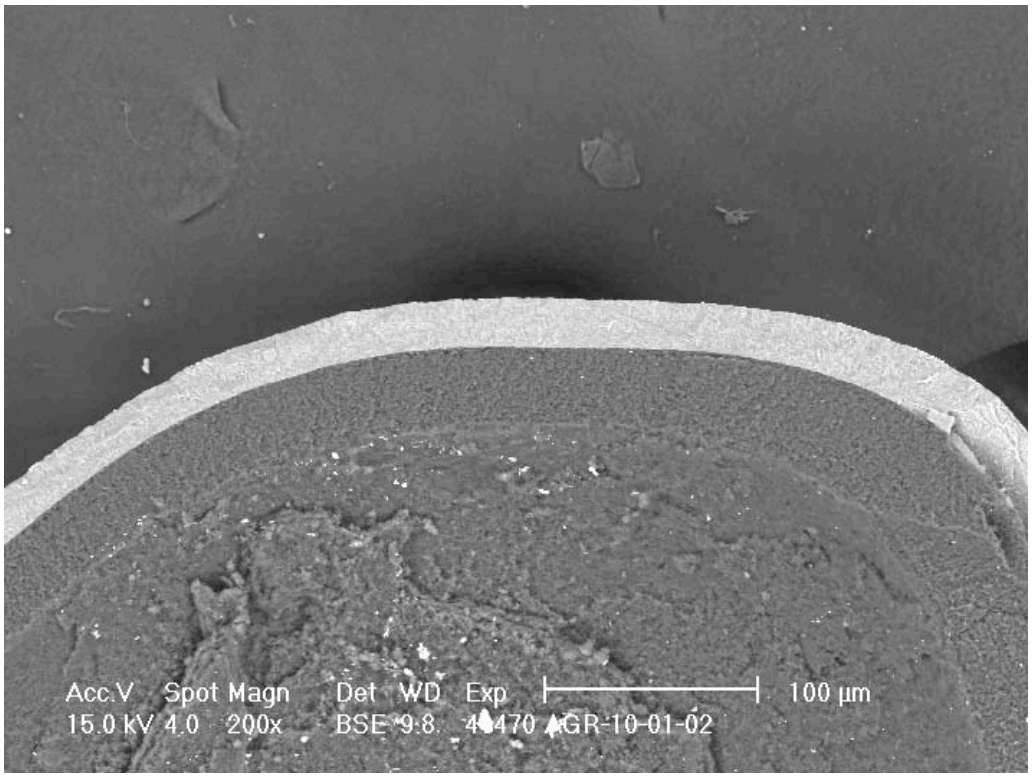

Figure 1-6: HRB-21 IPyC/SiC fragment with some buffer still attached.

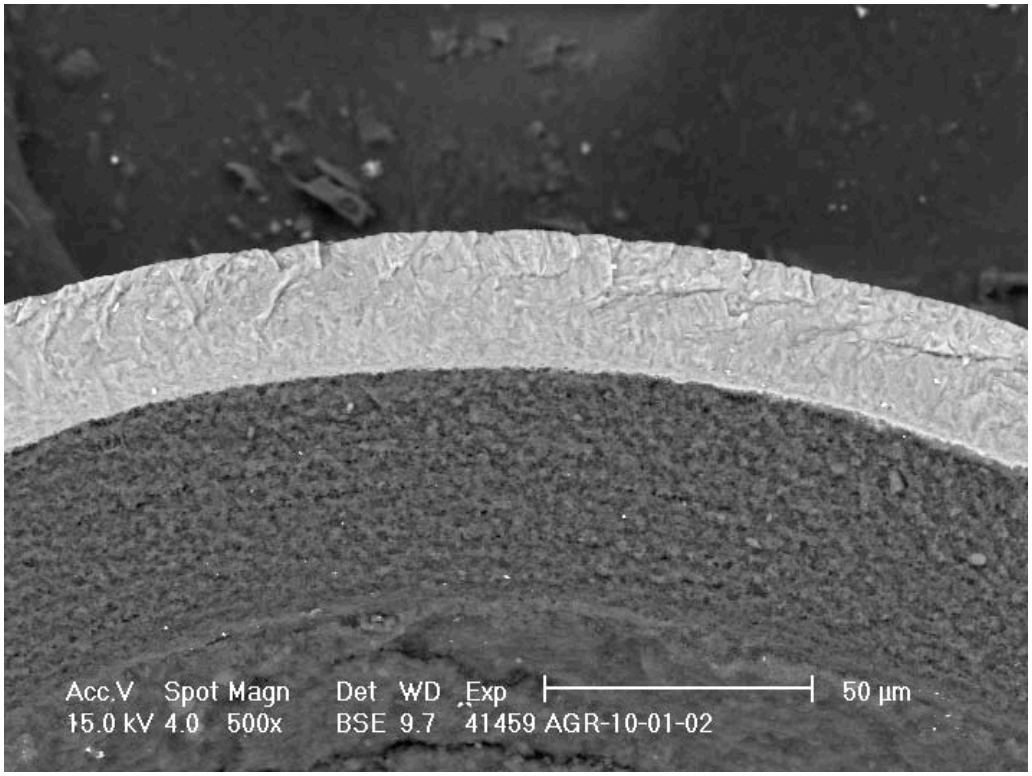

Figure 1-7: HRB-21 IPyC/SiC fragment with buffer/IPyC interface seal coat visible.

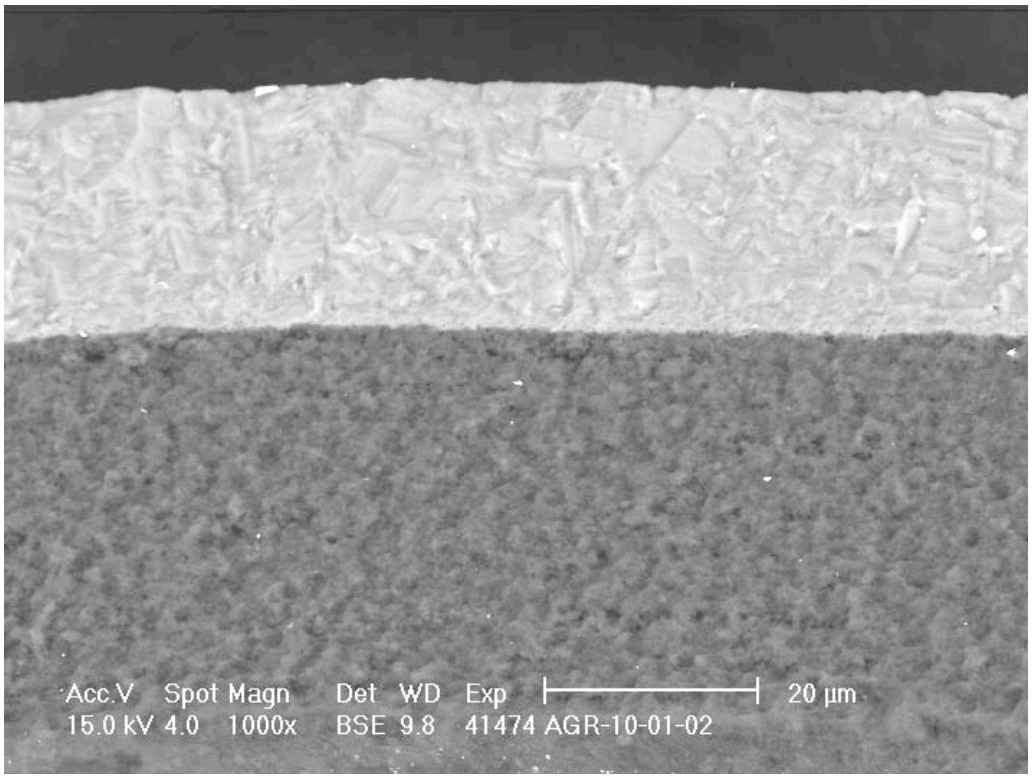

Figure 1-8: HRB-21 IPyC/SiC fragment.

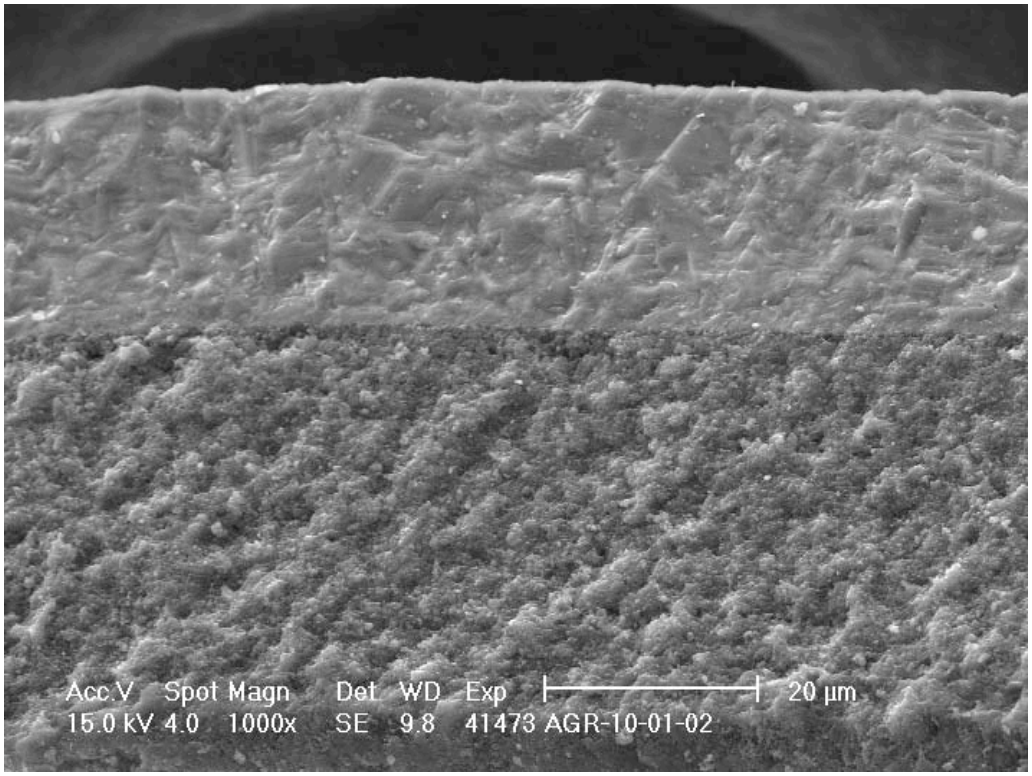

Figure 1-9: HRB-21 Scanning electron image of same area in Figure 1-8.

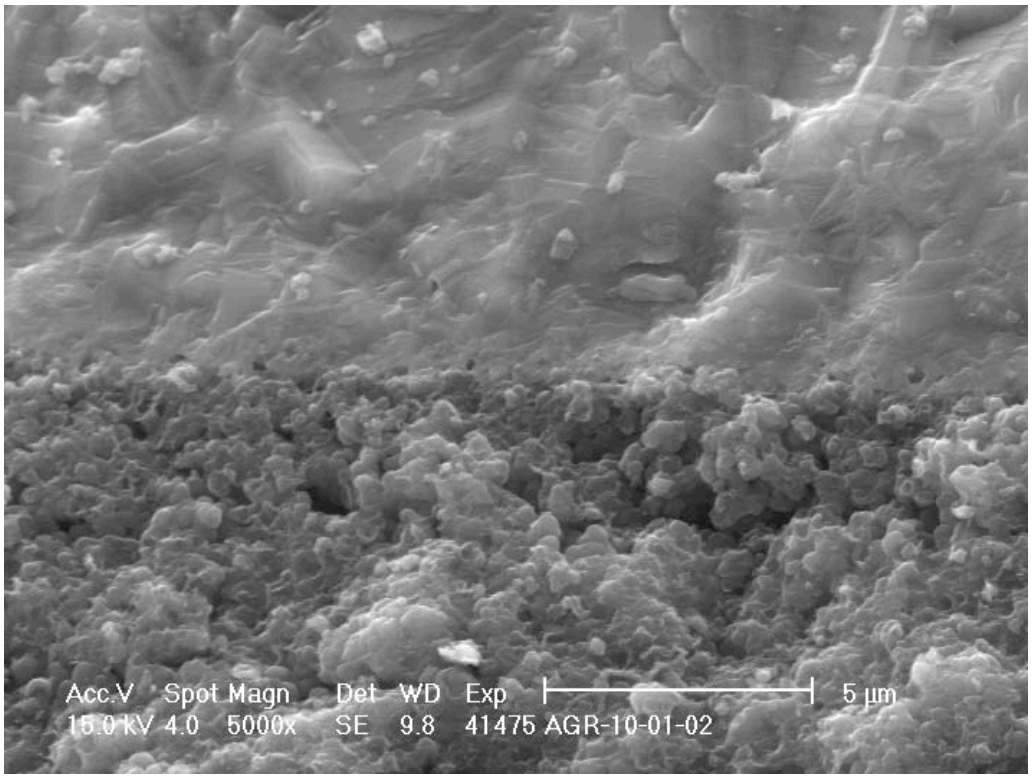

Figure 1-10: HRB-21 IPyC/SiC interface.

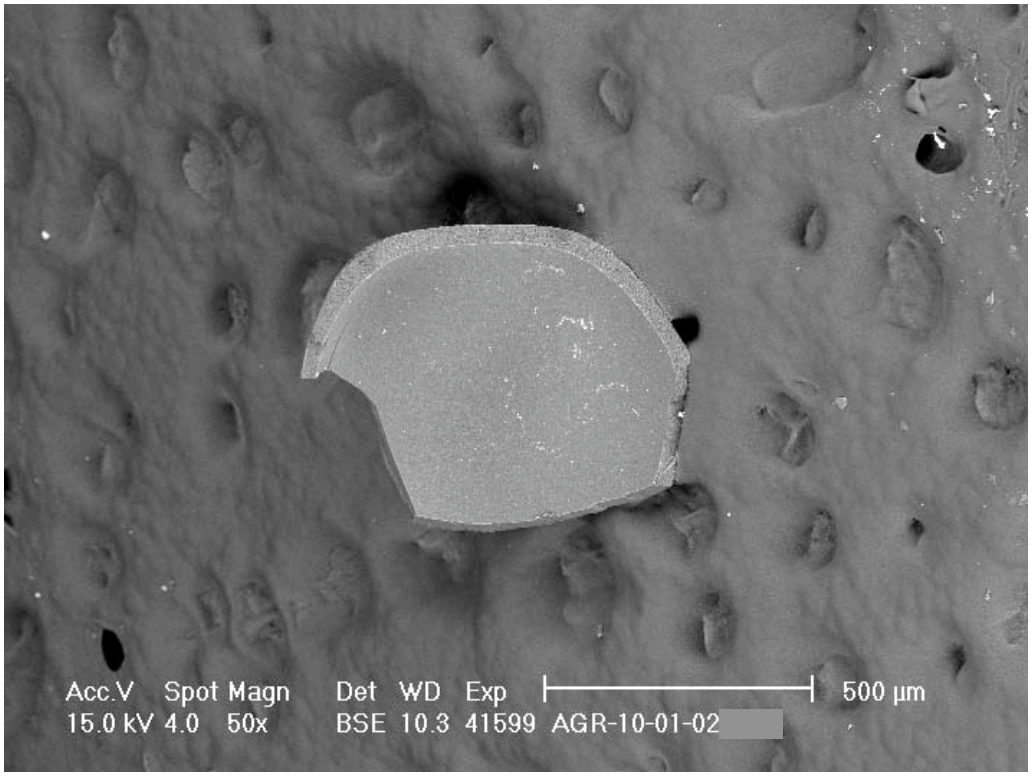

Figure 1-11: HRB-21 OPyC fragment.

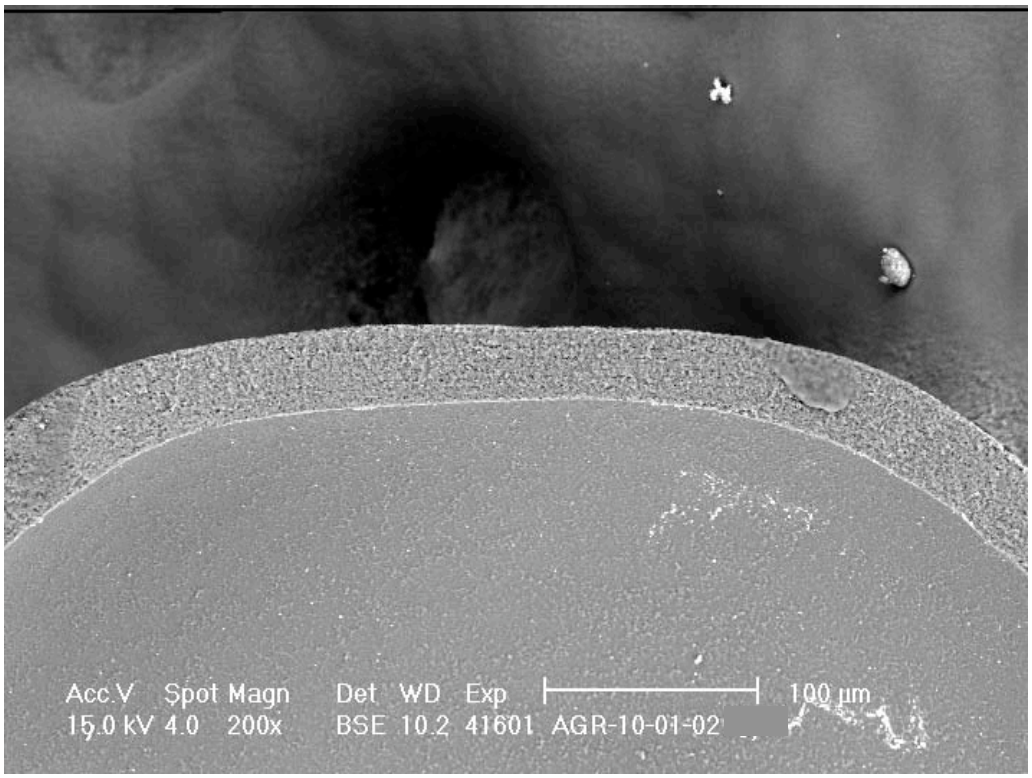

Figure 1-12: HRB-21 OPyC fragment.

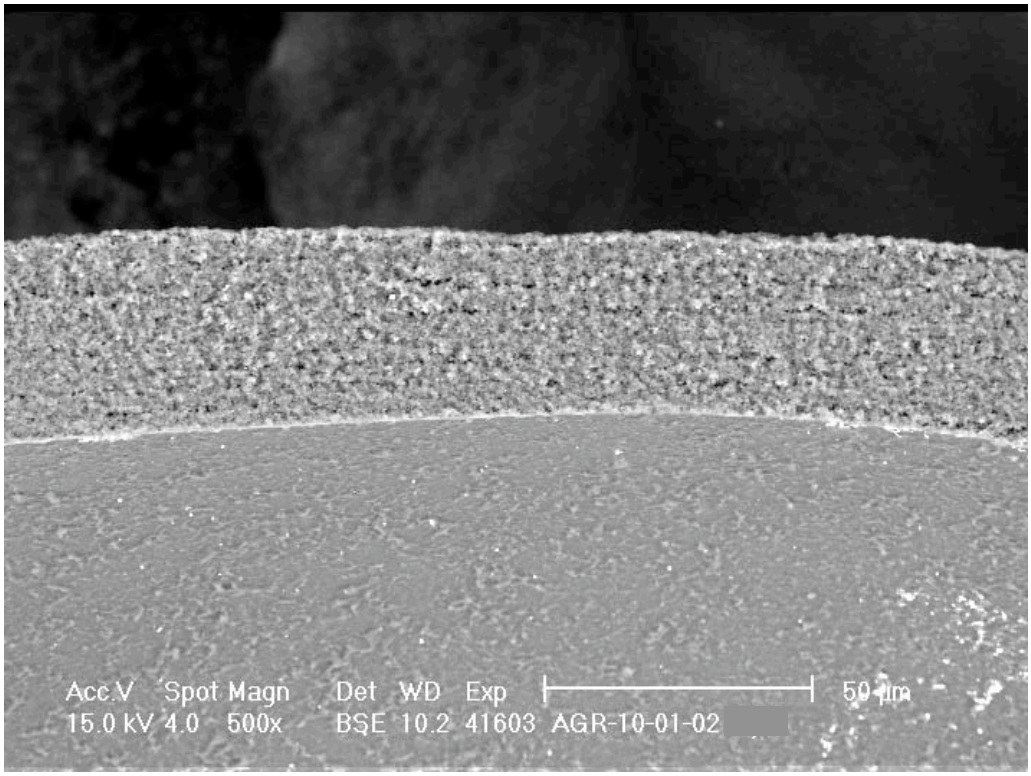

Figure 1-13: HRB-21 OPyC fragment.

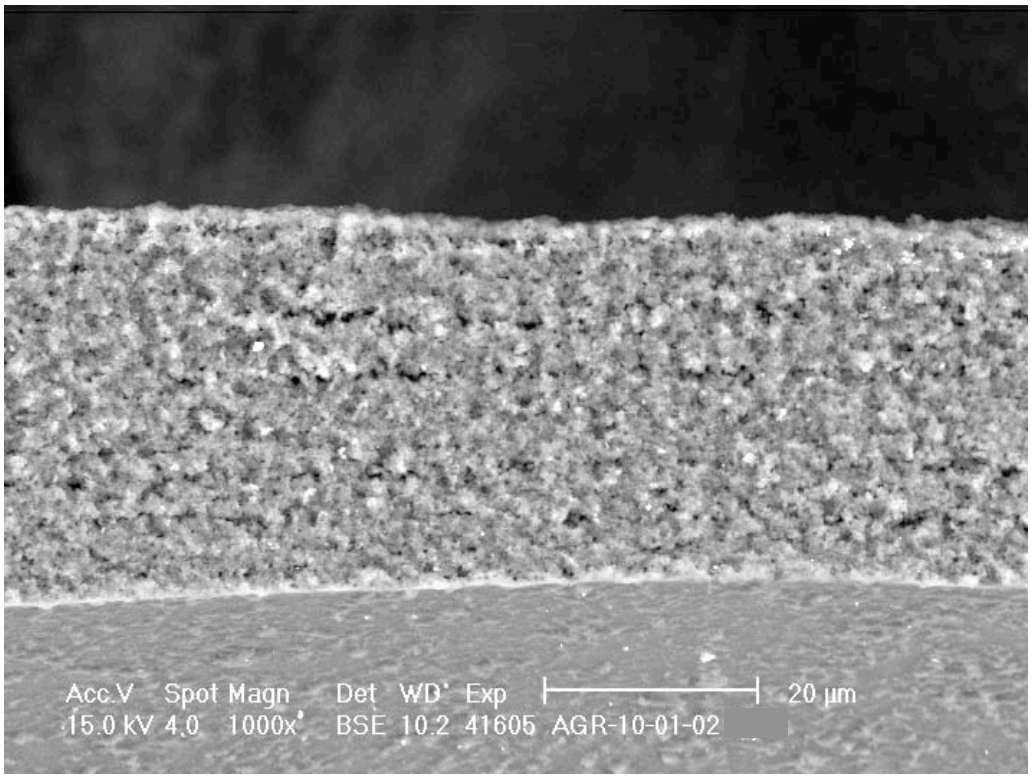

Figure 1-14: HRB-21 OPyC fragment.

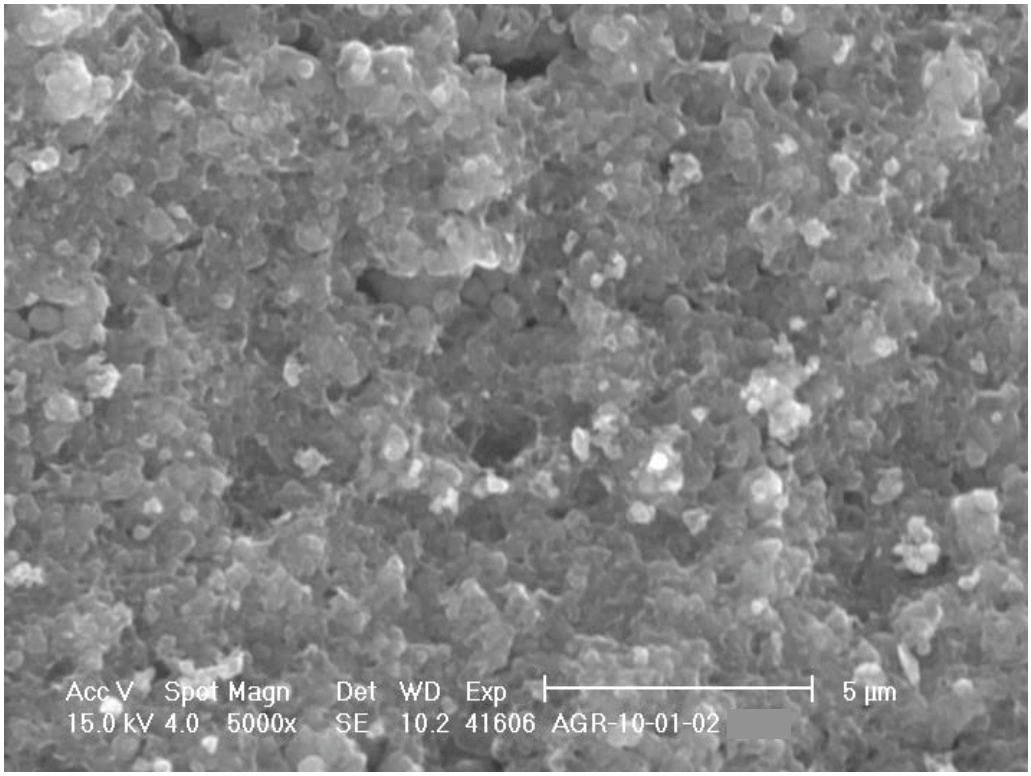

Figure 1-15: HRB-21 OPyC fragment.

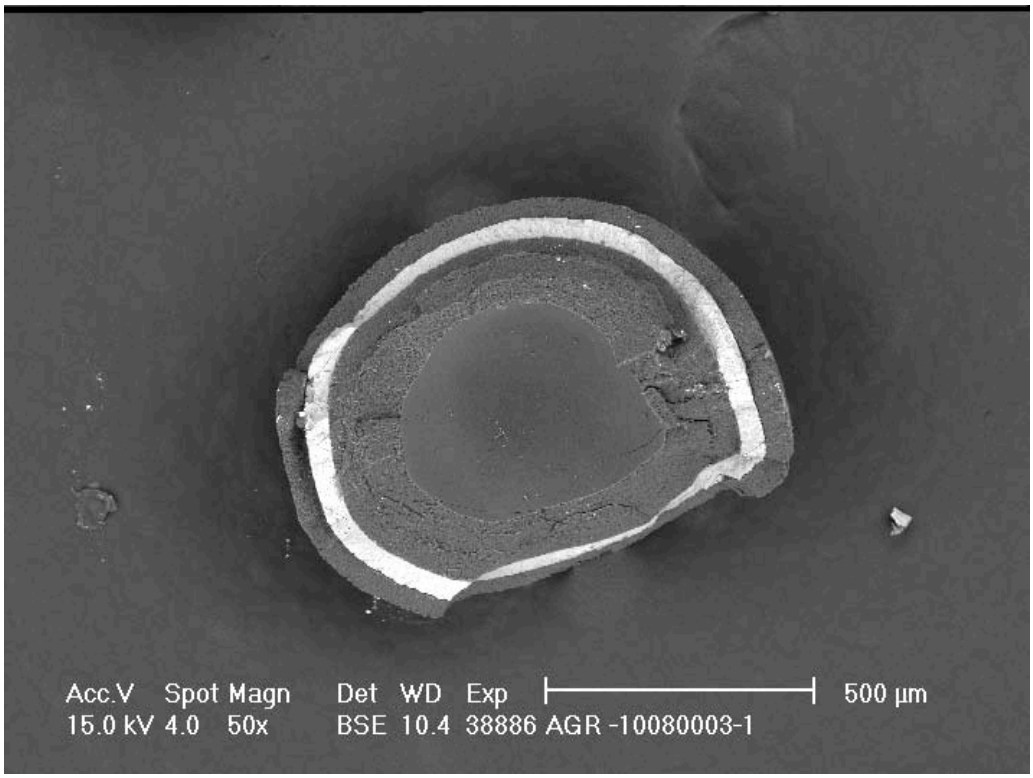

Figure 1-16: German fuel coating fragment separated at kernel/buffer interface.

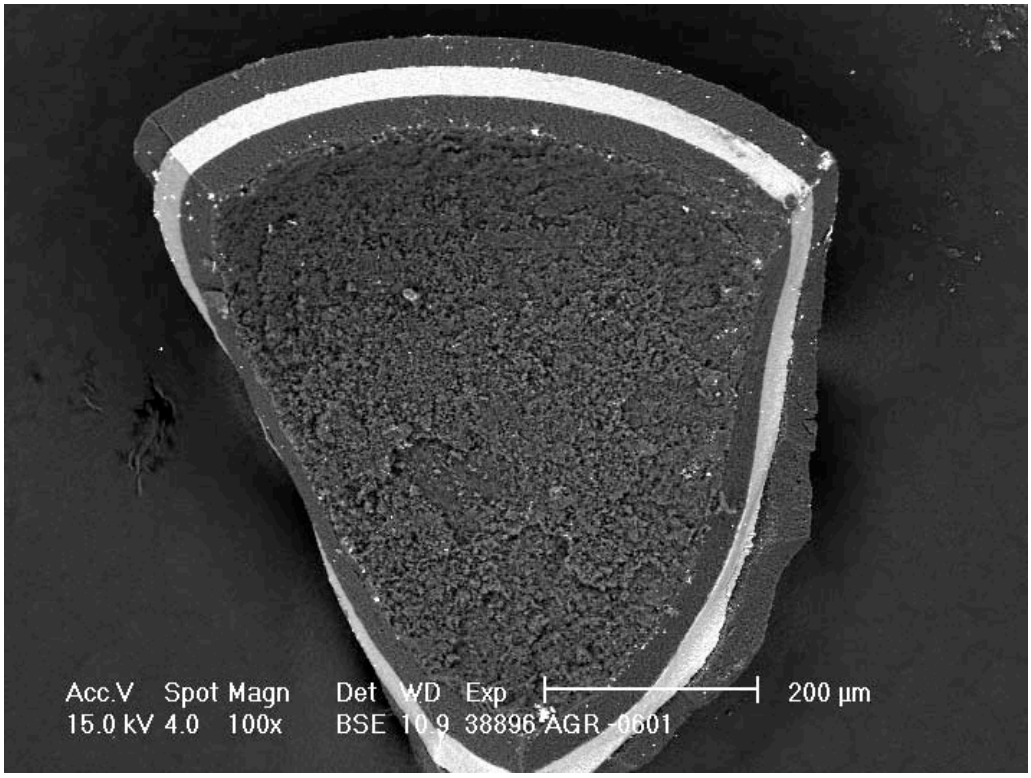

Figure 1-17: German fuel fragment separated at buffer/IPyC interface.

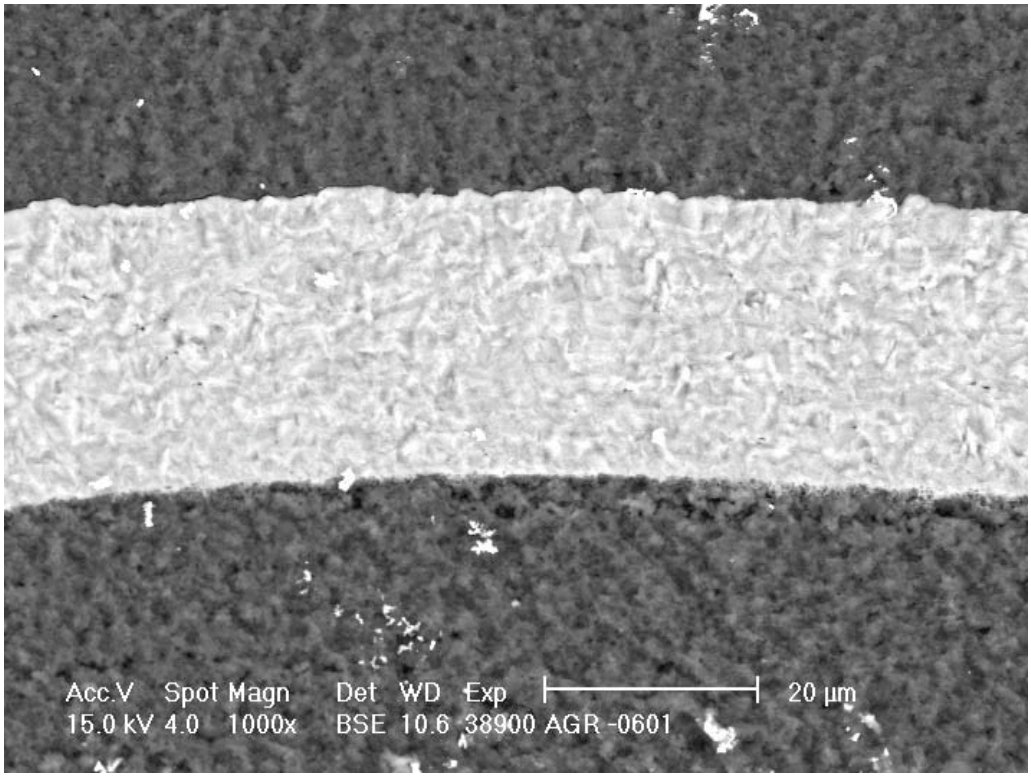

Figure 1-18: German fuel IPyC/SiC/OPyC, compare to Figure 1-8 and Figure 1-14.

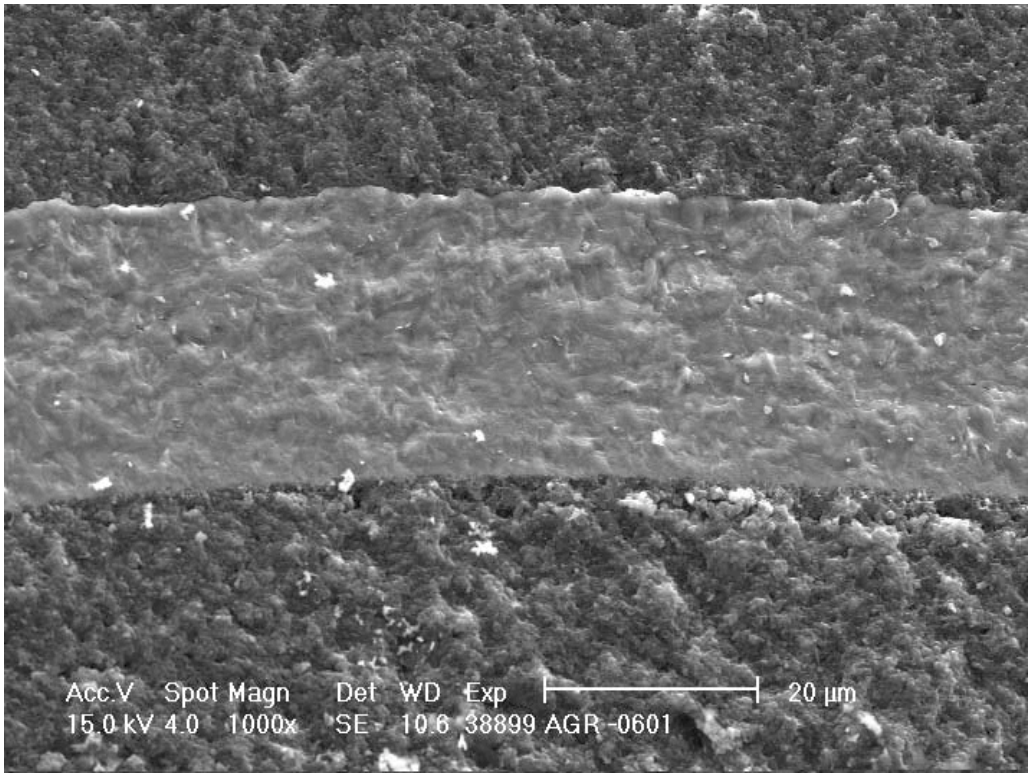

Figure 1-19: German fuel IPyC/SiC/OPyC, compare to Figure 1-9.

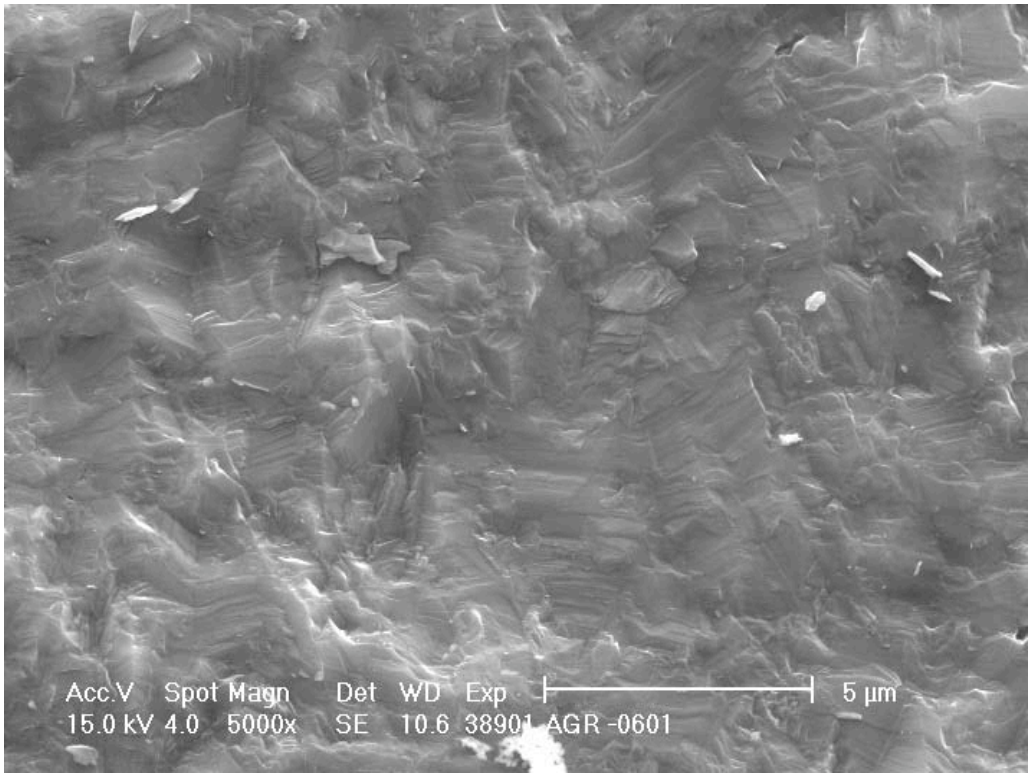

Figure 1-20: German fuel SiC fracture surface, compare to Figure 1-10**.**

2 Measurement of Size and Shape Using Shadowgraphy

J.D. Hunn, A.K. Kercher, and J.R. Price

2.1 Size and shape of kernels

A sufficient number of kernels could not be extracted from the coated particles to determine size and shape by the preferred shadow imaging technique. Size and shape of the kernels was measured on cross sectioned samples instead. The data is reported in section 3.1.

2.2 Size and shape of coated particles

Shadow images were obtained for a random orientation of 1375 coated particles riffled from AGR-10. Image analysis software was used to find the center of each kernel and identify 360 points around the perimeter. The uncertainty for this measurement was ±1 μm. This data was then compiled to report aspect ratio (maximum radius/minimum radius), mean radius, standard deviation in radius, maximum radius, and minimum radius for each particle measured. The summary data from each particle in the sample was then compiled to obtain the average, standard deviation, maximum, and minimum of the individual particle quantities (aspect ratio, mean radius, standard deviation in radius, maximum radius, and minimum radius). Figure 2-1 contains the compiled data and shows the distributions of the aspect ratio and mean particle radius. The histogram labels correspond to the maximum value in that bin (top of bin). The same data was also computed in terms of diameter by measuring the distance between perimeter points that were separated by 180°. These values are summarized in Figure 2-2. The average and standard deviation of the mean diameter were exactly twice the values obtained for the mean radius. This showed that the statistical measurement for the size distribution was equivalent for the two methods. The aspect ratio calculated using maximum and minimum radii was more sensitive to the faceting and non-symmetrical shapes observed in the sample of HRB-21 particles. A higher average and standard deviation was observed than for the ratio calculated from the diameter.

The measured particles had an average mean radius of 399 μm with a standard deviation in the distribution of 13 μm. Based on variable sampling statistics using a two-sided student's t distribution (t=1.96), the average mean radius of the HRB-21 particles was 398-400 μm with 95% confidence. Applying a two-sided tolerance factor test (K=2.6), the critical range satisfied by 99% of the batch was 365-433 μm with 95% confidence. Applying a one-sided tolerance factor test (K=2.4), the critical range satisfied by 98% of the batch (1% above and 1% below) was 368-430 μm with 95% confidence. The largest particle measured had a mean radius of 446 μm. The smallest particle had a mean radius of 328 μm.

	Rmax/Rmin	Mean Radius	St. Dev. In Radius	Minimum Radius	Maximum Radius
Average	1.11	399	10	378	418
Standard Deviation	0.03	13	3	15	14
Minimum	1.03	328	3	313	339
Maximum	1.22	446	23	427	464

Rmax/Rmin	*Frequency*
1	0
1.01	0
1.02	0
1.03	0
1.04	1
1.05	4
1.06	25
1.07	83
1.08	115
1.09	178
1.1	197
1.11	205
1.12	147
1.13	126
1.14	94
1.15	71
1.16	52
1.17	33
1.18	17
1.19	12
1.2	9
1.21	2
1.22	3
1.23	1
More	0

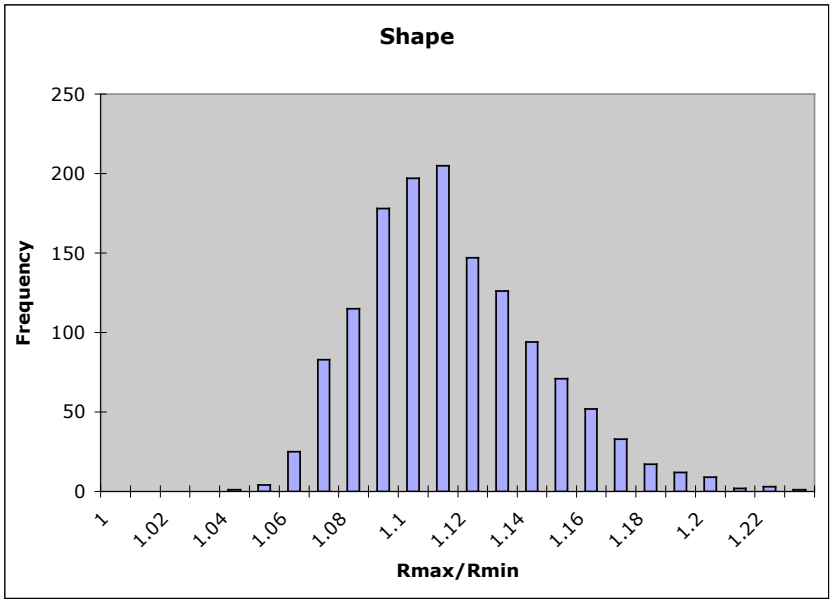

Mean Radius	*Frequency*
325	0
330	1
335	0
340	0
345	0
350	0
355	0
360	0
365	4
370	10
375	21
380	56
385	93
390	150
395	206
400	169
405	224
410	165
415	126
420	72
425	43
430	20
435	11
440	2
445	1
450	1
More	0

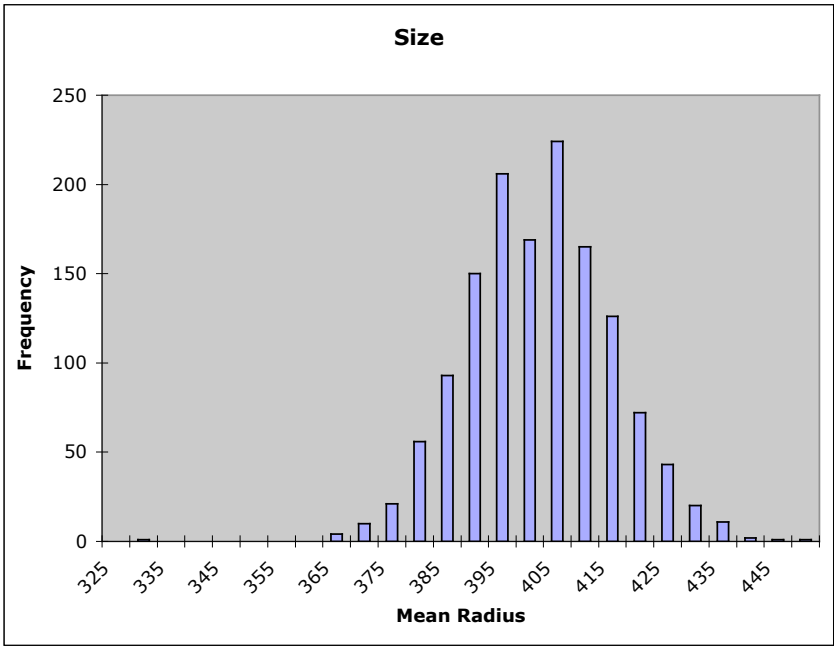

Figure 2-1: Size and shape summary for 1375 coated particles. Measurements are distance from best circle fit center to edge in μm.

	Dmax/Dmin	Mean Diameter	St. Dev. In Diameter	Minimum Diameter	Maximum Diameter
Average	1.07	798	15	771	824
Standard Deviation	0.02	26	5	28	28
Minimum	1.02	652	3	641	664
Maximum	1.19	889	43	868	923

Dmax/Dmin	*Frequency*
1	0
1.01	0
1.02	4
1.03	15
1.04	86
1.05	168
1.06	225
1.07	268
1.08	214
1.09	166
1.1	100
1.11	54
1.12	40
1.13	13
1.14	8
1.15	11
1.16	1
1.17	1
1.18	0
1.19	1
1.2	0
More	0

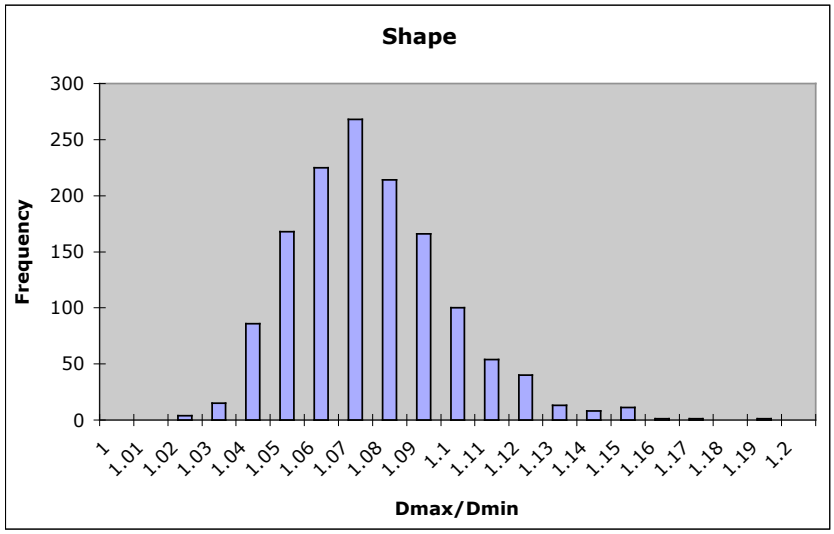

Mean Diameter	*Frequency*
650	0
660	1
670	0
680	0
690	0
700	0
710	0
720	0
730	6
740	8
750	25
760	53
770	93
780	151
790	197
800	174
810	225
820	169
830	117
840	74
850	48
860	17
870	12
880	3
890	2
900	0
More	0

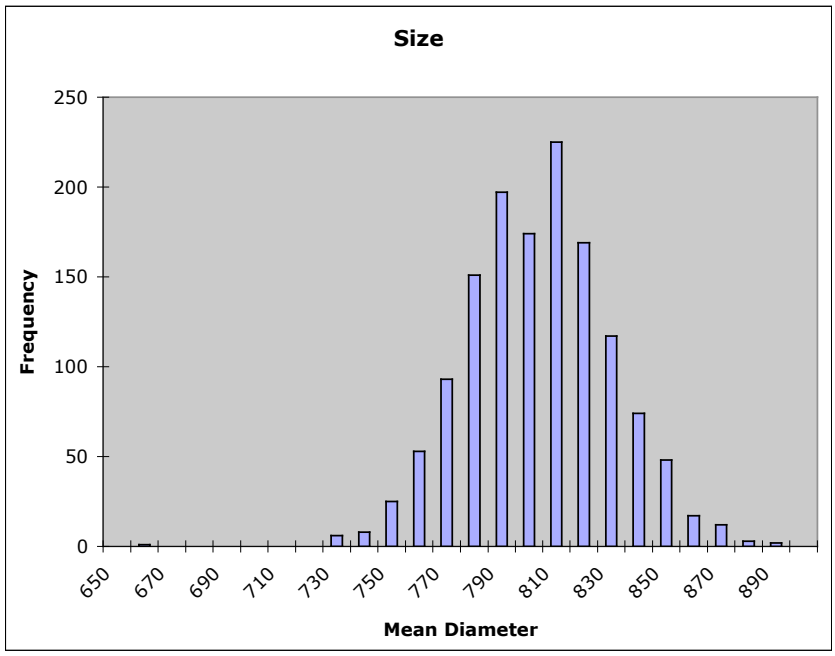

Figure 2-2: Size and shape summary for 1375 coated particles. Measurements are in μm from edge to edge through best circle fit center.

The HRB-21 particles were highly faceted. The average R_{max}/R_{min} aspect ratio was 1.11. Figure 2-3 shows additional ways of considering deviations from a spherical shape. The local radius of curvature was calculated by performing a Kasa circle fit on 30° segments around the perimeter of the image. A radius of curvature that is small compared to the average radius indicates a sharp corner. A radius of curvature that is large indicates a "flat." The particles showed a tendency to exhibit numerous "flats." Note that these features that appeared as "flats" in the shadowgraphs are likely dimples, and appeared to be related to buffer defects.

The mean and maximum deviations in radius from the best fit radius are also reported in Figure 2-3. A large deviation indicates a non-spherical shape. Figure 2-4 shows some typical coated particles from the batch. A high degree of faceting was observed for these particles.

	Minimum Radius of Curvature	Maximum Radius of Curvature	Mean Deviation in Radius	Maximum Deviation in Radius
Average	237	961	8	17
Standard Deviation	33	347	2	6
Minimum	60	424	3	6
Maximum	329	2744	19	49

Ave. Mean Radius = 399

Minimum Radius of Curvature	*Frequency*
50	0
70	4
90	4
110	0
130	1
150	3
170	18
190	53
210	179
230	294
250	348
270	260
290	143
310	56
330	12
350	0
More	0

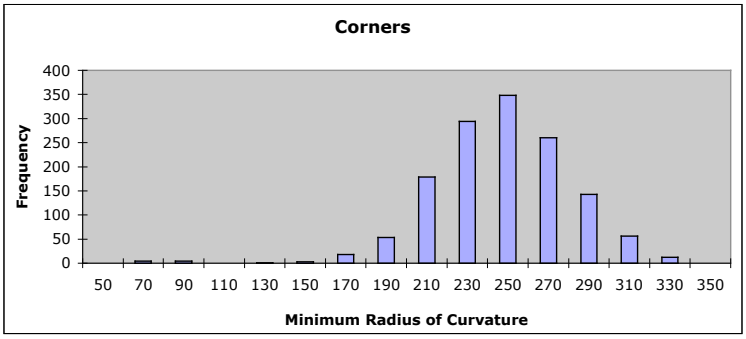

Maximum Radius of Curvature	*Frequency*
0	0
100	0
200	0
300	0
400	0
500	18
600	107
700	202
800	210
900	193
1000	161
1100	104
1200	87
1300	73
1400	63
1500	43
1600	27
1700	32
1800	14
1900	12
2000	12
2100	6
2200	4
2300	3
2400	1
2500	1
2600	1
2700	0
2800	1
2900	0
3000	0
More	0

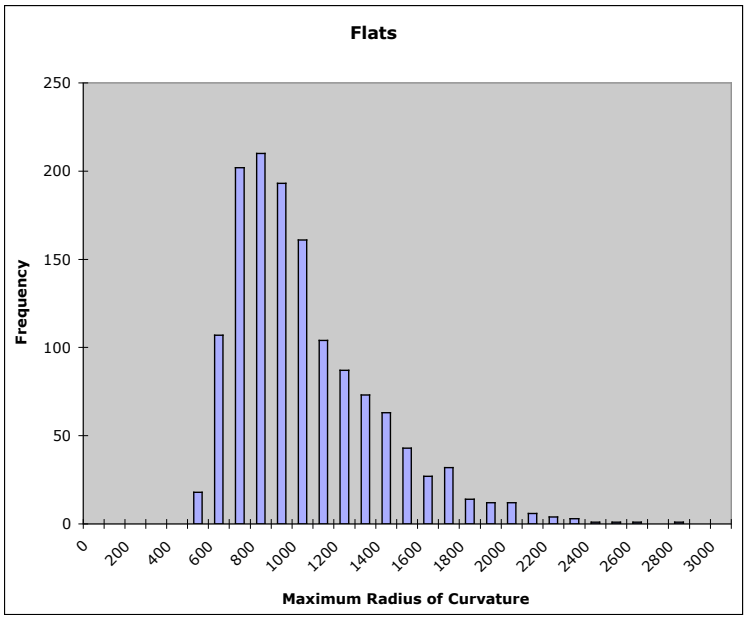

Figure 2-3: Other methods of measuring shape. Radii are in μm.

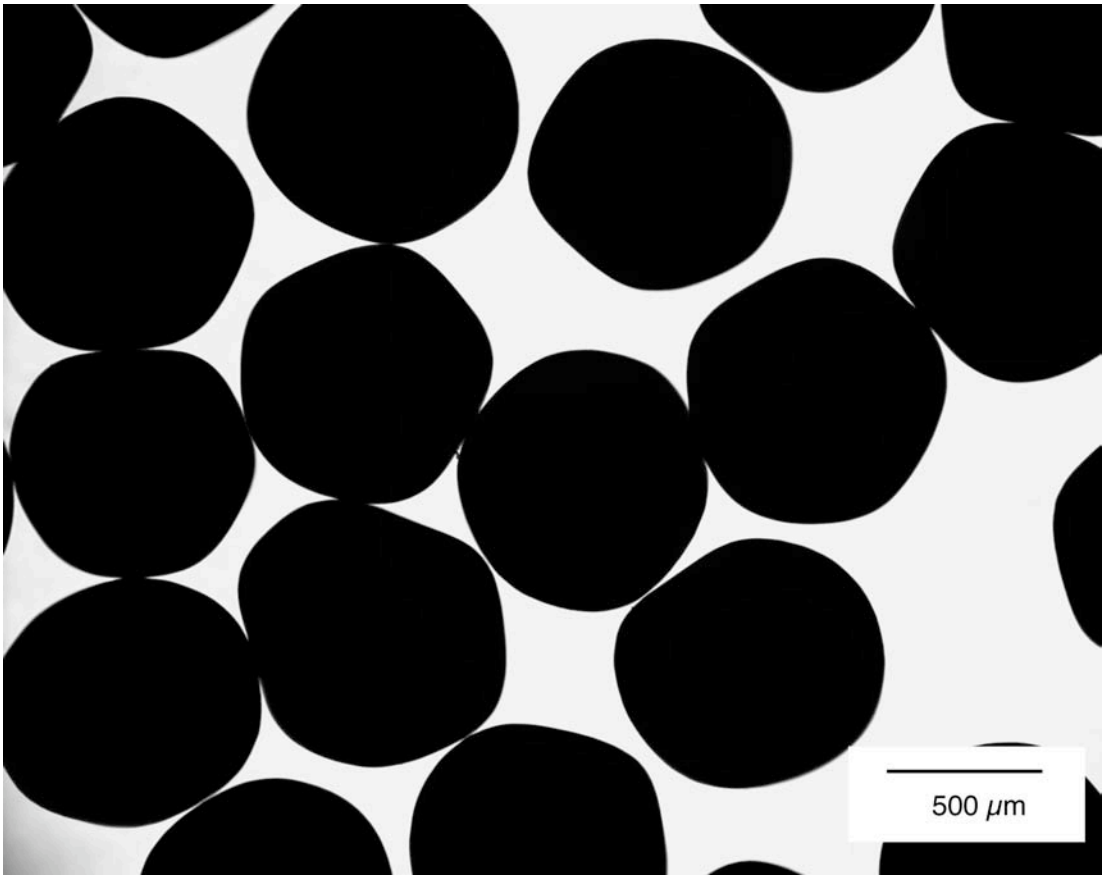

Figure 2-4: HRB-21 coated particles.

3 Measurement of Coating Thicknesses

J.D. Hunn, A.K. Kercher, and J.R. Price

Coating thicknesses were measured on 144 particles by mounting particles in a clear epoxy and grinding and polishing the particles to close to, but not beyond, the midpoint. The polished cross sections were imaged in bright field reflected mode with a computer-automated optical microscope and the images were computer analyzed to extract the thickness information for each layer. The deviation of the measured layer thickness from the actual layer thickness due to the polished cross section not being exactly at a midplane was corrected by measuring the outer diameter of the particle and applying a geometric correction. The outer diameter was measured by backlighting the clear epoxy mount to obtain a shadow image of the particle in addition to the bright field reflected image.

Extensive porosity in the kernels and badly faceted coated particles made the image analysis difficult. Figure 3-1 shows some of the images used for the coating thickness analysis. The image analysis algorithms were adjusted to work with the abnormal kernels. The faceting of the particles resulted in incomplete identification of the outer diameter of the particles in the correction for deviation of the cross section from midplane. Because the midplane could not be well defined, an additional uncertainty was introduced. This was, especially true for the kernel measurements, where this correction was the greatest.

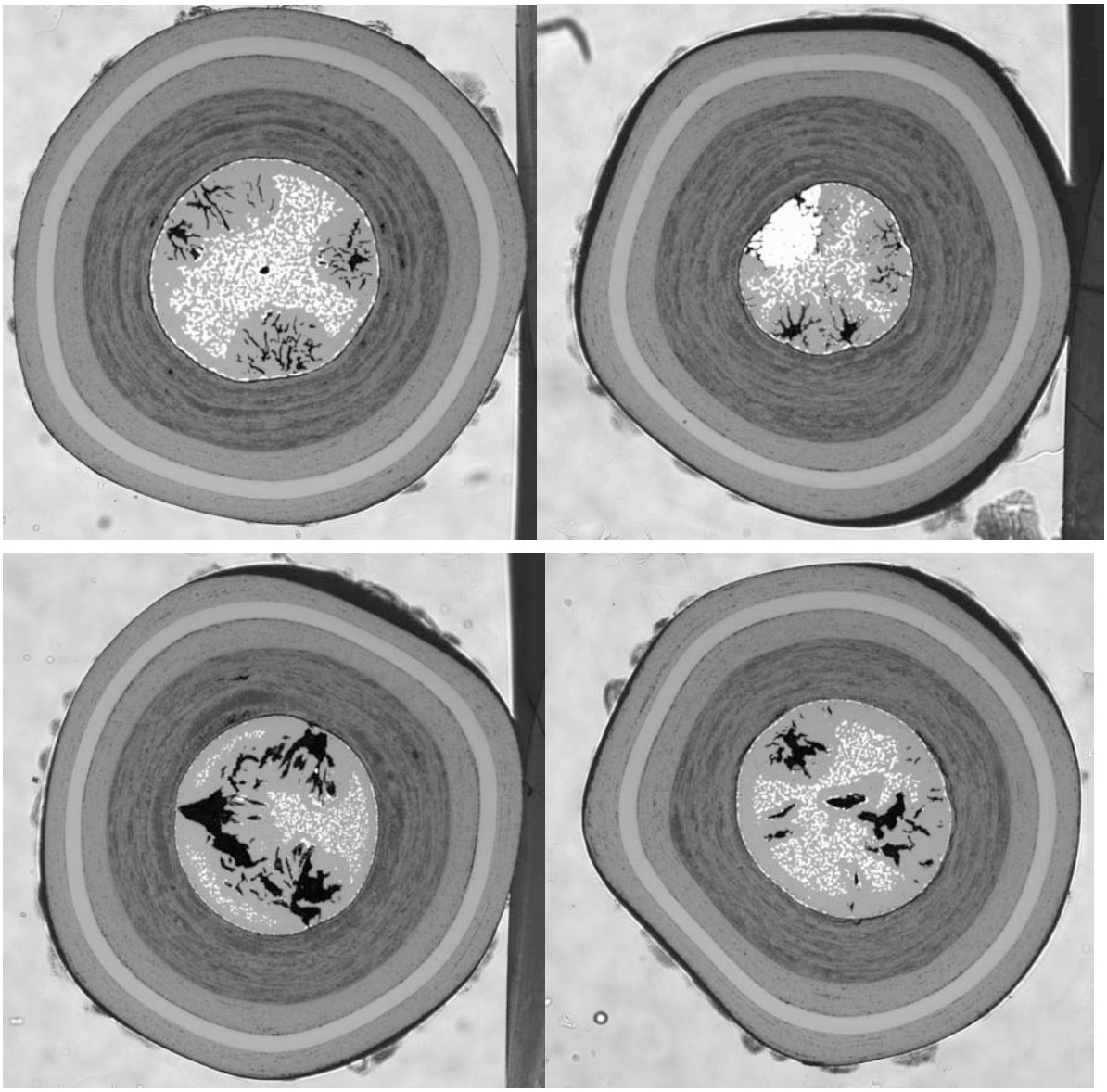

Figure 3-1: HRB-21 particle cross-sections.

3.1 Kernel diameter

Kernel diameter was determined by cross section analysis. This is not the preferred method for determination of kernel size and shape, but the kernels could not be easily extracted from the coatings as in the case of the German coated 500 μm UO_2 analyzed previously (see ORNL/CF-04/06). There is a much larger uncertainty in determining size and shape of the kernels by cross section when compared to using shadowgraphic methods. The deviation from midplane was corrected, as noted above, however, the associated error in this correction was greater than it was for the coatings due to the fact that the kernel edge was closer to the geometric center of the particle and to the fact that the kernels may have been off center in some cases. In addition, there was usually a gap between the kernel and the buffer that increased the uncertainty in the location of that interface.

Figure 3-2 shows the data summary for the kernel radius. The histogram labels correspond to the maximum value in that bin (top of bin). The average mean radius was 186 μm with a standard deviation of 9 μm. The average R_{max}/R_{min} was 1.04. The aspect ratio was adjusted by –0.01 to correct for a systematic offset error associated with extracting a ratio of a maximum value over a minimum value (this is discussed in depth in ORNL/CF-04/07). Based on variable sampling statistics using a two-sided student's t distribution (t=1.97), the average mean diameter of the HRB-21 kernels was 369-375 μm with 95% confidence. Applying a two-sided tolerance factor test (K=2.86), the critical range satisfied by 99% of the batch was 321-423 μm with 95% confidence. Applying a one-sided tolerance factor test (K=2.61), the critical range satisfied by 98% of the batch (1% above and 1% below) was 325-419 μm with 95% confidence. These values appear to be high compared to the specification and previous measurements. Based on sampling statistics using a binomial distribution, the kernels would not pass a 1.05 control limit on the aspect ratio for less than a 42% tolerance limit at 95% confidence.

	Rmax/Rmin	Mean Radius	Stnd. Dev. In Radius	Minimum Radius	Maximum Radius
Average	1.04	186	2.4	181	191
Standard Deviation	0.02	9	1.2	9	9
Maximum	1.11	211	6.5	208	215
Minimum	1.00	160	0.5	155	165

Sphericity	*Frequency*
1	0
1.01	4
1.02	21
1.03	26
1.04	20
1.05	22
1.06	20
1.07	9
1.08	8
1.09	8
1.1	4
1.11	2
More	0

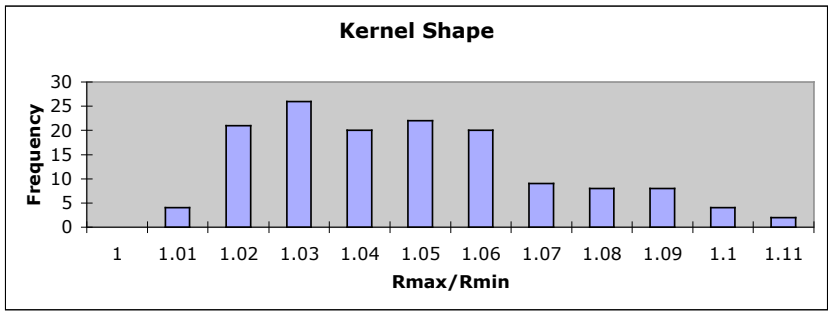

Mean Radius	*Frequency*
155	0
160	0
165	2
170	4
175	9
180	20
185	28
190	35
195	26
200	10
205	7
210	2
215	1
More	0

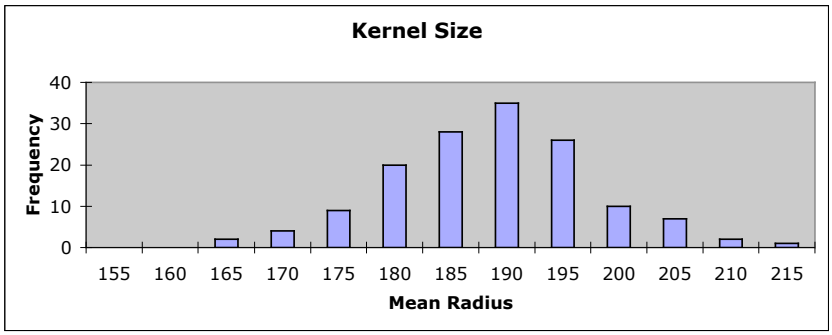

Figure 3-2: Data summary for kernel radius from cross section measurement. Radii are in μm.

3.2 Buffer thickness

Figure 3-3 shows the data summary for the measurements made on the buffer. The average mean buffer thickness was 105 μm with a standard deviation in the distribution of 12 μm. Based on variable sampling statistics using a two-sided student's t distribution (t=1.97), the average mean thickness of the buffer in this lot of particles was 103-107 μm with 95% confidence. The thickest point measured in a buffer layer was 151 μm. The thinnest point measured in a buffer layer was 70 μm. The thinnest mean thickness measured was 78 μm. Applying a one-sided tolerance factor test (K=2.61), the critical limit at 1% tolerance for minimum mean buffer thickness of the batch was 74 μm with 95% confidence.

	Mean Thickness	Stnd. Dev. In Thickness	Maximum Thickness	Minimum Thickness
Average	105	3.9	114	96
Standard Deviation	12	1.0	13	12
Maximum	139	7.1	151	131
Minimum	78	1.8	86	70

Mean Thickness	*Frequency*
75	0
80	2
85	3
90	14
95	9
100	24
105	32
110	17
115	14
120	11
125	12
130	3
135	0
140	3
More	0

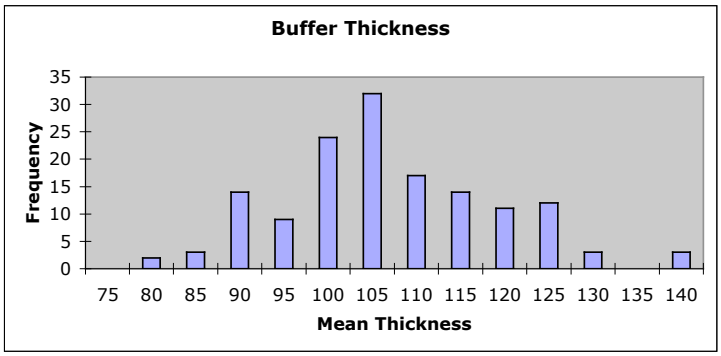

Figure 3-3: Data summary for buffer thickness. Thicknesses are in μm.

3.3 IPyC thickness

Figure 3-4 shows the data summary for the measurements made on the IPyC. The average mean IPyC thickness was 46 μm with a standard deviation in the distribution of 3 μm. Based on variable sampling statistics using a two-sided student's t distribution (t=1.97), the average mean IPyC thickness of the HRB-21 particles was 45-47 μm with 95% confidence. The thickest point measured in an IPyC layer was 61 μm. The thinnest point measured in an IPyC layer was 30 μm. Applying a two-sided tolerance factor test (K=2.86), the critical range satisfied by 99% of the batch was 37-55 μm with 95% confidence. Applying a one-sided tolerance factor test (K=2.61), the critical range satisfied by 98% of the batch (1% above and 1% below) was 38-54 μm with 95% confidence.

There was not sufficient contrast and resolution to resolve the seal coat as a separate layer at the magnification used for this analysis. The reported IPyC thickness included the thickness of the seal coat. The seal coat was about 3 μm thick.

	Mean Thickness	Stnd. Dev. In Thickness	Maximum Thickness	Minimum Thickness
Average	46	3.3	54	39
Standard Deviation	3	0.6	3	3
Maximum	54	4.8	61	47
Minimum	40	1.8	44	30

Mean Thickness	*Frequency*
40	1
41	1
42	4
43	11
44	11
45	20
46	19
47	19
48	18
49	13
50	11
51	10
52	3
53	2
54	0
55	1
More	0

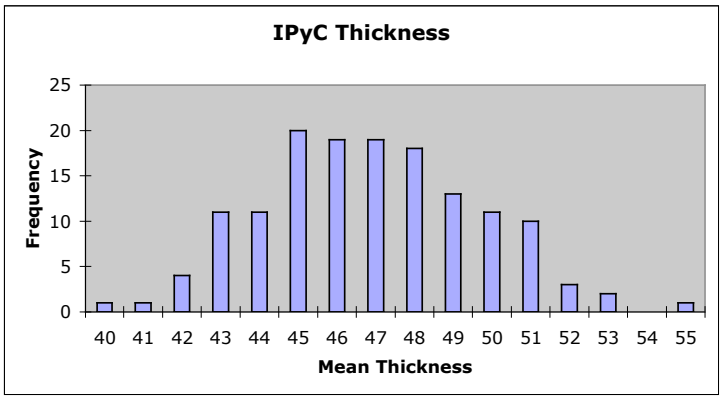

Figure 3-4: Data summary for IPyC thickness. Thicknesses are in μm.

3.4 SiC thickness

Figure 3-5 shows the data summary for the measurements made on the SiC. The average mean SiC thickness was 26.8 μm with a standard deviation in the distribution of 0.6 μm. This indicated a very uniform SiC deposition throughout the lot. Based on variable sampling statistics using a two-sided student's t distribution (t=1.97), the average mean SiC thickness of the HRB-21 particles was 26.7-26.9 μm with 95% confidence. The thickest point measured in a SiC layer was 30.7 μm. The thinnest point measured in a SiC layer was 23.1 μm. Applying a one-sided tolerance factor test (K=2.61), the critical limit at 1% tolerance for minimum SiC thickness of the batch was 25.2 μm with 95% confidence. The maximum standard deviation in thickness around a SiC layer was only 1.13 μm. This indicated that the SiC layers were very uniform in thickness on each particle.

	Mean Thickness	Stnd. Dev. In Thickness	Maximum Thickness	Minimum Thickness
Average	26.8	0.73	28.7	25.0
Standard Deviation	0.6	0.14	0.8	0.8
Maximum	28.4	1.13	30.7	26.7
Minimum	25.1	0.40	26.4	23.1

Mean Thickness	*Frequency*
25	0
25.25	3
25.5	1
25.75	3
26	5
26.25	11
26.5	16
26.75	21
27	28
27.25	25
27.5	19
27.75	6
28	4
28.25	1
28.5	1
More	0

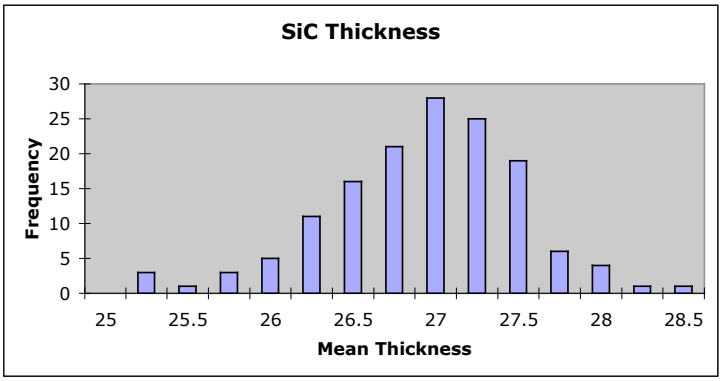

Figure 3-5: Data summary for SiC thickness. Thicknesses are in μm.

3.5 OPyC thickness

Figure 3-6 shows the data summary for the measurements made on the OPyC. The average mean OPyC thickness was 40 μm with a standard deviation in the distribution of 3 μm. Based on variable sampling statistics using a two-sided student's t distribution (t=1.97), the average mean OPyC thickness of the HRB-21 particles was 39-41 μm with 95% confidence. The thickest point measured in an OPyC layer was 56 μm. The thinnest point measured in an OPyC layer was 26 μm. Applying a one-sided tolerance factor test (K=2.61), the critical limit at 1% tolerance for minimum OPyC thickness of the batch was 32 μm with 95% confidence.

	Mean Thickness	Stnd. Dev. In Thickness	Maximum Thickness	Minimum Thickness
Average	40	3.9	48	31
Standard Deviation	3	0.8	3	3
Maximum	47	6.7	56	42
Minimum	33	2.3	38	26

Mean Thickness	*Frequency*
33	0
34	2
35	3
36	7
37	8
38	17
39	17
40	23
41	24
42	19
43	9
44	10
45	2
46	2
47	0
48	1
More	0

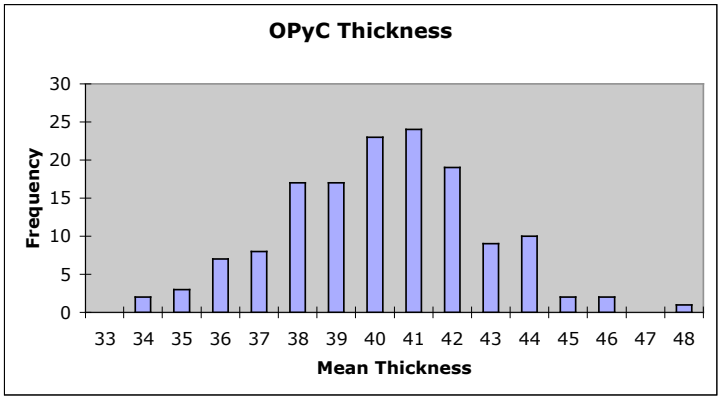

Figure 3-6: Data summary for OPyC thickness. Thicknesses are in μm.

3.6 Total particle radius

The mean kernel radius and mean layer thickness data were summed for each particle as a comparison check against the data obtained from the whole particle shadowgraphy measurements made in section 2.2. The average mean radius obtained by summing the data from the cross section measurements was 404 μm with a standard deviation in the distribution of 13 μm (Figure 3-7). This agreed fairly well with the data obtained by shadow imaging the whole particles summarized in Figure 2-1 (399 ± 13 μm), especially considering the difficulties in measurement associated with the very odd shapes of the particles. The average R_{max}/R_{min} aspect ratio was the same as measured by shadowgraphy. The fully coated particles were not very spherical.

	Rmax/Rmin	Mean Radius
Average	1.11	404
Standard Deviation	0.03	13
Maximum	1.18	443
Minimum	1.05	371

Rmax/Rmin	*Frequency*
1.05	1
1.06	2
1.07	8
1.08	9
1.09	18
1.1	21
1.11	16
1.12	19
1.13	21
1.14	13
1.15	6
1.16	6
1.17	3
1.18	1
1.19	0
More	0

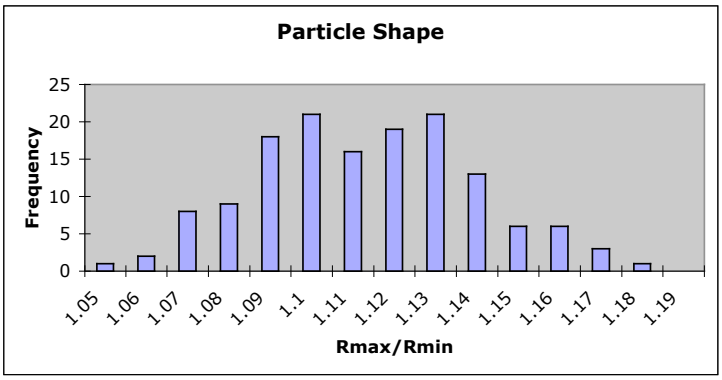

Mean Radius	*Frequency*
370	0
375	1
380	0
385	9
390	12
395	21
400	17
405	20
410	25
415	11
420	12
425	8
430	3
435	0
440	3
445	2
More	0

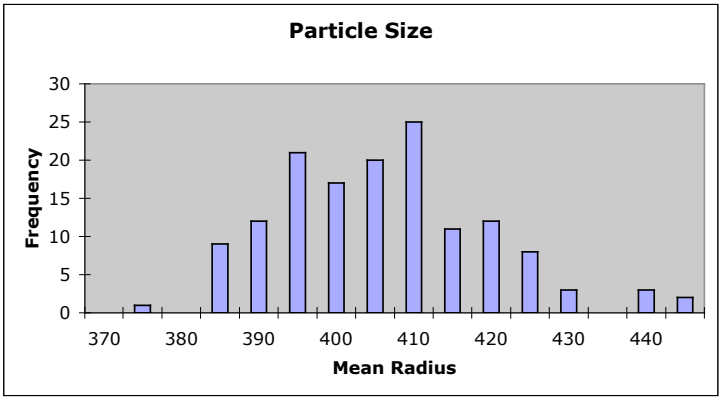

Figure 3-7: Data summary for total particle radius calculated from sum of kernel radius and layer thicknesses. Radii are in μm.

4 Density Measurement

P.J. Pappano and J.D. Hunn

4.1 Kernel density

Using the ASTM D3766 standard terminology, we define three different types of density: the *theoretical density* is based solely on the solid material volume, the *skeletal density* includes the closed pore volume, and the *envelope density* includes the open and closed pore volume. The theoretical density of UO_2 is 10.96 g/cc. The theoretical density of UC_2 is 11.28 g/cc. The theoretical density of UC is 13.63 g/cc.

The UCO kernels could not be separated from the coatings sufficiently to perform a density measurements.

4.2 Buffer and IPyC density

The buffer and IPyC layers could not be isolated from the coated particles. The density was not measured.

4.3 SiC density

Coatings were broken off of the particles as described in section 1. Pieces of IPyC/SiC fragments were removed and heated in air at 750°C for 90 min to remove the carbon layers. The separated SiC fragments were placed in a liquid gradient density column spanning a range of 3.15-3.21 g/cc. The column was created using an appropriate combination of methylene iodide and bromoform in such a way as to create a linear density gradient. Six calibration floats were used to generate a density versus position linear fit for the column and the density of the SiC fragments was calculated after measuring their equilibrium position in the column. Figure 4-1 shows the column calibration and measured values for the SiC fragments. The average density measured by this method was 3.206±0.002 g/cc. The 95% confidence interval for the average SiC density by this method was 3.205-3.207 g/cc. A rigorous uncertainty analysis has not yet been performed for the density column characterization of SiC, but it is expected to be around ±0.001-0.002 g/cc. The density measured by this technique is expected to have a value between the envelope density and the skeletal density, depending on the porosity of the material and the extent to which the liquid penetrates the open pores. The SiC had very little porosity, so there should be little difference between the envelope density and the skeletal density.

AGR-10-01-02 SiC

Calibrated Floats

Density	Top of Float	Bottom of Float	Float Position
3.150	75.54	98.27	86.91
3.170	213.18	235.63	224.41
3.190	348.38	370.02	359.20
3.200	417.95	437.44	427.70
3.200	430.71	430.71	430.71
3.210	491.44	514.28	502.86

Linear Fit

slope	intercept
1.45E-04	3.14E+00

Particle Number	Particle Position	Calculated Density
1	435.16	3.201
2	440.17	3.201
3	441.55	3.202
4	470.33	3.206
5	472.45	3.206
6	474.59	3.206
7	475.67	3.207
8	479.79	3.207
9	471.73	3.206
10	471.25	3.206
11	475.14	3.206
12	474.44	3.206
13	479.88	3.207
14	481.88	3.207
15	483.27	3.208
16	488.56	3.208
17	491.37	3.209
18	494.97	3.209
19	487.69	3.208
20	479.04	3.21

Average Density 3.206
Standard Deviation 0.002

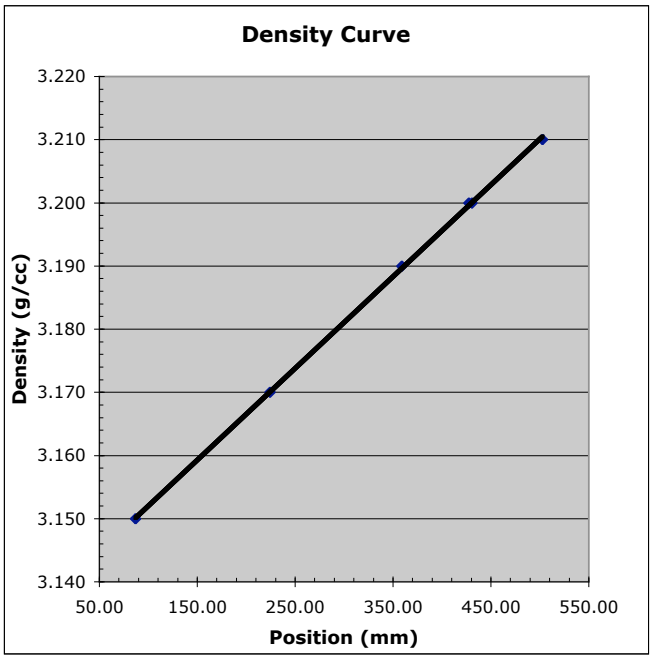

Figure 4-1: Density column data report for SiC. Densities are in g/cc.

4.4 OPyC density

Coatings were broken off of the particles as described in section 1. Pieces of free OPyC fragments were removed. The separated OPyC fragments were placed in a liquid gradient density column spanning a range of 1.7-2.1 g/cc. The column was created using an appropriate combination of ethylene bromide and tetrachloroethylene in such a way as to create a linear density gradient. The column was not quite linear over the entire range so only the central three calibration floats were used to generate a density versus position linear fit for the column that spanned the range of the unknown. The density of the OPyC fragments was calculated after measuring their equilibrium position in the column. Figure 4-2 shows the column calibration and measured values for the OPyC fragments. The average density measured by this method was 1.925±0.012 g/cc. The 95% confidence interval for the average OPyC density by this method was 1.919-1.931 g/cc. A rigorous uncertainty analysis has not yet been performed for the density column characterization of OPyC, but it is expected to be around ±0.005 g/cc.

Calibrated Floats

Density	Float Position
1.70	2.52
1.80	201.56
1.91	370.04
2.00	507.75
2.10	616.24

Linear Fit

slope	intercept
6.52E-04	1.67E+00

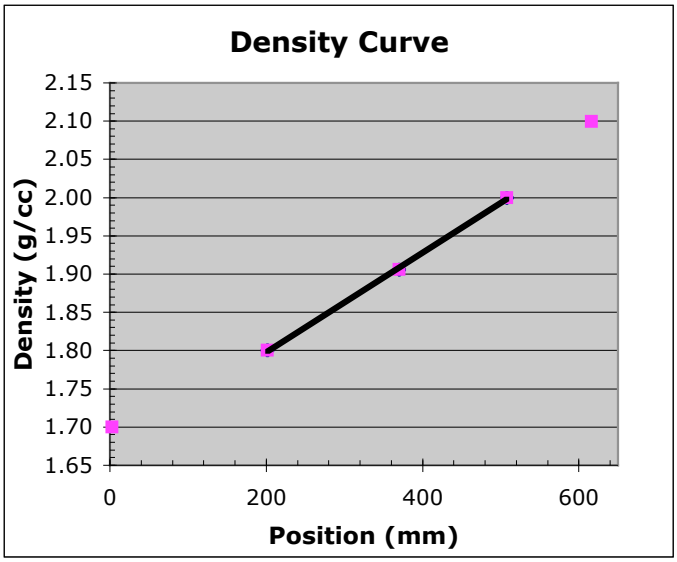

Particle Number	Particle Position	Calculated Density
1	362.04	1.904
2	364.06	1.905
3	377.74	1.914
4	379.30	1.915
5	383.73	1.918
6	390.23	1.922
7	398.23	1.927
8	405.86	1.932
9	410.64	1.935
10	423.63	1.944
11	368.31	1.908
12	371.44	1.910
13	375.51	1.912
14	402.65	1.930
15	405.02	1.932
16	406.95	1.933
17	409.87	1.935
18	424.20	1.944
19	409.86	1.935
20	408.72	1.934
21	405.48	1.932
22	400.58	1.929
23	395.10	1.925
Average Density		1.925
Standard Deviation		0.012

Figure 4-2: Density column data report for OPyC. Densities are in g/cc.

The density measured by this technique is expected to have a value between the envelope density and the skeletal density, depending on the porosity of the material and the extent to which the liquid penetrates the open pores. Because the OPyC layers may be porous, it is not sufficient to simply measure the density using the liquid gradient density column. Therefore, OPyC envelope density was measured using a Hg porosimeter. The average envelope density of the OPyC layer was measured by first measuring the mass and envelope volume of the fully coated particles. After this measurement, all the particles were recovered, cleaned, heated at low temperature to remove the residual mercury, and heated in air at 750°C to remove the OPyC layer. The mass and envelope volume of the particles with the OPyC removed was then

measured and the mass and envelope volume of the OPyC calculated by subtraction. The accuracy of this measurement depended on not loosing any particles between measurements, fully removing the Hg between measurements, and low porosity in the SiC to prevent burnoff of the inner carbon layers. The measured buffer density of the OPyC layer by this method was 1.73 g/cc for a particle sample weighing 3.4 g.

The porosimetry measurement also provided data on the porosity of the OPyC and SiC layers. The OPyC open porosity was around 0.82%. No open porosity could be measured in the SiC. Figure 4-3 shows the high pressure curve (0 to 30,000 psi) for fully coated particles. The red line is the intrusion curve, where mercury is being forced into any open porosity by increasing the pressure. The blue curve is the extrusion curve, where pressure on the mercury is being reduced and the mercury is coming back out of the pores. The regions of large volume increase as a function of pressure correspond to mercury filling the intraparticulate volume (the open porosity). The pressure at which the open porosity is intruded indicates the size of the pores. Figure 4-4 shows the pore size distribution versus normalized pore volume calculated from the intrusion curve in Figure 4-3.

The Hg porosimeter results above are preliminary in that the uncertainty and repeatability of the porosimetry measurement has not yet been fully analyzed.

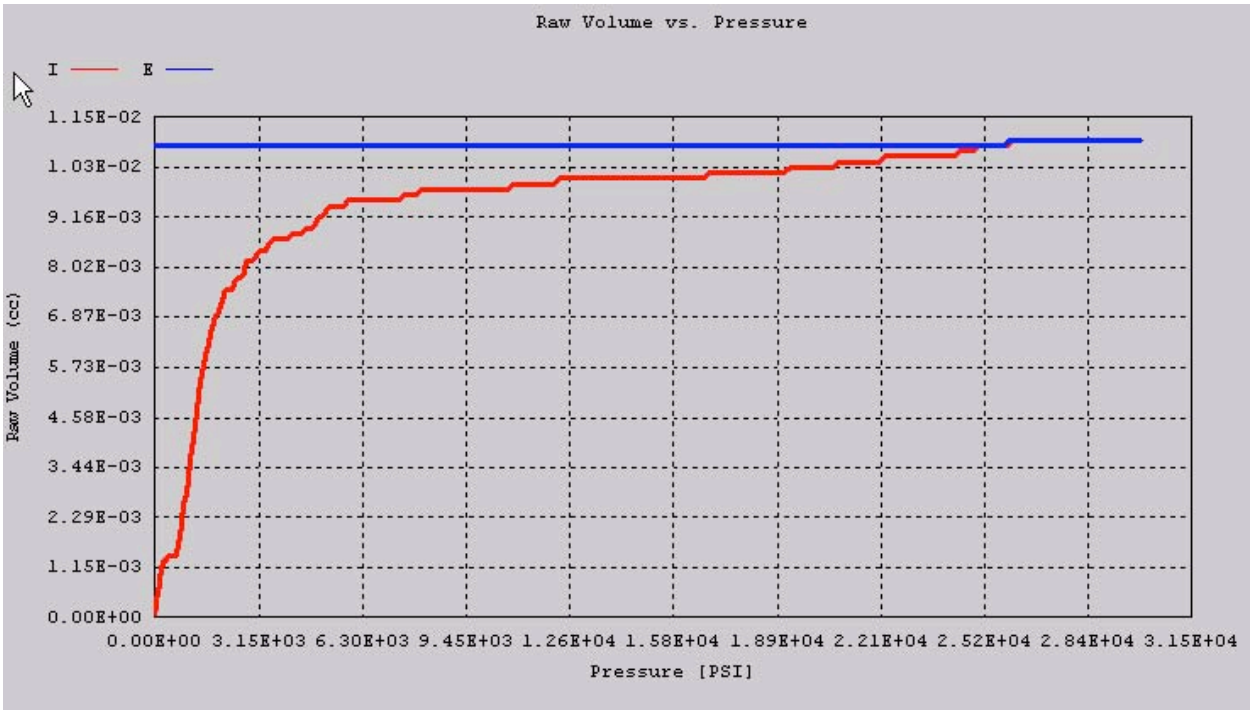

Figure 4-3: High pressure volume vs. pressure curve for fully coated particles.

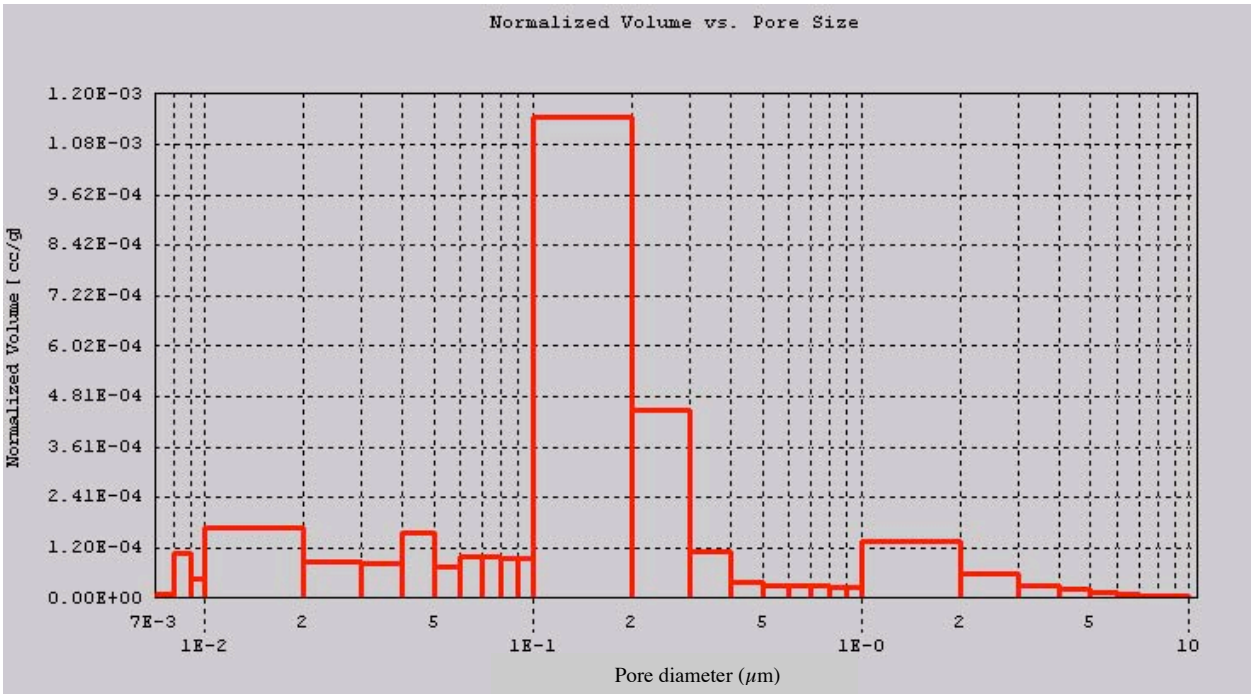

Figure 4-4: Pore size distribution in OPyC layer on fully coated particles.

4.5 Particle Density

A particle envelope density of 2.57 g/cc was obtained from the first half of the OPyC density measurement using the porosimeter. This measurement was not repeated and the result is preliminary in that the uncertainty and repeatability of the porosimetry measurement has not yet been fully analyzed.

5 Optical Anisotropy Measurements

G. E. Jellison, Jr. and J. D. Hunn

Particles were mounted and polished to reveal the individual coatings and a series of optical anisotropy measurements were made using the two-modulator generalized ellipsometry microscope (2-MGEM). The 2-MGEM measured the average Mueller matrix in a 10 μm diameter spot which was scanned over the specimen surface in two dimensions with a 10 μm step size in each direction. With this data, various optical anisotropy parameters could be imaged with a 10x10 μm per pixel resolution. A data set containing 2-MGEM data for 8,000 to 10,000 spots was generated for each particle.

Images produced by the 2-MGEM were analyzed using a software tool developed for this project which allowed for individual pixels in the image to be selected and added to different lists. Using this tool, data was grouped together for the kernel (used for final data normalization), the IPyC layer, the SiC layer, and the OPyC layer. Relevant optical parameters for each list of data points was then output on a data sheet such as that in Appendix A.

Data points can be selected using any of the optical parameter images. The diattenuation is often used, as was the case for the data analysis shown in Appendix A. In some cases, such as when the diattenuation is near zero, it is more convenient to use the reflected intensity image in order to be able to identify the individual layers. Any one of the pictures can be displayed in the data sheet.

Several relevant parameters were selected for observation: the diattenuation, the retardation, the circular diattenuation, the direction of the fast axis, the polarization factor, and the relative intensity of light reflecting from the sample. It was assumed that the diattenuation was the primary quantity, and it was set to be positive definite and was used to determine the direction of the fast axis.

In the data sheet, the average and standard deviation (SD) of the data in each list was calculated. The average error (that is, the average of the error limits for each of the selected parameters measured at each point) was also calculated. If there is a significant variation of the observed quantity around the layer, then the SD will be on the order of or greater than the average error, but if the quantity is uniform at all the selected points in the list, then the SD will be less than the average error.

For the particle shown in Appendix A, the SiC layer (saved list C) was optically isotropic by all measures. The diattenuation was indistinguishable from 0, as was the retardation and circular diattenuation. The direction of the fast axis was random, since it has little meaning for small values of optical anisotropy. Note, however, that for the SiC layer, the relationship (if any) between the optical anisotropy and anisotropy in the orientation of the crystallites is not yet well understood. In the PyC layers, the technique of characterizing crystalline anisotropy by measuring average optical anisotropy is based on the fact that the graphite structure possesses a high optical anisotropy. Certain polytypes of SiC (such as β-SiC) are optically isotropic, while other polytypes are hexagonal or rhombohedral and therefore optically anisotropic. Without

additional knowledge of the SiC microstructure, the observed optical isotropy of the SiC layer can not be related to the crystallographic orientation of the crystallites in the SiC layer.

For the particle shown in Appendix A, the IPyC layer (saved list A) had a significant diattenuation, N = 0.018±0.002. This corresponds to an optical anisotropy factor of 1.036±0.004 [OAF = (1+N)/(1-N) ≈ 1 + 2N]. There may have been some associated retardation in this layer, but it was not significantly different from 0. The circular diattenuation was 0 as well, within the error of the measurement. The direction of the fast axis (from -90° to +90°, corresponding to the direction of the a-b plane) was roughly perpendicular to the growth direction

There was a smaller amount of optical anisotropy in the OPyC layer (saved list F), again with the direction of the fast axis perpendicular to the growth direction. The diattenuation was 0.012±0.003 (OAF = 1.024±.005). This was 67% of the diattenuation measured for the IPyC layer. The amount of signal collected for this layer was a factor of 3-10 less than that reflected from the IPyC layer. This was due to the polished surface not being perfectly planar. The failure of the 2-MGEM to collect all of the reflected light did not introduce an absolute error, as it would for the old optical polarimeter technique, but it did increase the stochastic error because of the reduction in signal. This caused the image to be “noisier” for the OPyC layer and the uncertainty of each data point to be higher. Work is in progress to increase the signal to noise ratio by increasing the amount of analyzed light.

A total of 13 particles were analyzed with the 2-MGEM. Table 5-1 summarizes the diattenuation measurements. For all the particles, the average SiC diattenuation was not different from zero with respect to the average error. The average of the average diattenuation for the IPyC layers was 0.0186±.0010 (OAF = 1.037±0.002). The average of the average diattenuation for the OPyC layers was 0.0119±0.0011 (OAF = 1.024±0.002). The 95% confidence intervals for the OAF for the IPyC was 1.036-1.038 and for the OPyC was 1.023-1.025.

The measured anisotropy of the HRB-21 pyrocarbon layers was significantly higher than that previously measured by the 2-MGEM for the German reference material. A total of 12 particles of German fuel were measured. The average of the average diattenuation for the IPyC layers was 0.0140±.0016 (OAF = 1.028±0.003). The average of the average diattenuation for the OPyC layers was 0.0080±0.0010 (OAF = 1.016±0.002).

Table 5-1 : Diattenuation of HRB-21 Fuel

	IPyC			SiC			OPyC	
	Ave.	S. D.	Ave Error	Ave.	S. D.	Ave Error	Ave.	S. D.	Ave Error
	0.0184	0.0022	0.0032	0.0026	0.0018	0.0030	0.0112	0.0019	0.0030
	0.0166	0.0028	0.0031	0.0019	0.0008	0.0028	0.0107	0.0022	0.0034
	0.0196	0.0020	0.0031	0.0017	0.0006	0.0026	0.0108	0.0018	0.0038
	0.0185	0.0026	0.0035	0.0021	0.0015	0.0033	0.0111	0.0021	0.0043
	0.0179	0.0020	0.0034	0.0015	0.0009	0.0028	0.0122	0.0025	0.0046
	0.0177	0.0032	0.0033	0.0020	0.0010	0.0030	0.0101	0.0015	0.0043
	0.0176	0.0032	0.0033	0.0018	0.0008	0.0032	0.0125	0.0016	0.0042
	0.0186	0.0024	0.0030	0.0016	0.0007	0.0034	0.0126	0.0031	0.0046
	0.0197	0.0028	0.0030	0.0023	0.0013	0.0031	0.0125	0.0022	0.0044
	0.0199	0.0017	0.0035	0.0015	0.0009	0.0034	0.0140	0.0030	0.0059
	0.0196	0.0018	0.0030	0.0023	0.0012	0.0029	0.0122	0.0018	0.0041
	0.0197	0.0020	0.0030	0.0016	0.0009	0.0027	0.0135	0.0020	0.0040
	0.0184	0.0024	0.0033	0.0016	0.0010	0.0027	0.0118	0.0028	0.0049
Average	0.0186	0.0024	0.0032	0.0019	0.0010	0.0030	0.0119	0.0022	0.0043
S.D.	0.0010	0.0005	0.0002	0.0004	0.0003	0.0003	0.0011	0.0005	0.0007

Table 5-2 : Diattenuation of German Fuel

	IPyC			SiC			OPyC	
	Ave.	S. D.	Ave Error	Ave.	S. D.	Ave Error	Ave.	S. D.	Ave Error
	0.0134	0.0025	0.0032	0.0015	0.0009	0.0026	0.0077	0.0019	0.0040
	0.0140	0.0022	0.0029	0.0011	0.0006	0.0027	0.0077	0.0027	0.0040
	0.0160	0.0022	0.0034	0.0015	0.0007	0.0030	0.0083	0.0029	0.0046
	0.0127	0.0022	0.0037	0.0014	0.0008	0.0035	0.0078	0.0024	0.0040
	0.0129	0.0023	0.0038	0.0017	0.0011	0.0035	0.0089	0.0023	0.0044
	0.0174	0.0022	0.0031	0.0014	0.0008	0.0028	0.0097	0.0035	0.0036
	0.0138	0.0019	0.0028	0.0024	0.0011	0.0023	0.0086	0.0028	0.0045
	0.0122	0.0018	0.0028	0.0017	0.0006	0.0024	0.0071	0.0033	0.0036
	0.0159	0.0022	0.0033	0.0016	0.0012	0.0031	0.0089	0.0051	0.0037
	0.0133	0.0017	0.0028	0.0019	0.0009	0.0027	0.0074	0.0025	0.0046
	0.0125	0.0015	0.0027	0.0014	0.0010	0.0027	0.0062	0.0021	0.0032
	0.0137	0.0017	0.0028	0.0017	0.0009	0.0028	0.0074	0.0038	0.0039
Average	0.0140	0.0020	0.0031	0.0016	0.0009	0.0029	0.0080	0.0030	0.0040
S.D.	0.0016	0.0003	0.0004	0.0003	0.0002	0.0004	0.0010	0.0009	0.0004

6 Comparison to GA Data

J.J. Saurwein and J.D. Hunn

GA document DOE-HTGR-88357, Rev. C, "Capsule HRB-21 Preirradiation Report" contains the characterization data for fuel particle batch 8876-70-O, which was irradiated in the HRB-21 irradiation test. Table 9-1 provides a summary of the ORNL data for batch 8876-70 versus the GA data extracted from the GA report. As described in the introduction to this report, batches 8876-70-O and 8876-70 are identical through the OPyC coating layer.

Table 6-1: Comparison of ORNL and GA Data for HRB-21 Fissile Particles

Property	ORNL		GA	
	Mean	**95% Conf.**	**Mean**	**95% Conf.**
Particle diameter	798	796 – 800	811	ND
Average particle sphericity Rmax/Rmin	1.11	NA	NR	
Average particle sphericity Dmax/Dmin	1.07	NA	NR	
Kernel diameter	372	369 - 375	351	350 - 352
Buffer thickness	105	103 – 107	105	102 – 108
IPyC thickness	46	45 – 47	53	52 – 54
SiC thickness	26.8	26.7 – 26.9	32.6	32.2 – 33.0
SiC density	3.206	3.205 – 3.207	3.219	3.217 – 3.221
OPyC thickness	40	39 – 41	47	46 – 48
OPyC density (sink-float)	1.925	1.919 – 1.931	1.95	1.94 – 1.96
OPyC density (envelope)	1.73	ND	1.84	ND
IPyC BAFo	1.036	1.035 – 1.037	1.074	1.070 – 1.078
OPyC BAFo	1.024	1.023 – 1.025	1.038	1.035 – 1.041
SiC defect fraction	ND		1.5×10^{-6}	$<1.2 \times 10^{-5}$

NR = Not reported
NA = Not applicable
ND = Not determined

The difference between the ORNL and GA measurements for several of the properties in the above table is greater than can be accounted for by the reported 95% confidence values, which are computed only from random measurement errors (i.e., the measurement standard deviation). The 95% confidence values neglect systematic errors, which are concluded to be responsible for the observed differences. With regards to the particle diameter and coating thickness measurements, GA used x-radiography and ORNL uses ceramography/optical microscopy, which tend to have a positive measurement bias and a negative measurement bias, respectively. The measurement biases associated with these methods are usually small. However the considerable asphericity of the HRB-21 particles probably resulted in much larger than normal biases for both measurements. In both cases, a problem arises when the line segments on the image which are used to measure the coating thickness or particle radius are not parallel to the surface normal. Insufficient information is available to assess the errors in the GA measurements, but it is considered likely that the severe nonsphericity of many of the HRB-21 particles resulted in larger-than-normal errors. The error in the ORNL measurement is usually removed by comparing the diameter of the polished cross-section to the diameter at the midplane and applying a correction which assumes that the particles are essentially spherical. Because of the shape of the HRB-21 particles it was difficult to even determine the diameter of the midplane in many cases. In addition, for certain orientations of these heavily faceted particles, the assumption of sphericity used in the correction also breaks down. This problem would result in a fairly significant error in the kernel measurement. The error in the measurement of the outer coatings should be smaller because the size of the correction is inversely related to the distance from the center of the particle. Because it is anticipated that fuel particles fabricated under the AGR fuel program will have much better sphericity than the HRB-21 particles, this source of error in the ORNL HRB-21 particle measurements is not considered to be of concern.

Conversely, it is not surprising that there was a large difference in the PyC anisotropy results obtained by ORNL and GA because ORNL's 2-MGEM method used a dramatically different approach to measure the optical anisotropy as compared to the optical polarimeter technique that was used by GA (see Section 8 of ORNL report ORNL/CF-04/06, "Results From ORNL Characterization of German Reference Fuel From EUO 2358-2365 Composite"). However, it is interesting to note that the relative differences between the ORNL and GA BAFo values for the HRB-21 PyC were about the same as they were between the ORNL and GA BAFo values for the German EUO 2358-2365 particles. This suggests that the two techniques were measuring the same physical parameter and that the differences in the measured values were the result of a physical bias between the two measurement techniques.

7 TEM and X-ray Analysis of PyC Layer

N. Hashimoto, E.D. Specht and J.D. Hunn

Coating fragments were obtained as described in Section 1. A TEM specimen was prepared using focused ion beam micromachining (FIB). The FIB used a focused ion beam for controlled removal of material by sputtering. The FIB preparation involved sputter-coating the sample with Pt then depositing a thick protective layer of Pt using the FIB. Machining of the TEM specimen was then performed using 30 keV Ga^+ ions.

Figure 7-1 and Figure 7-2 show typical bright and dark field images of the PyC layer. 100-500 nm clumps were observed in the bright field image. Diffraction patterns from polycrystalline specimens can be viewed in much the same way as X-ray diffraction from powders. If the polycrystal is textured, there is usually one special plane nearly common to all the grains. The pattern produced by a random polycrystal can be distinguished from one produced by a textured specimen by a tilting technique. The diffraction patterns for this sample indicated a random polycrystal structure, in general. In the low magnification dark field images, the objective lens was used to select regions in the diffraction pattern that corresponded to a c-axis orientation either parallel (left image) or perpendicular (right image) to the growth direction (shown in the bright field image). Bright areas in the dark field image corresponded to pyrocarbon with a c-axis orientation close to the selected direction. One can see that the dark field images for the two orientations in Figure 7-1 and Figure 7-2 have inverted contrast with respect to each other. This type of imaging is currently being studied to look for microstructural evidence of crystallographic anisotropy in the layers.

Using the diffraction pattern, the grain size within the clumps could be estimated from the width of the rings, but it was more direct to observe the dark field image. Figure 7-3 shows a dark field image of the inner pyrocarbon layer. In the dark field image, diffracted spots selected by the objective lens aperture made white contrast on the image. From these spots, the size distribution of grains and average grain size could be estimated to be 1.1±0.3 nm. Figure 7-4 shows a dark field image of the outer pyrocarbon layer. The estimated grain size was 1.0±0.2 nm. Figure 7-5 shows the distribution in grain size as measured by this technique. Grain size was similar to that measured for the German reference material.

Figure 7-6 shows typical high resolution images (lattice images) of IPyC and OPyC. The high resolution electron micrographs shows the carbon layer planes in a clump. The micrographs seem to show the uniform arrangement of the crystallites in each sample. However, careful TEM analysis revealed that layers were wavy and apparently form a grain with 3~5 layers. Figure 7-7 shows a comparison between a lattice image and a dark field image of OPyC. The lattice image indicates a layer separation of 0.35 nm, corresponding to c_o-axis/2 of pyrolytic carbon. From these TEM results, a structure model (tentative) for the particle of pyrocarbon could be suggested (Figure 7-8).

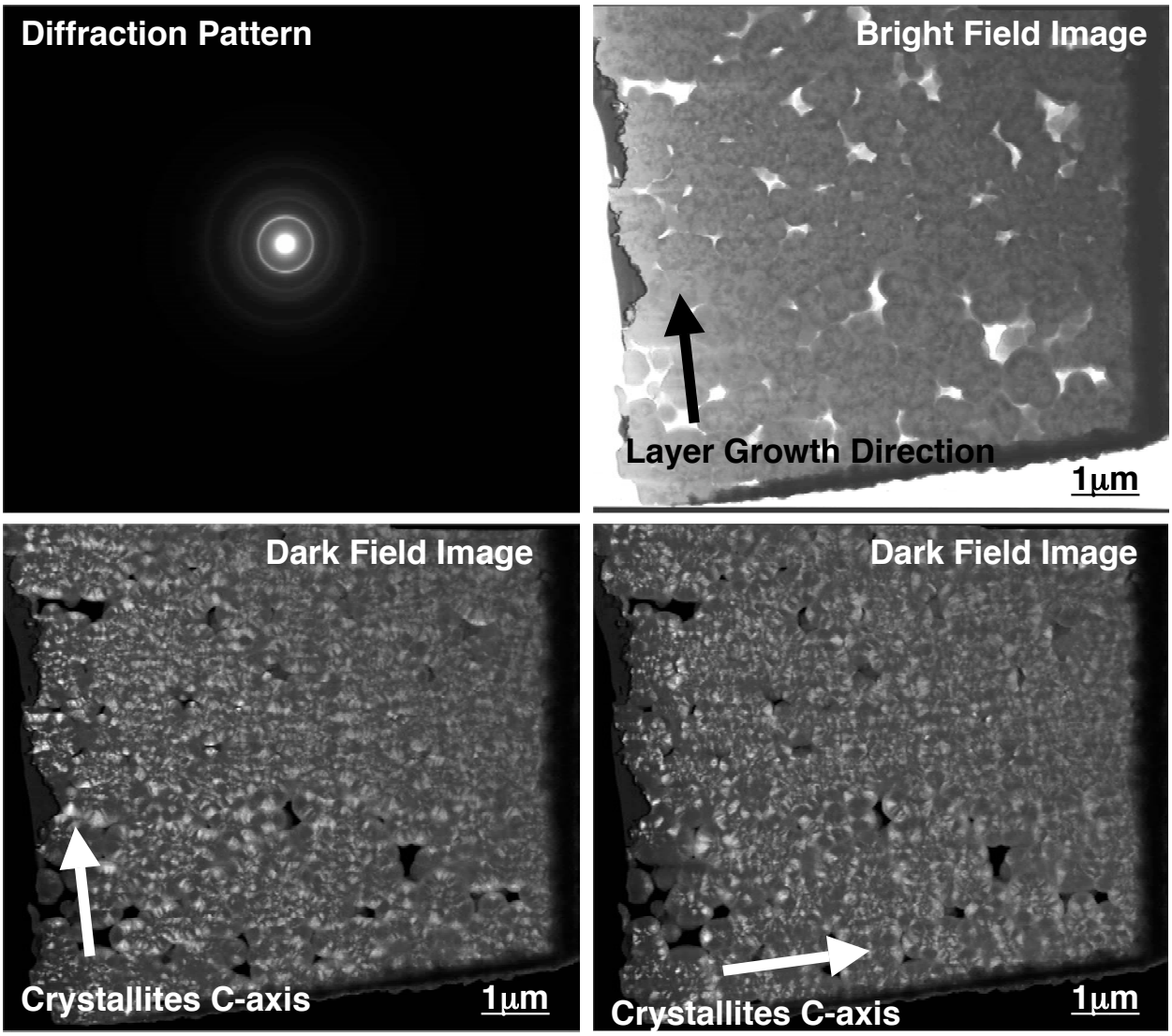

Figure 7-1: IPyC Low Magnification TEM image.

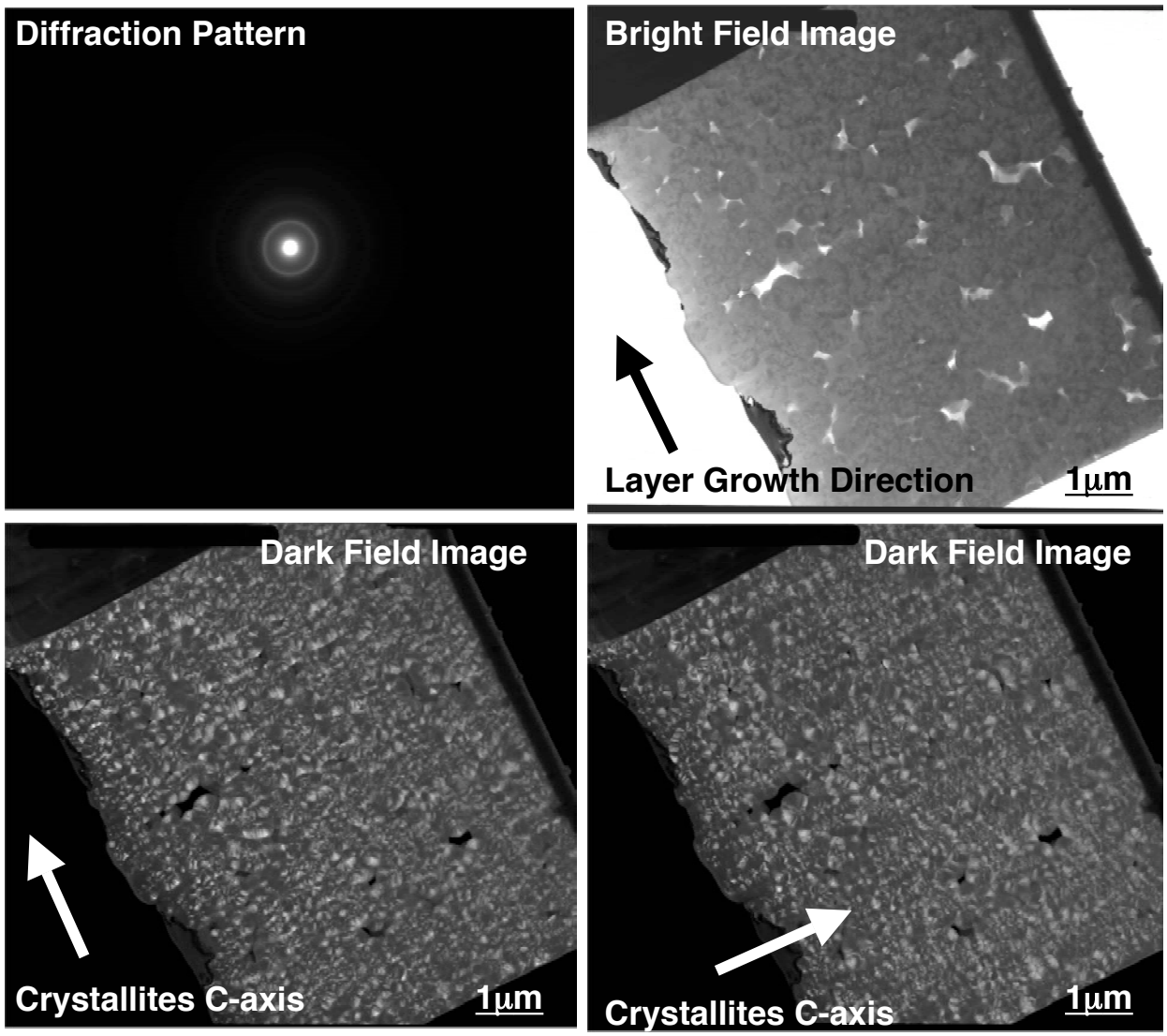

Figure 7-2: OPyC Low Magnification TEM image.

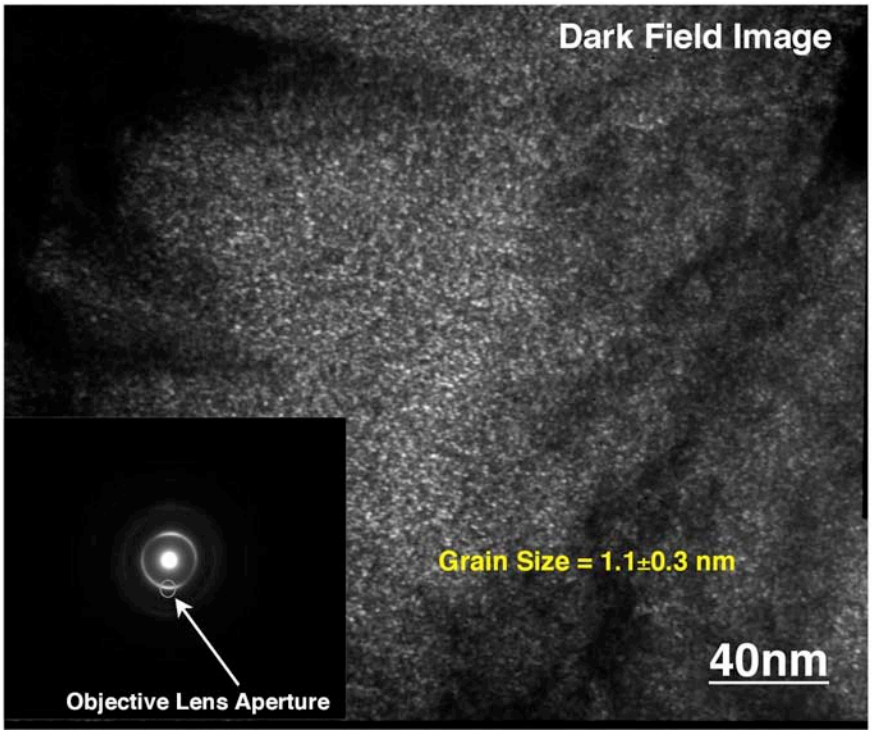

Figure 7-3: IPyC dark field image.

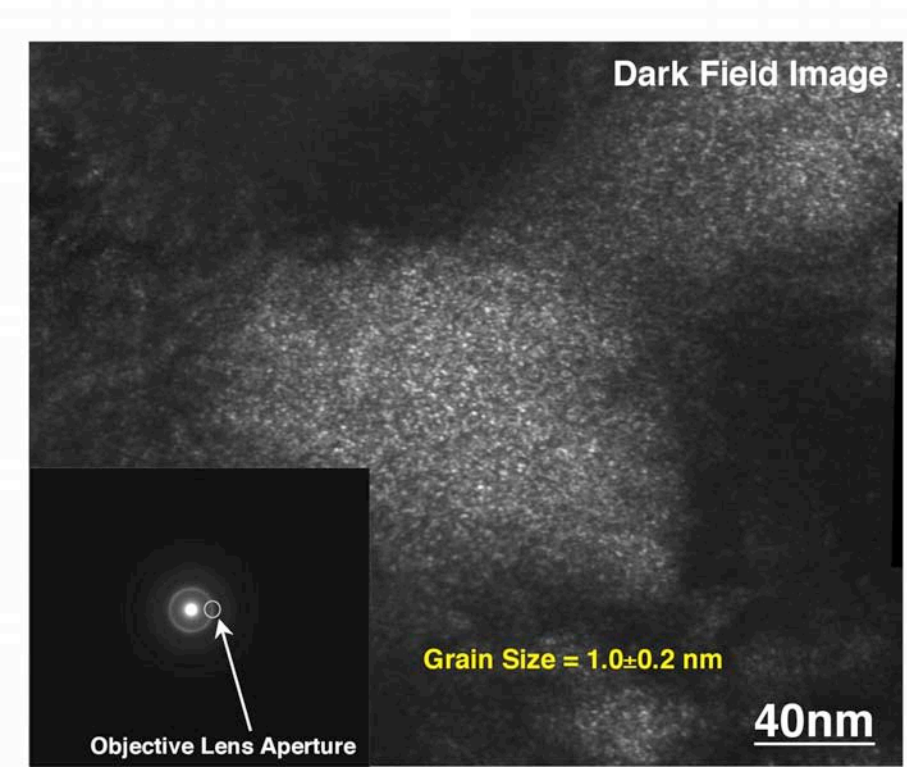

Figure 7-4: OPyC dark field image.

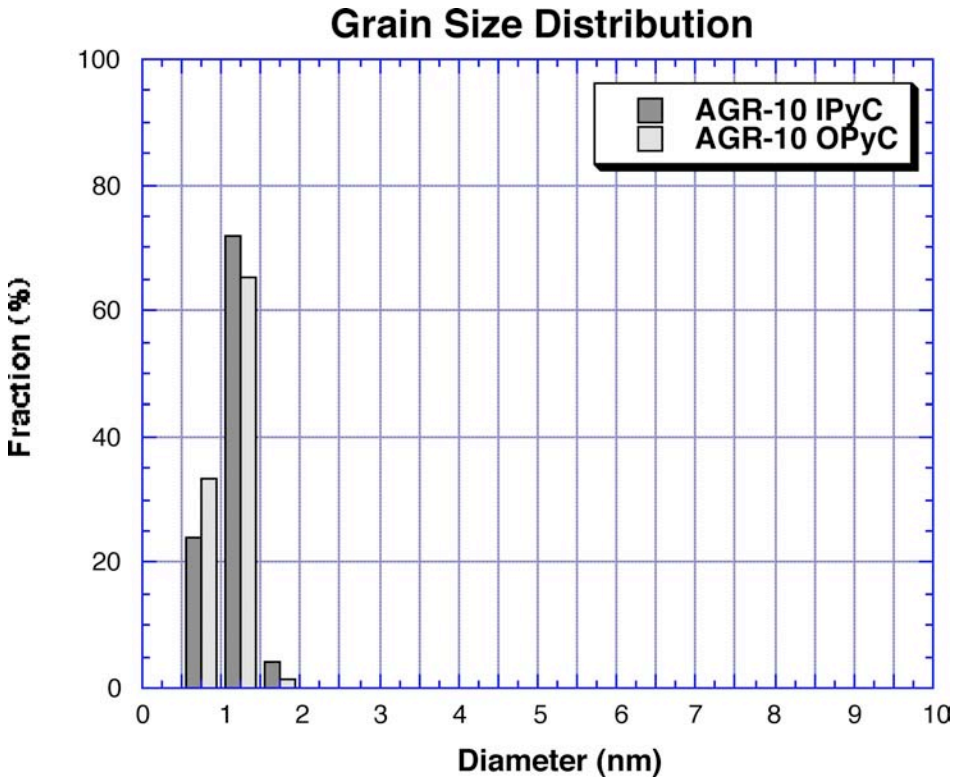

Figure 7-5: Grain sizes in PyC layer measured by TEM.

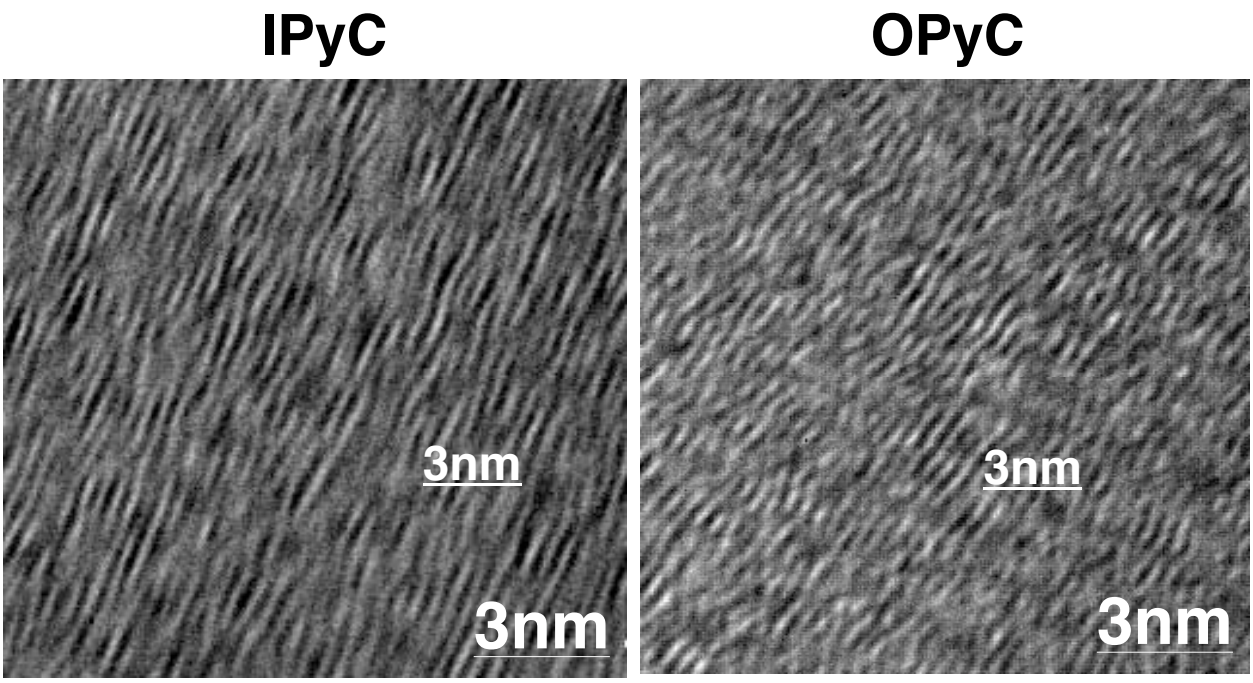

Figure 7-6: Lattice images of IPyC and OPyC.

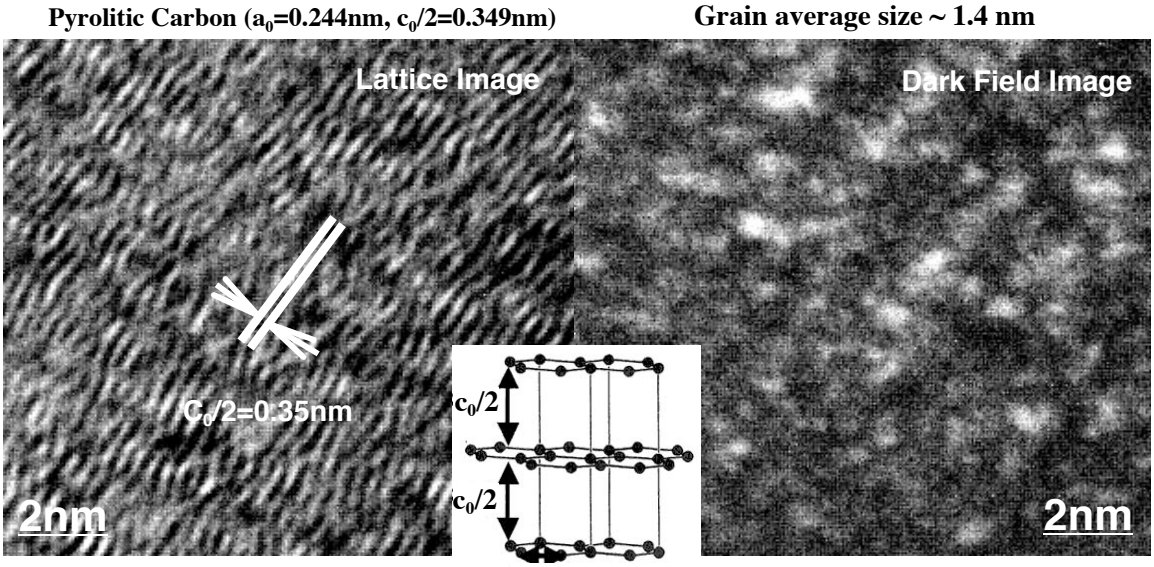

Figure 7-7: Comparison between a lattice image and a dark field image of OPyC.

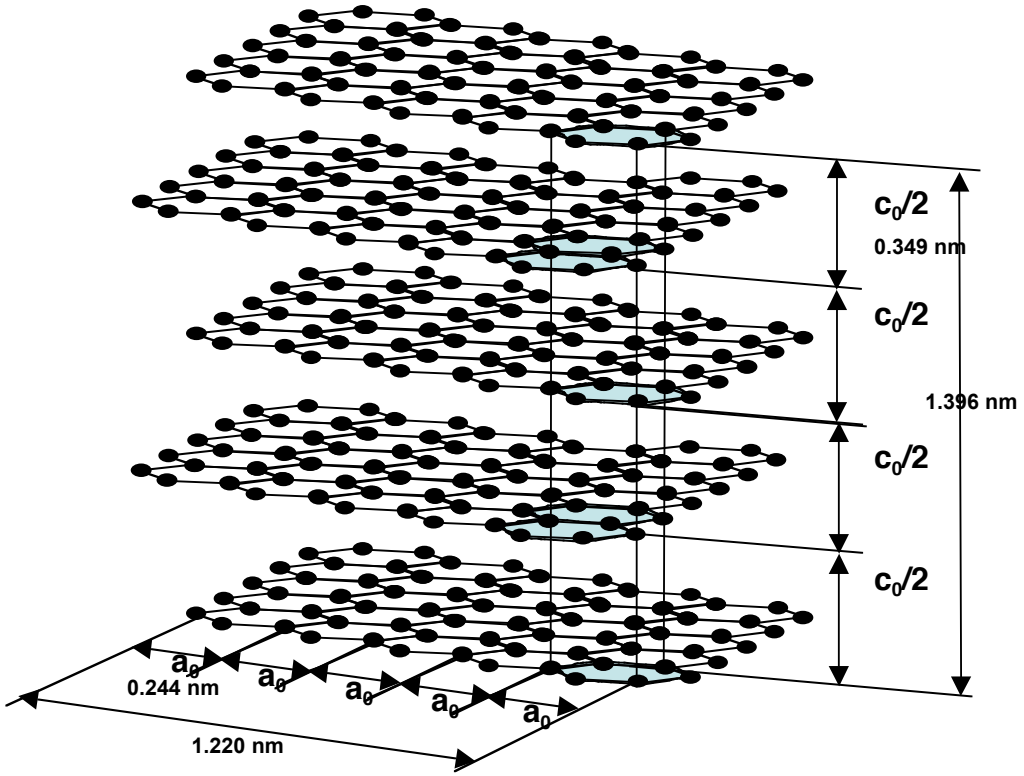

Figure 7-8: Structure model for the crystallite of pyrocarbon.

X-ray diffraction was performed on a coating fragment of IPyC/SiC. Figure 7-9 shows the diffraction pattern obtained. Cubic SiC was visible with instrumentally sharp reflections indicating a SiC particle size of >100 nm. The carbon was turbostratic, meaning the particles were not true crystallites, but stacks of graphitic atomic layers with their *c* axes aligned but with *a* axes in random directions. As a result, only (*hk*0) and (00*l*) reflections occurred, and the (*hk*0) reflections had a characteristic asymmetric lineshape. Parameters for the C(002) and C(100) peaks were found by least-squares fitting to Pearson-7 lineshapes:

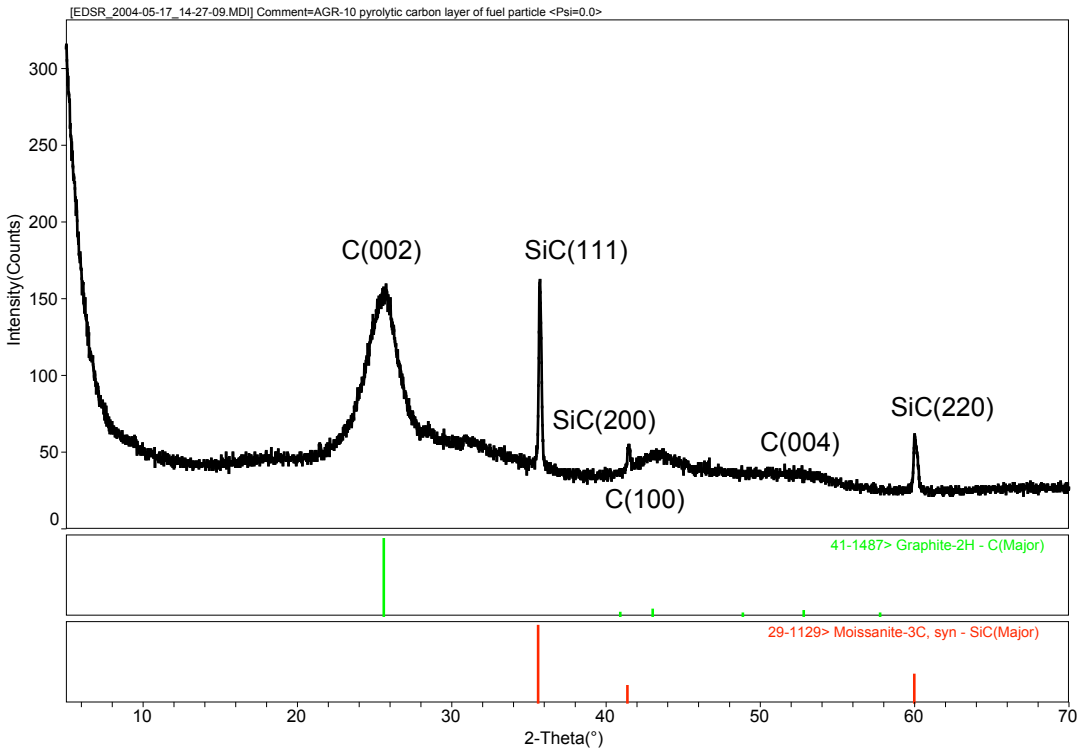

Figure 7-9: Diffraction pattern from fragment of IPyC/SiC.

Table 7-1: Carbon peaks observed for IPyC.

	C(002)	C(100)
2θ (deg.)	25.47	43.30
FWHM (deg)	2.37	3.70

The analysis followed that of J. Biscoe and B.E. Warren ["An x-ray study of carbon black", *Journal of Applied Physics*, **13**, 364-371 (1942)]. The particle size in the plane of the graphitic layers was calculated to be

$$L_a = \frac{1.84\lambda}{\mathrm{FWHM}_{100}\cos\theta_{100}} = 4.7 \text{ nm},$$

where $\lambda = 0.15406$ nm was the x-ray wavelength. The particle size in the normal direction was calculated to be

$$L_c = \frac{0.89\lambda}{\mathrm{FWHM}_{002}\cos\theta_{002}} = 3.4 \text{ nm}.$$

The particles were disk-shaped. These values are larger than the grain size as measured by TEM. This discrepancy is currently being evaluated.

Lattice parameters were calculated to be

$$a = \frac{2}{\sqrt{3}}\frac{\lambda}{2(\sin\theta_{100} - \Delta)} = 0.244 \text{ nm}$$

$$c = \frac{2\lambda}{2\sin\theta_{002}} = 0.699 \text{ nm},$$

where $\Delta = \frac{0.16\lambda}{L_a}$. Note that the *c* lattice parameter was significantly longer than that of graphite (*c*=0.670 nm), another indication of a turbostratic structure.

8 SEM Analysis

P.A. Menchhofer, J.D. Hunn, and W.E. Comings

8.1 SEM of kernels

24 HRB-21 particles were mounted and cross sectioned for SEM analysis. Figure 8-1 and Figure 8-2 show a UCO kernel in cross-section. Using high contrast in backscattered electron mode, the grain structure of the kernel could be imaged. The grains around the outer surface of the kernel were much larger than those observed in the central region. Energy dispersive x-ray spectroscopy (EDS) showed that the large outer grains were all uranium oxide. The interior of the kernel was a mixture of uranium oxide and uranium carbide grains. Figure 8-2 and Figure 8-3 show numerous short thin lines of higher brightness in the interior of the kernel, often at the edges of grains but sometimes cutting across a grain. The EDS spectra for these regions suggest that they are UC, in contrast to the other carbide grains which appear to be UC_2. This is discussed further in section 9.

The kernels shown in Figure 8-1 through Figure 8-3 do not represent the average kernel observed after cross-sectioning the particles. Most of the kernels showed extensive porosity such as can be seen in Figure 8-4. Figure 8-5 shows optical images of several kernels with various levels of porosity. In this image, the UO_2 areas appear gray, the carbide areas appear white, and the pits appear black. The kernel in the top left does not show much porosity and exhibits the same kind of microstructure as seen in Figure 8-1, with a central region of mixed oxides and carbides surrounded by a rind of oxide at the surface. It is interesting to note that the pores in the other kernels in Figure 8-5 are also surrounded by this oxide rind. This suggests that these pores were open to the surface of the kernel during processing. One important effect of the open porosity in the UCO kernel appears to be a drastic reduction in the carbide content. The cross-section in Figure 8-4 show no carbide at all.

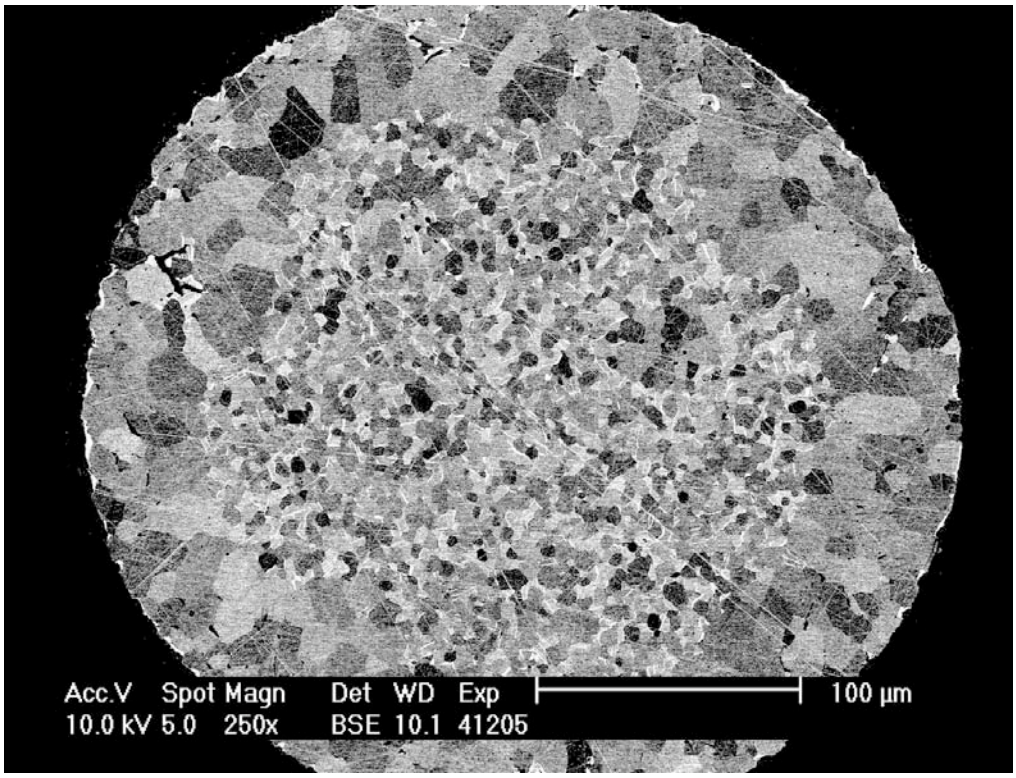

Figure 8-1: HRB-21 kernel cross section.

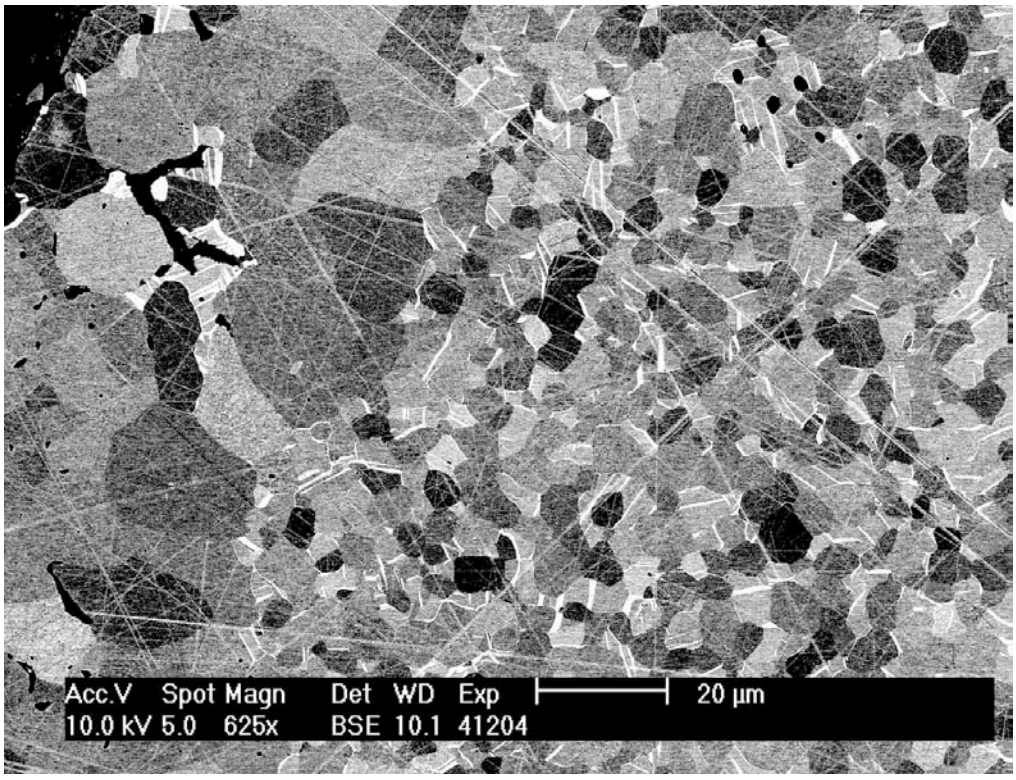

Figure 8-2: HRB-21 kernel cross section.

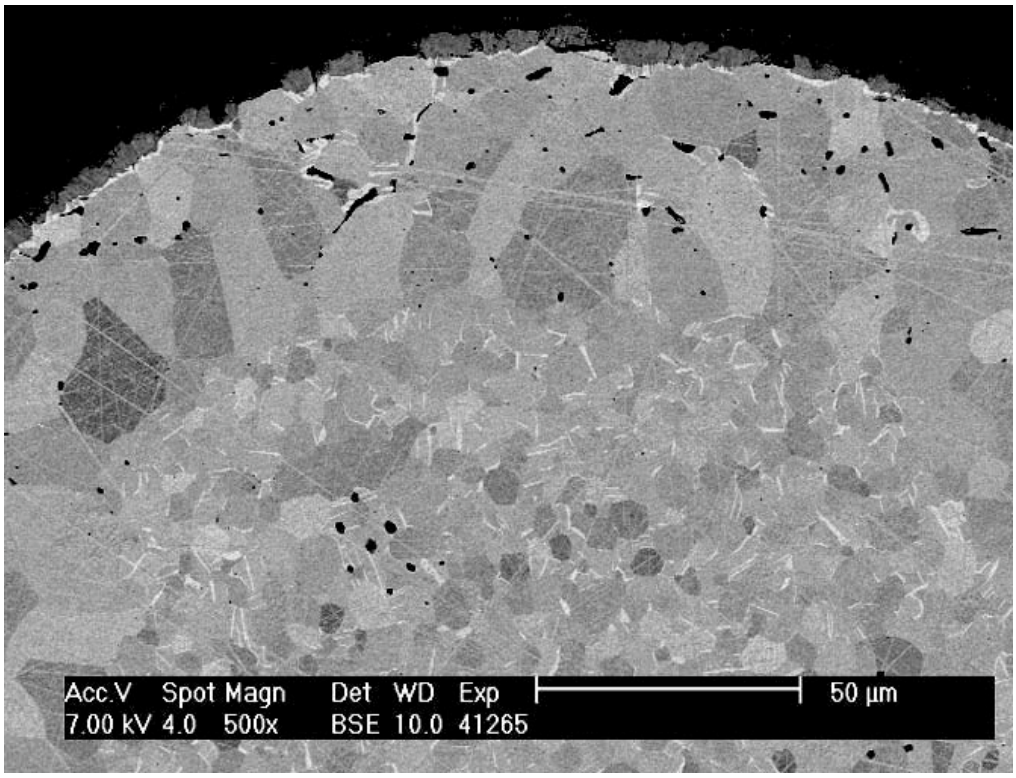

Figure 8-3: HRB-21 kernel cross section.

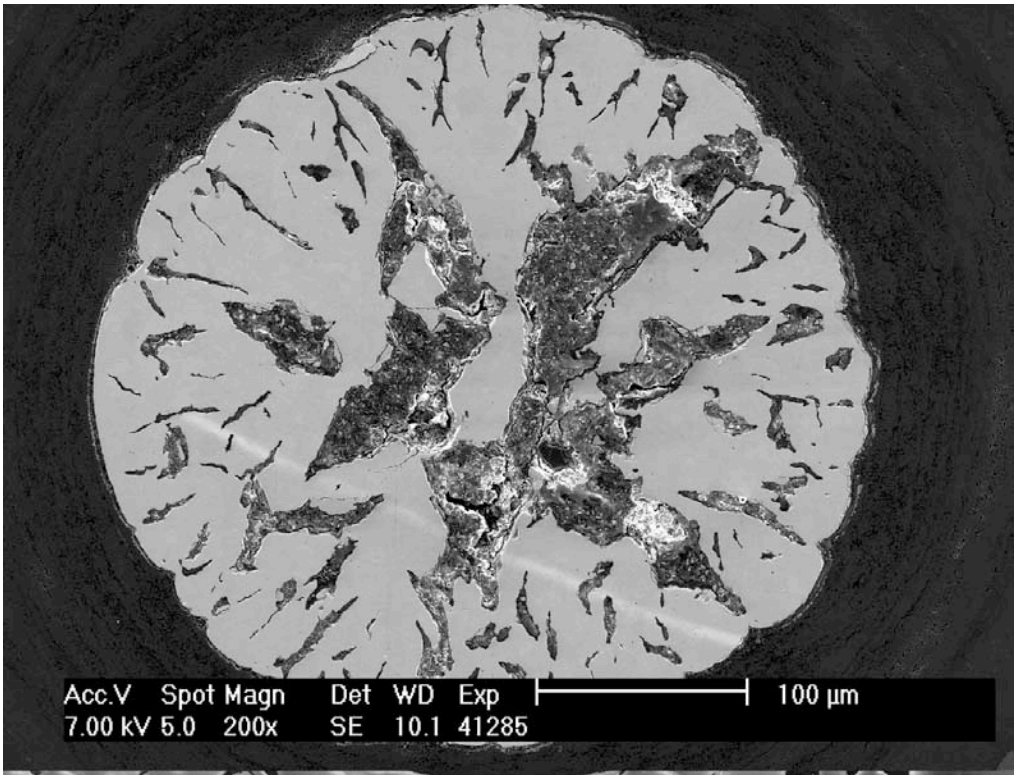

Figure 8-4: HRB-21 kernel showing extensive porosity.

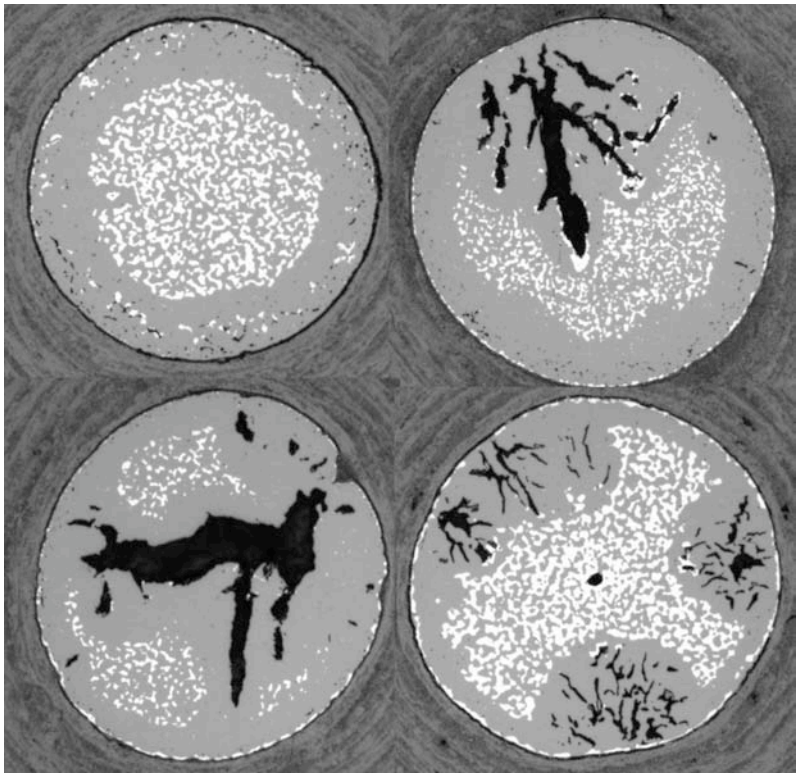

Figure 8-5: Optical image of several kernels with various porosity.

8.2 SEM of coated particles

Figure 8-6 shows a typical particle cross-section with a bright kernel surrounded by a porous buffer surrounded by a dark gray IPyC layer, a bright SiC layer, and a dark gray OPyC layer. A thin seal coat was also visible between the buffer and the IPyC. This was more obvious in Figure 8-8. The seal coat had well defined boundaries as opposed to the transition layer observed in the German coatings (Figure 8-9). Note the crack just inside the buffer at the buffer/seal coat interface in Figure 8-8. This cracking was common in these coatings and probably accounts for the fracture observed in section 1, Figure 1-5 and Figure 1-6, where separation tended to occur between the buffer and seal coat.

The buffer layer in the HRB-21 particles (Figure 8-6) appeared to be more porous than in the German particles (Figure 8-7). The buffer layers were made up of clumps of material. The clumps were presumably formed in free space and deposited onto the surface of the particle during coating. These growth features were smaller in the HRB-21 buffer than they were in the German buffer.

The HRB-21 IPyC (Figure 8-10) and OPyC (Figure 8-11) layers had a similar appearance. There was some evidence (Figure 8-6) of banding in the pyrocarbon layers (produced by alternating sub-layers of high porosity and low porosity), but it was not as evident as it was in the German coated particles (Figure 8-7). The porosity in the HRB-21 pyrocarbon layers appeared to be more randomly distributed. A layered structure of high and low density pyrocarbon, as observed in the German fuel, may result in a layer that is less permeable than one that has the same average envelope density but is more uniform throughout the thickness.

The interface between the IPyC and the SiC is shown in Figure 8-12. There were no gaps in the interface and the SiC intruded into the open pores of the IPyC. According to John Saurwein at GA, post mortem tests on HRB-21 concluded that the IPyC/SiC layers were not sufficiently bonded. The IPyC/SiC interface is shown at higher magnification for the HRB-21 fuel in Figure 8-13 and the German fuel in Figure 8-14. This has not yet been studied thoroughly for a large number of particles, but in these images there were some differences in the interface. The interfacial stitching in the German particle was somewhat more extensive in these higher magnification images. However, these images only show a limited region. Images at lower magnification such as Figure 8-12 showed a reasonable degree of interlacing occurred at the interface. Perhaps of greater importance is the fact that the HRB-21 fuel showed significantly more porosity near the interface. This additional porosity would result in a weaker interface regardless of the SiC stitching at the boundary. The high/low density layered structure observed in the German fuel presented an IPyC surface with a shallow layer of open porosity sufficient to allow for SiC penetration immediately adjacent to a denser pyrocarbon.

The interface between the OPyC and the SiC is shown in Figure 8-15 for a HRB-21 particle. The interface was dramatically different from the German interface shown in Figure 8-16. The OPyC was completely broken away from the SiC. This was most likely not an artifact of the sample preparation and was observed on most of the samples. This delamination at the SiC/OPyC interface explains why the OPyC layers were observed to easily separate from the SiC during fracture.

Figure 8-17 and Figure 8-18 show the SiC layer in high contrast. The grain structure can be seen in these high contrast images due to variations in electron channeling with respect to SiC crystal orientation. Most of the grains were a few microns in size in the exposed plane, but there were a few elongated (columnar) grains with the long axis oriented in the growth direction. Methods for better imaging of the SiC grain structure are currently being investigated.

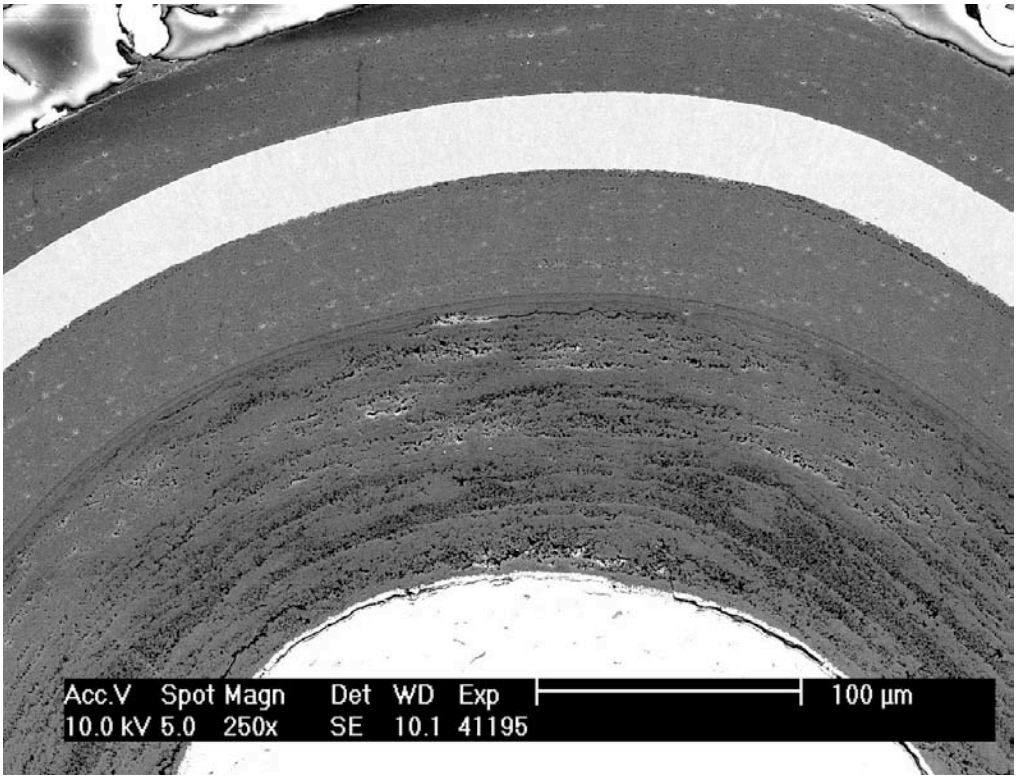

Figure 8-6: Typical coating layers for HRB-21.

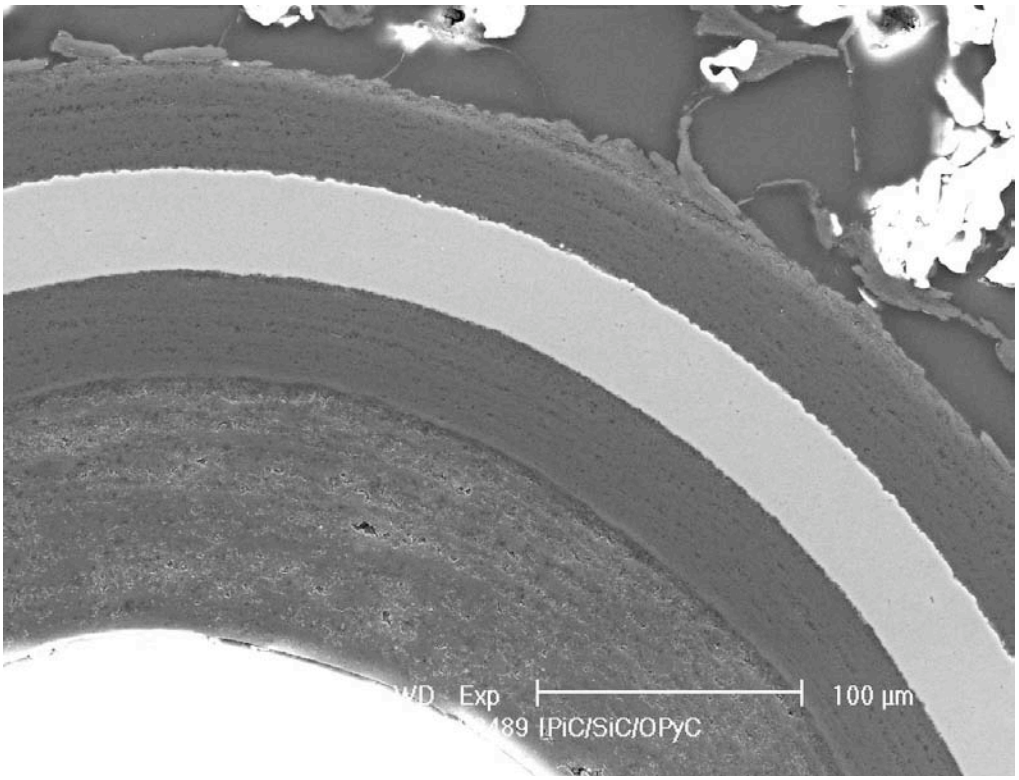

Figure 8-7: Typical coating layers for German particles.

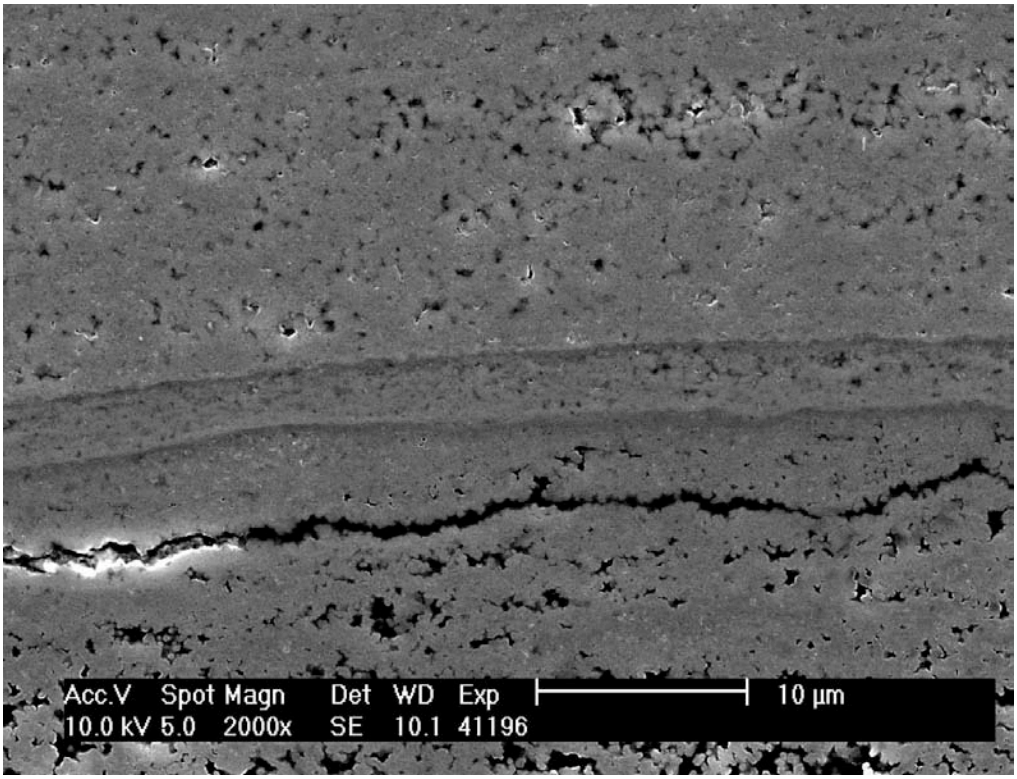

Figure 8-8: Buffer/IPyC interface showing buffer seal coat in HRB-21 coating.

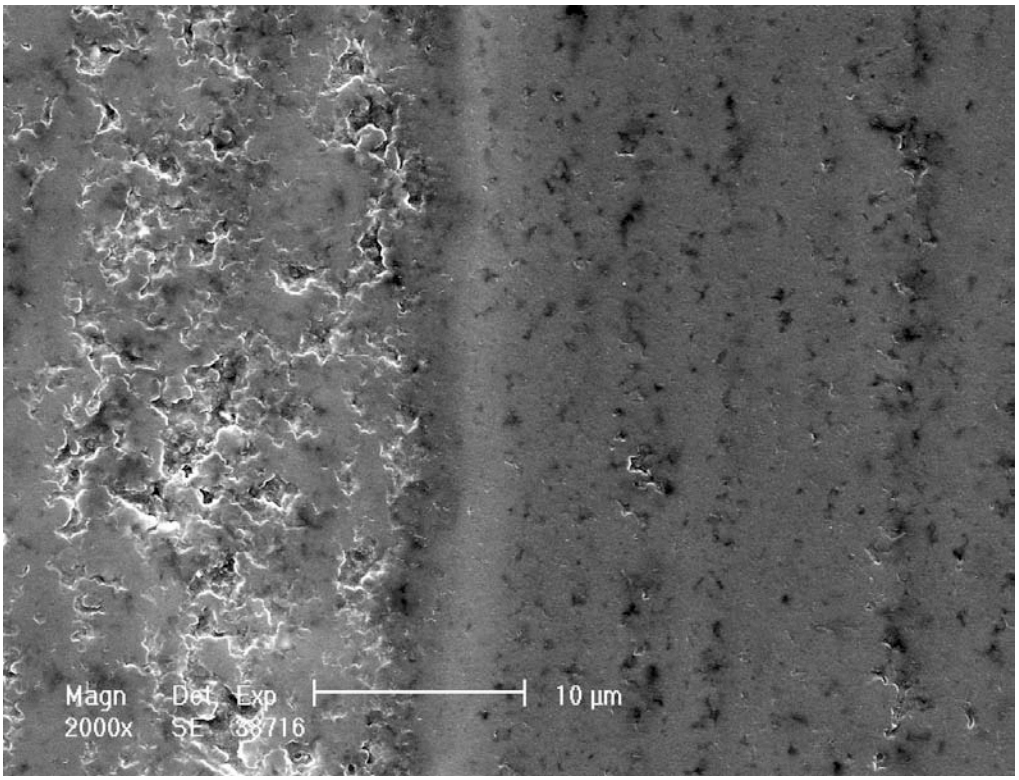

Figure 8-9: Transition layer between buffer and IPyC in German coating.

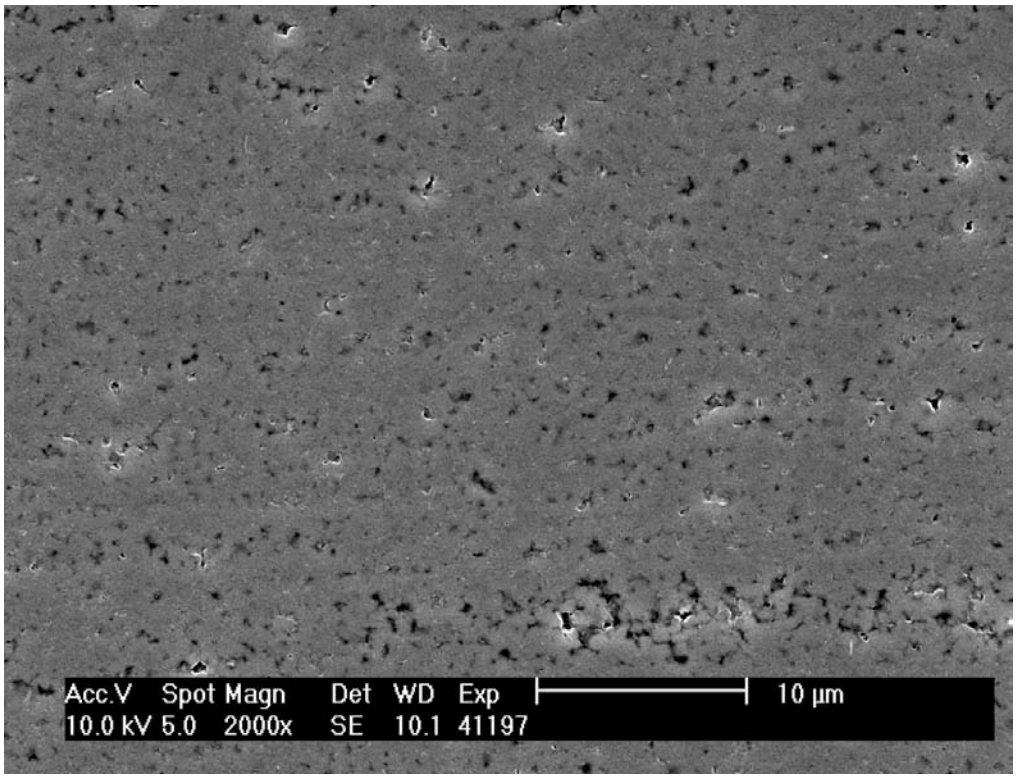

Figure 8-10: HRB-21 IPyC.

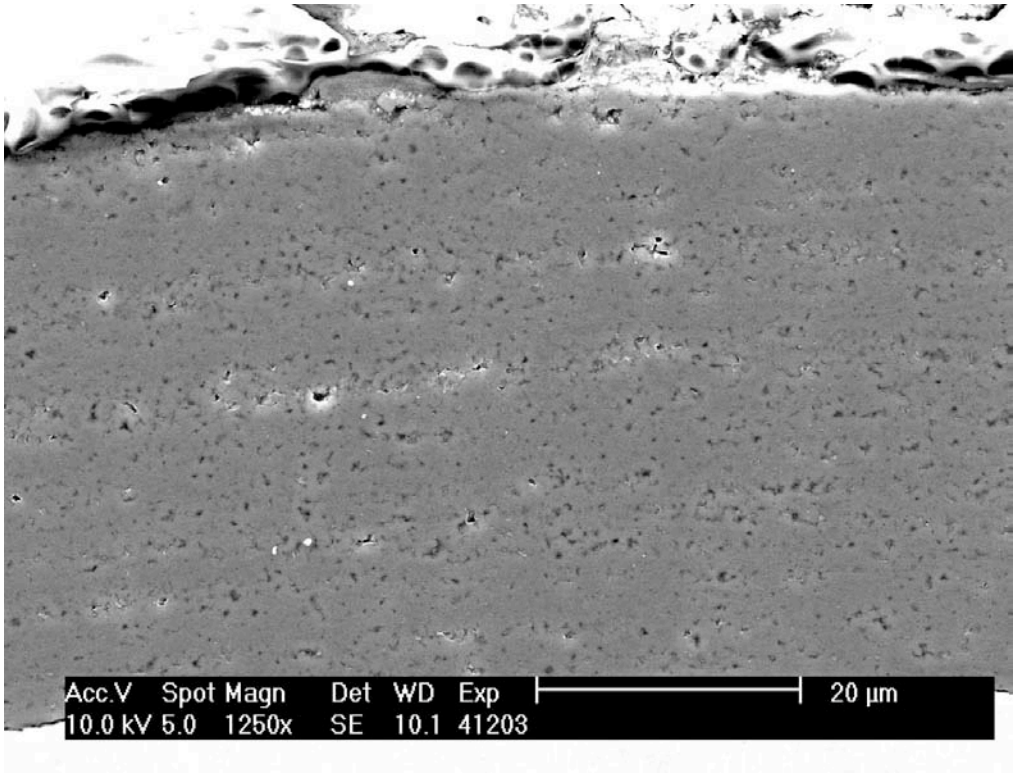

Figure 8-11: HRB-21 OPyC.

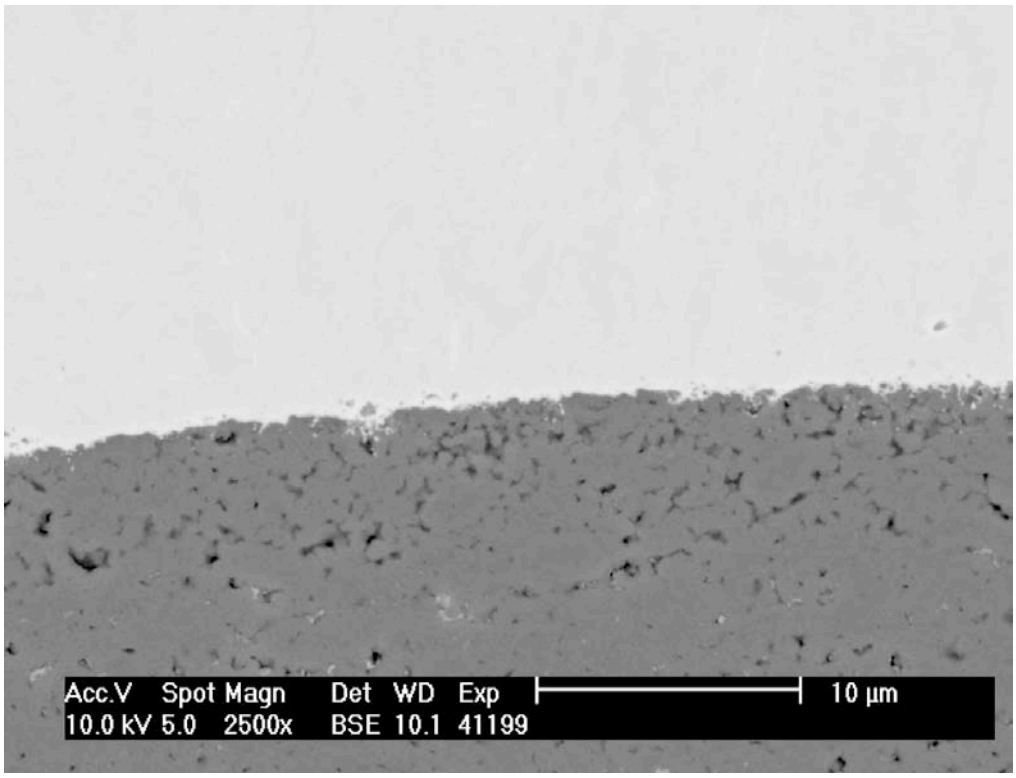

Figure 8-12: HRB-21 IPyC/SiC interface (bottom to top).

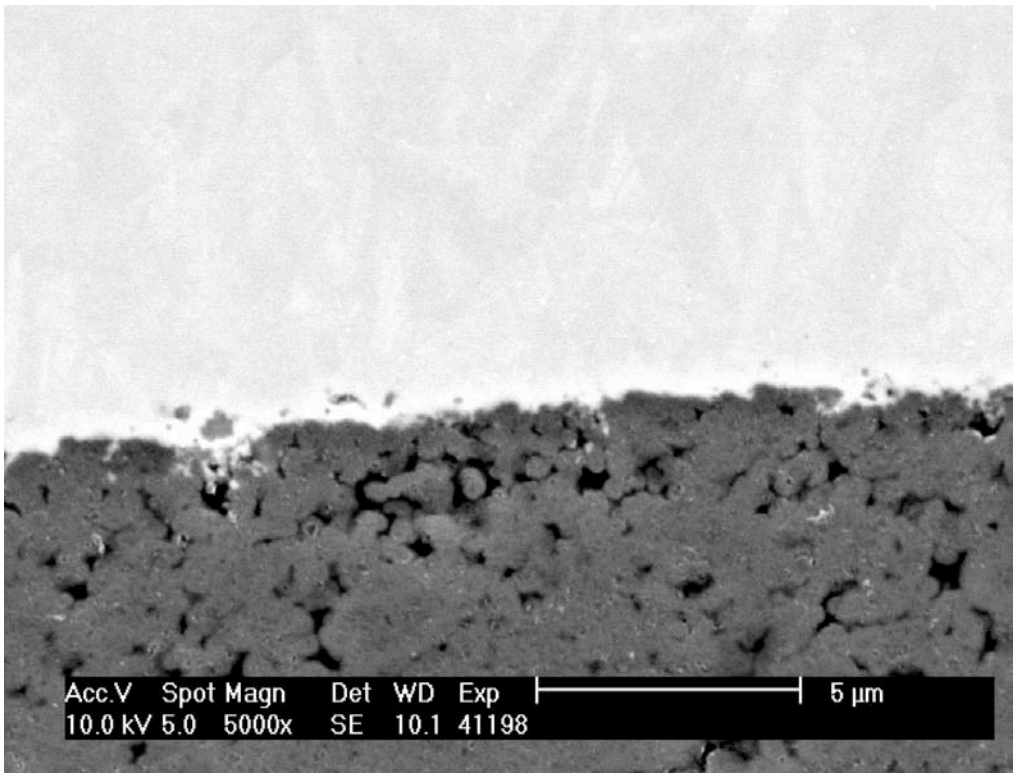

Figure 8-13: HRB-21 IPyC/SiC interface.

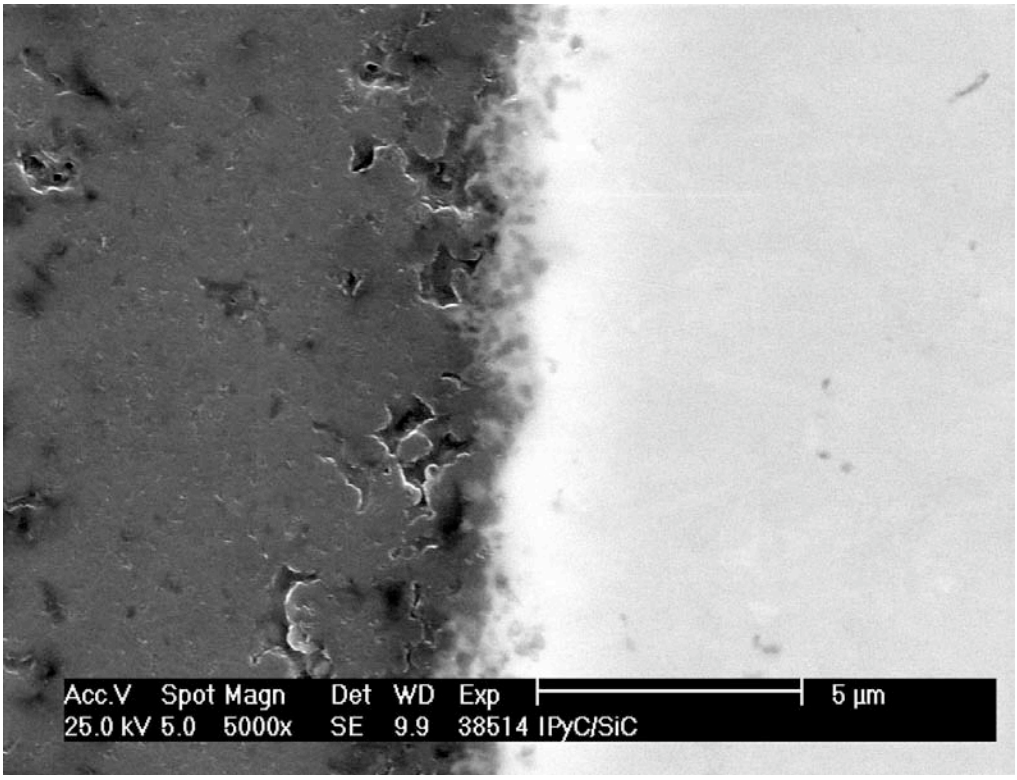

Figure 8-14: German IPyC/SiC interface.

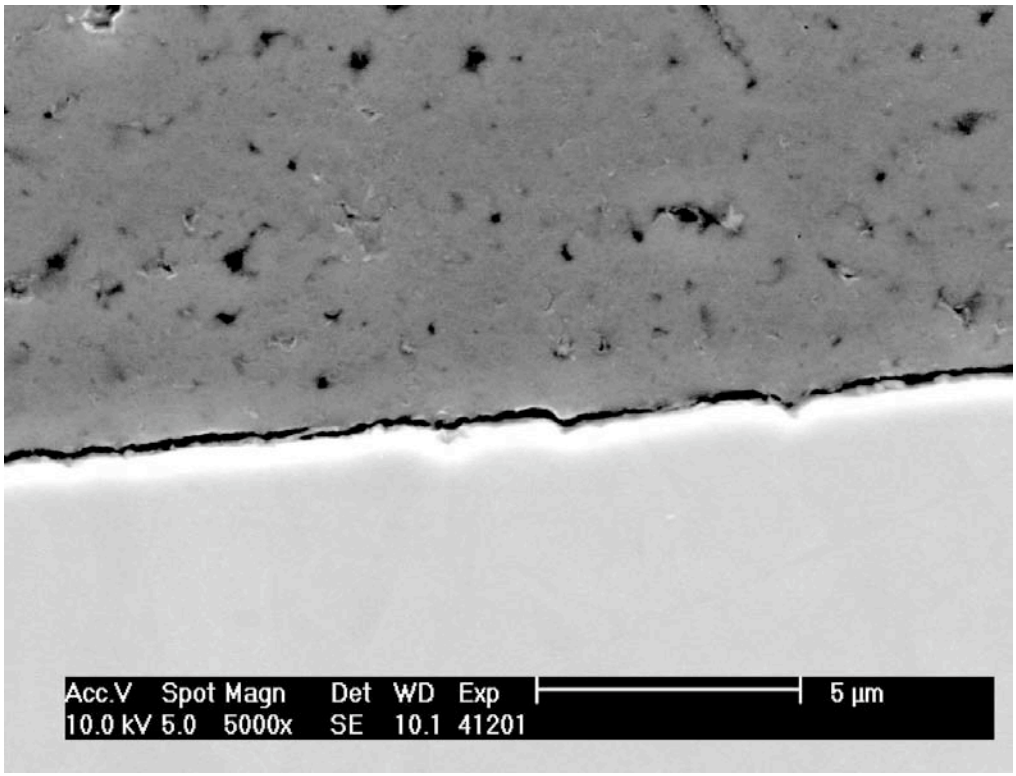

Figure 8-15: HRB-21 SiC/OPyC interface (bottom to top).

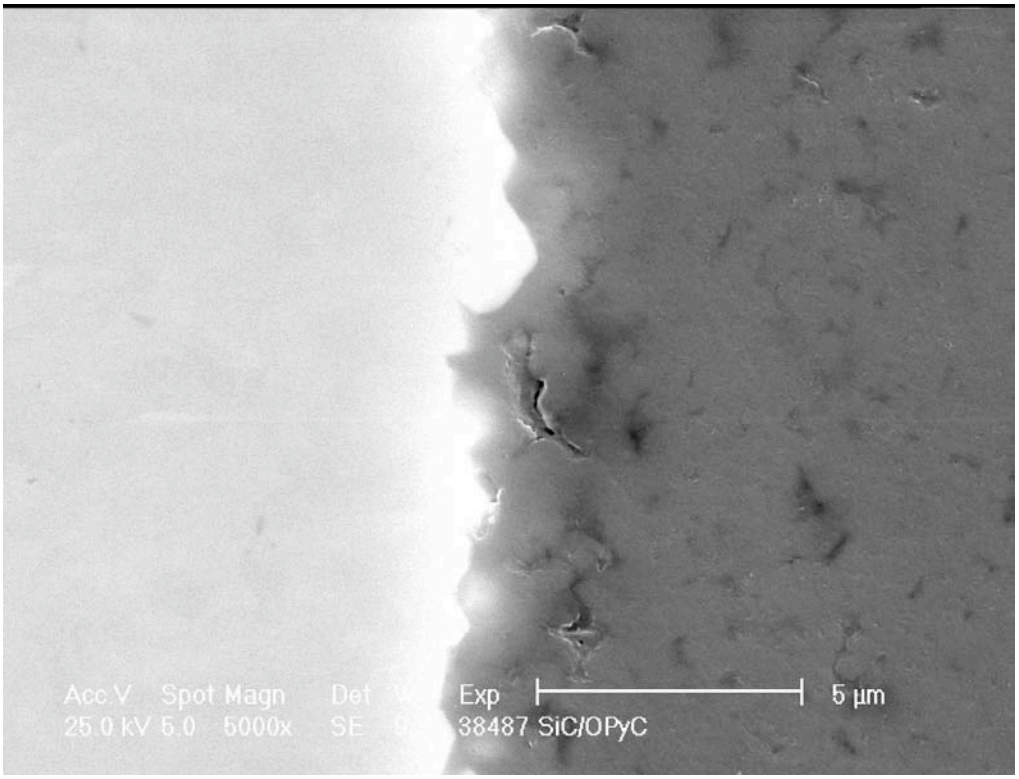

Figure 8-16: German SiC/OPyC interface.

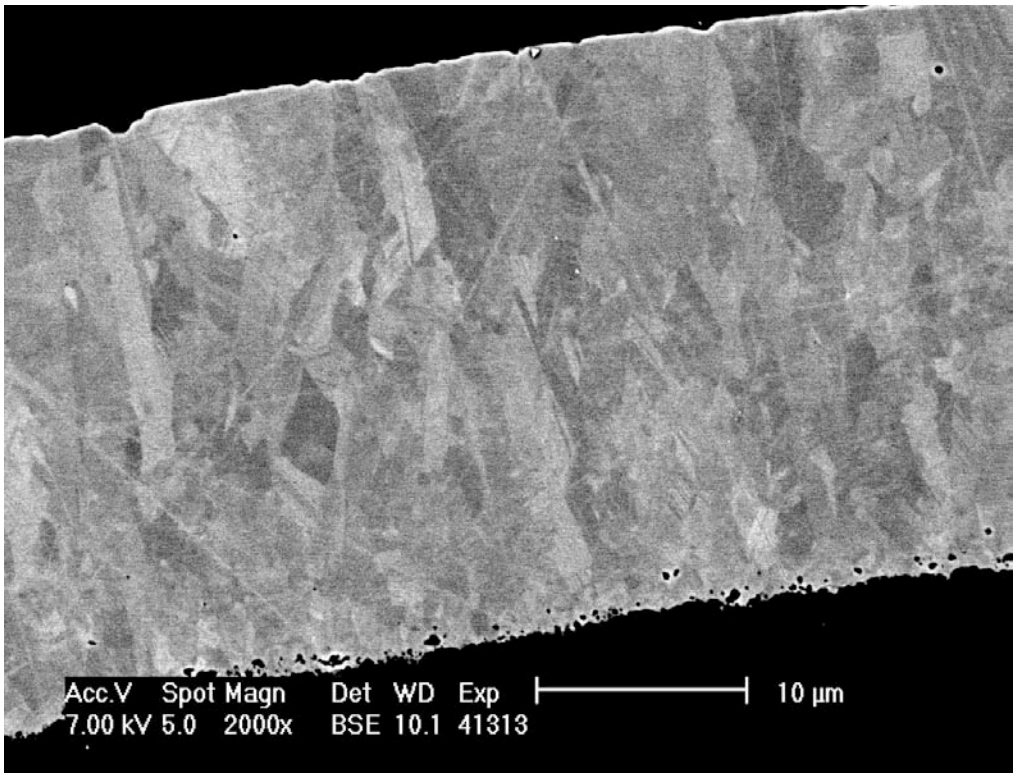

Figure 8-17: HRB-21 SiC at high contrast in backscattered electron mode.

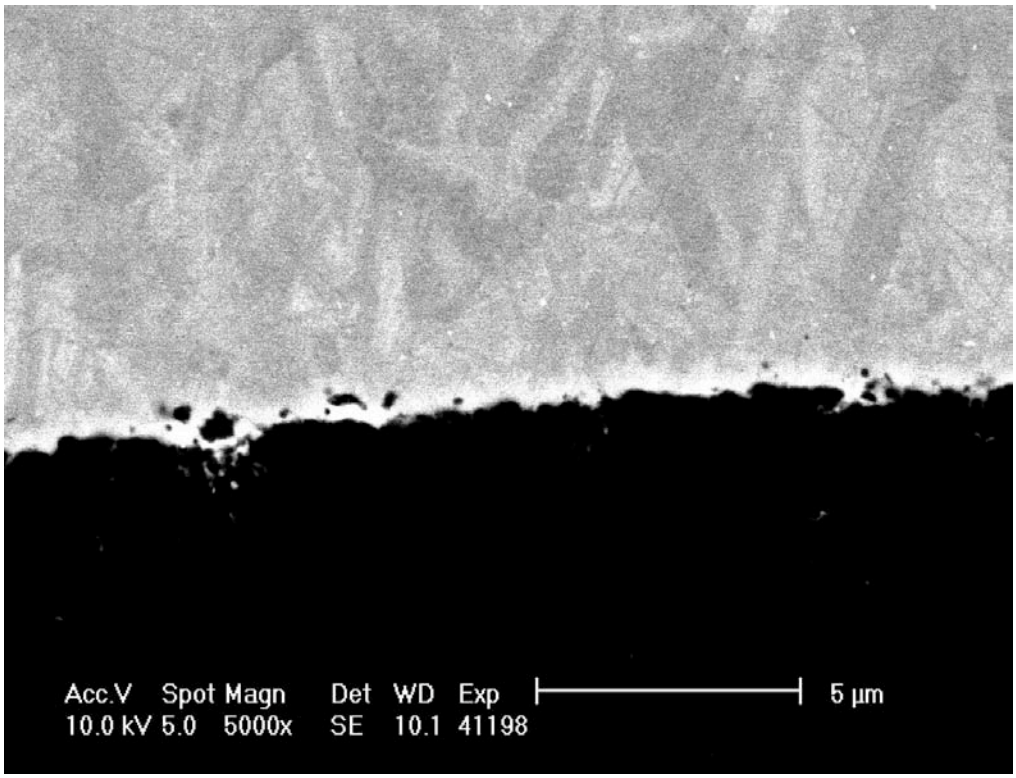

Figure 8-18: HRB-21 SiC at high contrast in scanning electron mode.

9 EDS Mapping

J.D. Hunn, P.A. Menchhofer, and E.A. Kenik

In order to analyze the cause of the observed contrast variation in the optical and SEM imaged kernel cross sections, energy dispersive x-ray spectroscopy (EDS) was performed. Figure 9-1 shows a backscattered electron image of a HRB-21 kernel cross section. Brighter areas indicate more backscattered electrons were detected. In this case brighter areas indicate a higher concentration of uranium or a lower degree of channeling. The area in the white box in Figure 9-1 was scanned using EDS to produce elemental maps of uranium, carbon, and oxygen. For this technique, the sample was rastered in 0.2 μm steps over the analysis region. At each point an EDS spectrum was obtained. The relative elemental concentrations at each point in the scanned area were then extracted from the thousands of spectra to form the elemental maps shown in Figure 9-2. Brighter areas in the elemental maps indicate a higher relative concentration of that particular element.

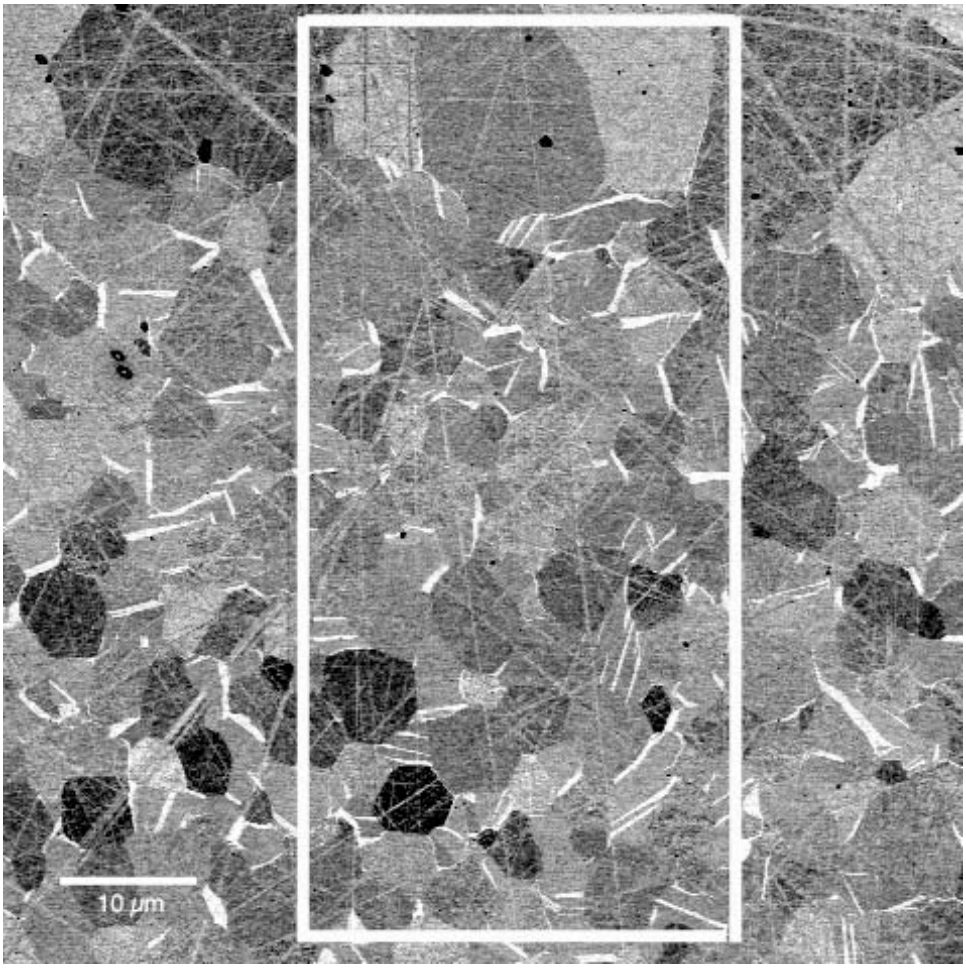

Figure 9-1: Backscatter electron image of HRB-21 kernel

In Figure 9-2 the C map and the O map are essentially inversely related. This indicates that the oxide and carbide phases are segregated. Oxide regions are dark in the C map and bright in the O map. Carbide regions are bright in the C map and dark in the O map. The dark spots near the top of the U map are pits. These show up as dark spots in the O map and bright spots in the C map. There is probably carbon residue from the polishing in these pits. In the C map, the carbide phases (bright regions) have some lighter gray streaks running through them. These streaks are brighter in the U map and in the backscattered electron image. These streaks are probably UC regions with the larger carbide regions being UC_2. The UC would show less yield in the C map because of the lower carbon content. The UC would be brighter in the U map and in the backscattered image because the density of UC (13.63 g/cc) is higher than the density of UC_2 (11.28 g/cc). The oxide regions are the darkest in the U map because the density of UO_2 is the lowest (10.96 g/cc).

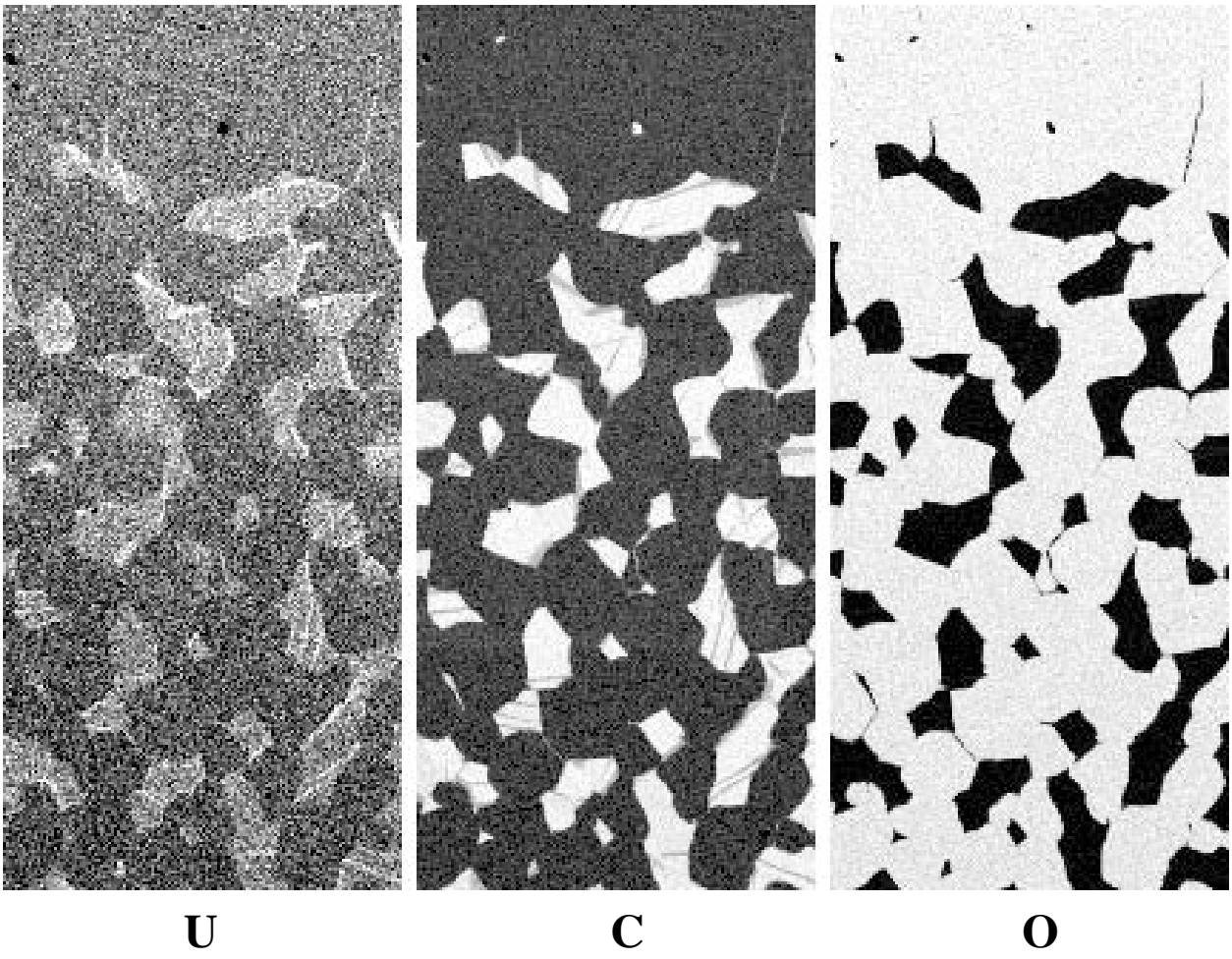

Figure 9-2: Elemental maps of NUCO produced by EDS.

10 Appendix A: 2-MGEM Data Report

File Name: C:\EllipDat\04_2728_04R\NFM040318a5 Date: 5/13/2004
Description: Highly anisotropic IPyC layer? Time: 3:47:29 PM
Data Normalized

Diattenuation (-0.010 to 0.030) Zero Color:

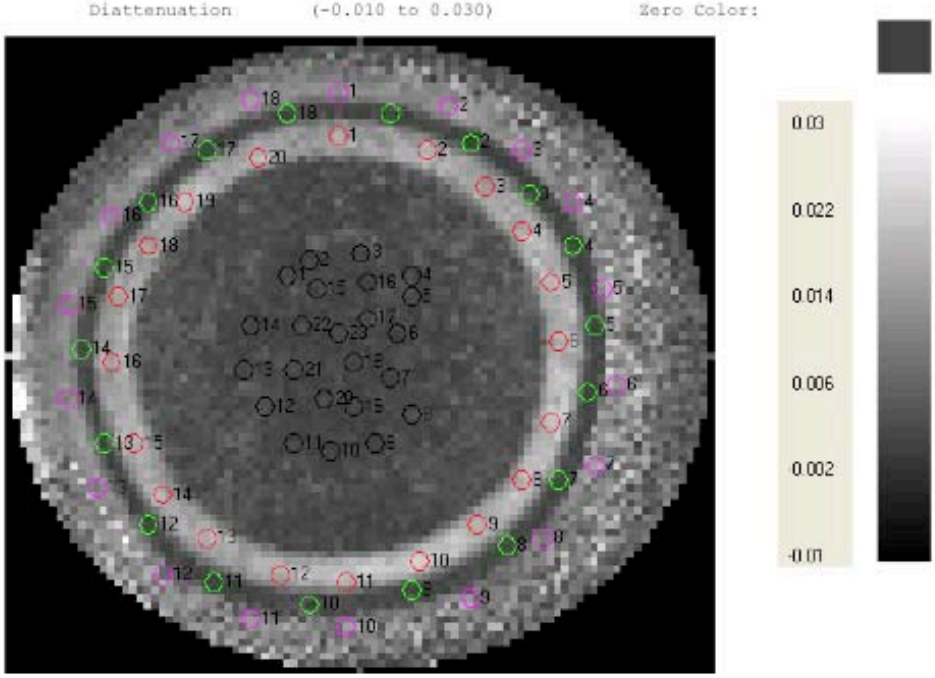

Selected Data

#	Pixel i	Pixel j	Position X	Position Y	Diattenuation (N)	Retardation (rad)	Fast Axis Angle (°)	Circular Diattn	Polar. Factor	Intensity (Arb. Units)
Saved list A--(20)										
1	46	74	0.45	0.73	0.0183±0.0045	-0.0072±0.0047	-87.0±5.3	0.0001±0.0030	1.0190	2.0262
2	58	72	0.57	0.71	0.0179±0.0035	-0.0065±0.0052	-66.5±5.7	-0.0015±0.0025	1.0017	2.0714
3	66	67	0.65	0.66	0.0146±0.0031	-0.0039±0.0046	-49.1±6.3	-0.0001±0.0021	0.9944	2.3488
4	71	61	0.70	0.60	0.0176±0.0038	-0.0003±0.0054	-30.4±6.3	-0.0004±0.0019	1.0150	2.4856
5	75	54	0.74	0.53	0.0187±0.0030	0.0039±0.0044	-16.2±5.1	0.0008±0.0040	0.9952	2.6882
6	76	46	0.75	0.45	0.0165±0.0027	-0.0046±0.0040	2.8±5.0	0.0005±0.0031	0.9995	3.0692
7	75	35	0.74	0.34	0.0208±0.0031	-0.0016±0.0039	20.6±4.2	-0.0009±0.0021	1.0097	3.9960
8	71	27	0.70	0.26	0.0167±0.0039	0.0024±0.0031	34.6±6.6	0.0003±0.0016	1.0107	4.5314
9	65	21	0.64	0.20	0.0188±0.0023	0.0020±0.0037	56.5±4.4	0.0005±0.0013	1.0098	4.7196
10	57	16	0.56	0.15	0.0229±0.0029	0.0031±0.0032	75.1±4.0	0.0019±0.0020	1.0139	5.1487
11	47	13	0.46	0.12	0.0182±0.0034	-0.0024±0.0039	85.4±5.9	0.0003±0.0016	1.0145	5.1498
12	38	14	0.37	0.13	0.0154±0.0030	-0.0044±0.0032	-78.3±5.6	0.0005±0.0015	1.0062	4.6446
13	28	19	0.27	0.18	0.0168±0.0025	0.0076±0.0048	-47.5±4.5	-0.0002±0.0021	0.9879	4.0366
14	22	25	0.21	0.24	0.0188±0.0040	0.0073±0.0036	-32.2±3.9	0.0016±0.0014	1.0114	3.4382
15	18	32	0.17	0.31	0.0186±0.0031	0.0067±0.0040	-25.4±4.6	0.0000±0.0024	1.0130	3.1976
16	15	43	0.14	0.42	0.0156±0.0028	-0.0046±0.0038	-1.4±5.1	0.0019±0.0024	1.0199	2.6206
17	16	52	0.15	0.51	0.0162±0.0038	0.0053±0.0050	21.1±6.6	0.0001±0.0025	1.0160	2.7165
18	20	59	0.19	0.58	0.0165±0.0042	0.0034±0.0042	31.4±5.2	-0.0011±0.0024	1.0173	2.6743
19	25	65	0.24	0.64	0.0205±0.0040	0.0040±0.0047	44.8±4.4	-0.0006±0.0023	1.0128	2.4787
20	35	71	0.34	0.70	0.0189±0.0035	-0.0095±0.0037	67.9±5.4	-0.0019±0.0026	1.0213	1.8564
Average:					0.0179±0.0020	0.0000±0.0052	0.3±52.0	0.0001±0.0010		
Average Error:					0.0034	0.0041	5.2	0.0022		
Saved list C--(18)										
1	53	77	0.52	0.76	0.0023±0.0026	-0.0035±0.0039	-85.7±31.1	0.0009±0.0021	0.9926	4.4094
2	64	73	0.63	0.72	0.0008±0.0022	0.0028±0.0040	-84.5±94.6	0.0002±0.0031	1.0130	4.0791
3	72	66	0.71	0.65	0.0045±0.0026	0.0064±0.0031	-42.5±15.4	0.0010±0.0019	1.0154	3.0422

File Name: C:\EllipDat\04_2728_04R\NFM040318a5 Date: 5/13/2004
Description: Highly anisotropic IPyC layer? Time: 3:47:30 PM
Data Normalized

#	Pixel i	Pixel j	Position X	Position Y	Diattenuation (N)	Retardation (rad)	Fast Axis Angle (°)	Circular Diattn	Polar. Factor	Intensity (Arb. Units)
4	78	59	0.77	0.58	0.0021±0.0034	-0.0055±0.0032	55.4±54.0	0.0002±0.0019	1.0193	3.4460
5	81	48	0.80	0.47	0.0010±0.0031	0.0049±0.0039	-50.0±79.3	-0.0005±0.0015	1.0034	5.3539
6	80	39	0.79	0.38	0.0010±0.0025	-0.0041±0.0039	13.9±71.0	-0.0007±0.0021	0.9986	3.3764
7	76	27	0.75	0.26	0.0019±0.0032	-0.0028±0.0038	19.9±46.1	-0.0009±0.0022	1.0010	3.7620
8	69	18	0.68	0.17	0.0018±0.0031	0.0035±0.0038	70.3±49.6	-0.0010±0.0023	1.0233	4.1930
9	56	12	0.55	0.11	0.0016±0.0029	0.0018±0.0036	-72.0±55.2	-0.0018±0.0023	1.0048	3.6614
10	42	10	0.41	0.09	0.0007±0.0025	0.0073±0.0042	-65.3±101.5	-0.0043±0.0022	1.0170	2.7990
11	29	13	0.28	0.12	0.0020±0.0030	0.0059±0.0043	-23.4±43.3	0.0023±0.0025	1.0277	2.4557
12	20	21	0.19	0.20	0.0015±0.0032	-0.0034±0.0044	-38.3±40.0	0.0009±0.0020	0.9914	3.6120
13	14	32	0.13	0.31	0.0005±0.0034	-0.0021±0.0038	9.5±129.2	-0.0005±0.0019	1.0048	3.9156
14	11	45	0.10	0.44	0.0016±0.0027	-0.0015±0.0038	-22.5±49.3	-0.0002±0.0020	1.0052	4.0302
15	14	56	0.13	0.55	0.0011±0.0026	0.0041±0.0030	47.4±73.0	-0.0023±0.0017	0.9931	6.2879
16	20	65	0.19	0.64	0.0012±0.0027	0.0036±0.0035	83.2±60.5	-0.0011±0.0015	1.0037	5.3893
17	28	72	0.27	0.71	0.0013±0.0027	0.0035±0.0036	76.4±56.8	-0.0015±0.0018	1.0074	4.5869
18	39	77	0.38	0.76	0.0011±0.0025	-0.0050±0.0033	66.1±67.0	-0.0013±0.0015	0.9958	4.6310
	Average:				0.0015±0.0009	0.0009±0.0043	-2.3±58.8	-0.0006±0.0015		
	Average Error:				0.0028	0.0037	62.1	0.0020		

Saved list F--(18)

#	Pixel i	Pixel j	Position X	Position Y	Diattenuation (N)	Retardation (rad)	Fast Axis Angle (°)	Circular Diattn	Polar. Factor	Intensity (Arb. Units)
1	46	80	0.45	0.79	0.0123±0.0023	-0.0066±0.0033	-85.7±6.1	0.0001±0.0017	0.9864	5.0437
2	61	78	0.60	0.77	0.0138±0.0026	0.0075±0.0042	-69.9±5.8	-0.0001±0.0022	1.0046	2.7206
3	71	72	0.70	0.71	0.0114±0.0025	0.0067±0.0057	-47.7±10.7	0.0003±0.0022	1.0225	1.6417
4	78	65	0.77	0.64	0.0094±0.0033	0.0073±0.0053	-44.2±9.5	-0.0015±0.0031	1.0040	1.2548
5	82	53	0.81	0.52	0.0118±0.0033	-0.0029±0.0044	-15.7±7.0	-0.0027±0.0037	1.0209	0.8100
6	84	40	0.83	0.39	0.0146±0.0059	-0.0121±0.0084	11.0±12.0	-0.0041±0.0058	1.0175	0.2941
7	81	29	0.80	0.28	0.0153±0.0094	-0.0126±0.0083	23.7±18.1	-0.0023±0.0056	1.0206	0.2493
8	74	19	0.73	0.18	0.0099±0.0072	-0.0063±0.0082	27.9±22.1	0.0000±0.0065	1.0146	0.4533
9	64	11	0.63	0.10	0.0143±0.0082	0.0021±0.0104	64.3±17.7	0.0004±0.0052	1.0044	0.2692
10	47	7	0.46	0.06	0.0151±0.0072	-0.0112±0.0106	79.3±21.5	-0.0046±0.0086	0.9861	0.3201
11	34	8	0.33	0.07	0.0144±0.0053	-0.0100±0.0087	-80.0±10.0	-0.0057±0.0066	1.0066	0.3830
12	22	14	0.21	0.13	0.0067±0.0047	0.0090±0.0067	-30.5±25.9	-0.0018±0.0062	1.0147	0.5151
13	13	26	0.12	0.25	0.0092±0.0044	0.0028±0.0058	-28.3±13.8	0.0011±0.0030	1.0079	1.2085
14	9	38	0.08	0.37	0.0100±0.0033	-0.0056±0.0037	-2.2±9.6	-0.0003±0.0023	1.0033	3.1751
15	9	51	0.08	0.50	0.0105±0.0022	-0.0019±0.0032	11.9±7.0	0.0009±0.0017	0.9858	5.7252
16	15	63	0.14	0.62	0.0124±0.0026	0.0052±0.0033	37.2±5.8	0.0013±0.0012	1.0198	4.2494
17	23	73	0.22	0.72	0.0130±0.0051	0.0076±0.0047	45.1±8.5	0.0026±0.0027	1.0144	3.8608
18	34	79	0.33	0.78	0.0155±0.0026	-0.0087±0.0041	71.3±4.7	0.0015±0.0015	0.9804	5.3900
	Average:				0.0122±0.0025	-0.0016±0.0077	-1.8±51.6	-0.0008±0.0023		
	Average Error:				0.0046	0.0061	12.0	0.0039		

Saved list N--(23)

#	Pixel i	Pixel j	Position X	Position Y	Diattenuation (N)	Retardation (rad)	Fast Axis Angle (°)	Circular Diattn	Polar. Factor	Intensity (Arb. Units)
1	39	55	0.38	0.54	0.0022±0.0025	0.0031±0.0038	-64.6±31.8	0.0003±0.0020	0.9900	5.2002
2	42	57	0.41	0.56	0.0023±0.0022	-0.0035±0.0032	30.1±32.8	-0.0007±0.0024	0.9920	5.5564
3	49	58	0.48	0.57	0.0017±0.0025	-0.0014±0.0037	-19.7±42.4	-0.0004±0.0012	0.9870	5.3430
4	56	55	0.55	0.54	0.0032±0.0031	-0.0017±0.0037	10.1±23.0	0.0020±0.0019	1.0230	3.9605
5	56	52	0.55	0.51	0.0022±0.0031	-0.0031±0.0049	-7.5±29.8	0.0011±0.0020	1.0225	4.1324
6	54	47	0.53	0.46	0.0004±0.0034	0.0042±0.0026	-35.3±187.3	-0.0018±0.0015	1.0031	4.8234
7	53	41	0.52	0.40	0.0008±0.0025	-0.0041±0.0032	42.6±115.4	-0.0006±0.0019	0.9711	5.6243
8	56	36	0.55	0.35	0.0034±0.0025	-0.0013±0.0040	13.8±20.5	0.0004±0.0013	1.0187	3.6134
9	51	32	0.50	0.31	0.0013±0.0031	0.0014±0.0041	-41.5±53.7	-0.0007±0.0023	1.0186	3.9261
10	45	31	0.44	0.30	0.0012±0.0029	0.0031±0.0030	-36.3±71.8	0.0001±0.0019	1.0040	4.6602
11	40	32	0.39	0.31	0.0028±0.0022	0.0026±0.0033	-84.8±27.7	-0.0004±0.0017	1.0066	4.6178
12	36	37	0.35	0.36	0.0032±0.0029	-0.0011±0.0043	-23.8±27.1	-0.0004±0.0023	1.0168	3.6427
13	33	42	0.32	0.41	0.0017±0.0028	0.0013±0.0043	-74.6±43.8	-0.0006±0.0023	1.0195	4.1146
14	34	48	0.33	0.47	0.0014±0.0025	0.0024±0.0038	45.7±48.4	0.0003±0.0020	0.9812	4.8481
15	43	53	0.42	0.52	0.0004±0.0037	-0.0016±0.0036	-47.3±271.1	0.0012±0.0015	1.0050	5.6543
16	50	54	0.49	0.53	0.0004±0.0023	0.0032±0.0030	-36.8±183.2	-0.0014±0.0015	1.0073	7.1672
17	50	49	0.49	0.48	0.0012±0.0026	-0.0030±0.0030	79.5±55.2	0.0005±0.0015	0.9879	6.3509
18	48	43	0.47	0.42	0.0007±0.0021	0.0003±0.0027	-24.2±83.7	-0.0003±0.0021	0.9976	5.8068
19	48	37	0.47	0.36	0.0022±0.0027	-0.0024±0.0032	-70.0±34.0	-0.0006±0.0016	0.9937	5.4017
20	44	38	0.43	0.37	0.0025±0.0029	-0.0007±0.0029	-10.7±27.1	0.0006±0.0015	0.9936	5.7540
21	40	42	0.39	0.41	0.0026±0.0033	-0.0025±0.0032	-55.4±26.6	0.0003±0.0019	0.9925	6.0716
22	41	48	0.40	0.47	0.0037±0.0022	0.0014±0.0035	59.5±18.2	0.0005±0.0021	1.0056	5.1134
23	46	47	0.45	0.46	0.0021±0.0030	0.0008±0.0030	-27.4±36.9	0.0003±0.0015	0.9839	5.9906
	Average:				0.0019±0.0010	-0.0001±0.0025	-16.5±44.7	0.0000±0.0009		
	Average Error:				0.0027	0.0035	64.8	0.0018		

ADVANCED GAS REACTOR PROGRAM
OAK RIDGE NATIONAL LABORATORY

ORNL DOCUMENT CLEARANCE / REGISTRATION FORM

PERSON PREPARING FORM:	PHONE NO.:	DATE SUBMITTED:
Jan Z. Palmer	576-7054	August 9, 2004
DOCUMENT NO.:	**SPONSOR:**	
ORNL/CF-04/08	DOE-NE / Dr. Madeline Feltus	

TITLE:

Results from ORNL Characterization of HRB-21 Reference Fuel

AUTHOR(s):

John Hunn

SIGNATURES:

AUTHOR:

John Hunn — 8-9-04

Name: J. D. Hunn — Date

TECHNICAL REVIEWER:

O. M. Stansfield — 8-9-04

Name: O. M. Stansfield — Date

APPROVER:

G. L. Bell — August 11, 2004

Name: G. L. Bell — Date